博士論文

Model predictive control of building energy system using artificial intelligence

（人工知能を用いた空調熱源システムのモデル予測制御）

李　度胤

Model predictive control of building energy system using artificial intelligence

by Doyun Lee

A thesis submitted in partial fulfilment
of the requirements of the University of Tokyo
for the degree of Doctor of Philosophy

July 2021

Department of Architecture
Graduate School of Engineering
THE UNIVERSITY OF TOKYO

TABLE OF CONTENTS

LIST OF FIGURES

LIST OF TABLES

NOMENCLATURE

Variables

A_i: Surface area on the ith node of the tank (m^2)

c: Specific heat capacity (J/(kgK))

C: Electric consumption (kWh)

E: Electricity consumption (kWh)

H_C: Control horizon (-)

H_P: Prediction horizon (-)

J_s: Objective function

m_i: Mass of the ith node inside the tank (kg)

$\dot{m}_C$: Mass flow rate of the incoming water from the heat source side to tank (kg/s)

$\dot{m}_L$: Mass flow rate of the returning water from the load side to tank (kg/s)

$\dot{m}_i$: Mixed flow rate on the ith node inside the tank (kg/s)

N: Number of temperature stratification nodes inside the TES tank (-)

n: Number of dataset (-)

O_{baseline}: Baseline of occupancy schedule

$O_{t+H_P|t}$: Future occupancy schedule from timestep t to prediction horizon $t+H_P$ at t timestep

$O_{\text{variation}}$: Variation(disturbance) of occupancy schedule

P: Time-variant electricity price per a day (JPY/kWh)

Q_{BHE}: Cumulative extracted heat amount of the BHE (kWh)

q_{BHE}: Heat rate injected $(+)$ or extracted $(-)$ (W)

Q_{TES}: Remaining heat amount of TES tank (kWh)

Δq_{BHE}: Extracted heat rate difference between the consecutive time step (W)

R^2: Coefficient of determination (-)

RH: Relative humidity (%)

S: Solar radiation (W/m^2)

S_T: Source and sink term of internal energy (W/m^3)

t: Control timestep to update the control input for MPC execution

T: Temperature (°C)

T_a: Ambient temperature around the tank (°C)

NOMENCLATURE

T_{avg}: Average temperature of all nodes inside the tank (°C)

T_C: Inlet water temperature from the heat source side to tank in the charging operation mode (°C)

T_i: Temperature on the ith node inside the tank (°C)

T_L: Returning water temperature from the load side to tank in the discharging operation mode (°C)

$\bar{T}$: Mean temperature (°C)

$u(t)$: Control input

$u(t+P|t)$: Predicted control input from timestep *t* to prediction time horizon *t*+*P* at *t* timestep

$u^*_{t+H_P|t}$: Optimal control input from timestep *t* to prediction horizon $t+H_P$ at t timestep

u^*_t: Optimal control input from timestep *t* to *t+1* at *t* timestep

U: Overall heat loss coefficient between the tank and the surrounding environment per unit area (W/(m^{2}K))

$\dot{V}$: Volumetric flow rate of water (m^3/s)

y: Target value of the evaluation dataset (°C)

$\hat{y}$: Predicted value from the trained ANN (°C)

$\bar{y}$: Mean value of the evaluation dataset (°C)

$y(t)$: Control output

$\hat{y}(t+P|t)$: Predicted control output from timestep *t* to prediction time horizon *t*+*P* at *t* timestep

$y(t)$: Control output

$y(t)$: Control output

Greek letters

ε: Porosity of soil (-)

λ: Thermal conductivity (W/(m·K))

ρ: Density (kg/m3)

Superscripts

$t-1$: $t-1$ timestep

t: t timestep

$t+1$: $t+1$ timestep

NOMENCLATURE

Subscripts

b: Bulk property, borehole

$chiller$: Air-source heat pump chiller

c,in : Inlet of the air-source heat pump chiller

c,out : Outlet of the air-source heat pump chiller

$diff$: Diffuse solar radiation

dir: Direct solar radiation

err: Control error

exp: Experimental result

f: Fluid phase

$heater$: Electric immersion heater installed inside the water tank in experimental system

out: Outdoor environment

$occu$: Occupants

$pump$: Variable-speed pump

s: Solid phase

$setpoint$: Setpoint temperature

std: Standard

TES: Stratified chilled water thermal energy storage

TES,bot: Bottom layer inside the TES tank

TES,mid: Middle layer inside the TES tank

TES,top: Top layer inside the TES tank

$tank$: Water tank in experimental system

$zone$: Air-conditioned zone

$zone,MPC$: Model predictive controlled air-conditioned zone

Abbreviations

AMeDAS: Automated meteorological data acquisition system

ANN: Artificial neural network

ASHRAE: American society of heating, refrigerating and air-conditioning engineers

BCVTB: Building control virtual test bed

BHE: Borehole heat exchanger

BLAST: Building loads analysis and system thermodynamics

CVRMSE: Coefficient of variation of root mean square error

DE: Differential evolution

NOMENCLATURE

DOE: Department of energy
DP: Dynamic programming
FCU: Fan coil unit
GA: Genetic algorithm
GSHP: Ground-source heat pump
HEX: Fluid-to-fluid heat exchanger
HVAC: Heating, ventilation, and air conditioning system
ILS: Infinite line source
LM: Levenberg marquardt
MSE: Mean square error
MILP: Mixed integer linear programming
MPC: Model predictive control
PID: Proportional-integral-differential
RBC: Rule-based control
RC: Resistance-capacitance
RJ: Random jumping
RMSE: Root mean square error
SQP: Sequential quadratic programming
TES: Stratified chilled water thermal energy storage
εDE-RJ: Epsilon constrained differential evolution with random jumping

ABSTRACT

The present thesis aims to propose a model predictive control (MPC) strategy using artificial intelligence (AI) and to examine the practicality of its operational optimization of a building energy system with thermal energy storage (TES).

A total primary energy consumption in building sector accounts for 20–40% globally. Especially, the main factor of building's energy use is known to be caused by the heating, ventilation, and air-conditioning (HVAC) systems during their operational phase. For this reason, it is crucial to effectively manage the building energy systems to condition the building space is crucial. In this respect, MPC is known as a promising way as an optimal control strategy for efficient building operations.

The MPC is an optimal control method for HVAC systems because it determines the optimal control input based on the predicted future behavior of the HVAC system. However, the performance of the MPC controller is hugely influenced by the accuracy of the model that represents the system behavior and the efficiency of the optimization solver that searches for the optimum solution of the control input.

In general, the HVAC system has a non-linear behavior composed of numerous and various equipment, therefore, constructing its predictive model is complicated. Also, when applying the MPC strategy, the optimization problem must be solved in a real-time manner and thus a low computational load is required. On the other hand, in recent years, with the improvement of the technical level of AI, it is expected that high-precision and high-speed prediction models and optimization algorithms can be expected. The practicality and applicability of the MPC strategy for the building facilities can be further enhanced when it is designed by using the AI.

Therefore, in this study, an AI-based MPC framework was developed and verified for a building energy system equipped with TES based on the simulation and experimental analysis. The future behavior of the TES system was modeled using an artificial neural network (ANN), focusing on the fact that the high prediction accuracy and low computational cost can be expected from ANN. Also, a metaheuristic method was adopted as an optimization solver since it is known to have a faster convergence speed than the conventional mathematical programming in solving a nonlinear optimization problem with handling a multiple constraint.

First, in Chapter 3, the practicality of the ANN prediction models in building energy systems was investigated. The ANN prediction models of the stratified chilled water TES system and the borehole heat exchangers (BHE) for a ground source heat pump (GSHP) system were constructed based on a case study to determine the valid input parameters for the training dataset. The simulation results from a high-fidelity physical model were utilized as the training dataset for the TES system. In regard with the BHE system, the ANN model was constructed using the results from a numerical simulation. It was observed that a highly accurate ANN models that results in marked reductions in the computational cost can be constructed by combining the most valid input parameters.

Also, the AI-based MPC strategy was proposed in Chapter 4 and its feasibility was analyzed with the choice of a virtual office building and target systems including TES. The ANN was utilized to predict the future behavior of the systems and the epsilon constrained differential evolution with random jumping (εDE-RJ) was implemented as an optimization problem solver to minimize operating costs. In addition, a significant occupancy disturbance was intentionally considered to test the ability of the MPC strategy to manage future disturbances. The simulation results of the AI-based MPC were compared with those of the conventional rule-based control (RBC). As a result, the MPC reduced the total operating costs 3.4% compared to the RBC during the four-day simulation period.

However, it is still necessary to verify the AI-based MPC strategy by experimental analysis considering the following points. First, the historical data obtained from the simulation building model is quantitatively and qualitatively better than actual operational data since normally the real operation data incudes a huge noise and uncertainty in the measurement. Furthermore, in the simulation-based analysis, the system physics occurred in the actual system such as mechanical characteristics of equipment when the operation starts and stops the driving, the heat loss that occurs when the heat is transferred from the primary side to the secondary side, and the time delay or the fluctuation of the zone temperature regulation that occurs when the heat is supplied from the primary side to the secondary side cannot be carefully considered. Finally, the MPC controller should be tested both in a software manner and a hardware manner, by linking the main MPC calculator and the system.

Therefore, the downscaled mock-up system was devised to validate the developed AI-based MPC strategy via experimental analysis in Chapter 5. The experimental system for the cooling operation includes an air-source heat pump chiller, TES, heat exchangers, and variable-speed pumps. The air-conditioning space was simulated by the water tank, and the cooling load was assigned by an electric immersion heater.

In Chapter 6, the developed AI-based MPC strategy was implemented to the experimental system under three representative cooling load profiles where the thermal load continues in a high, medium, and low level during the day and compared with the RBC strategies that prioritize the TES operation with proportional integral differential (PID) controller. In conclusion, the proposed AI-based MPC strategy reduced the total operating cost by 9.06–14.56% compared to the RBC strategy. In addition, it was observed that the MPC strategy could flexibly determine the operation schemes depending on the level of the daily cooling load.

In Chapter 7, the effectiveness of the AI-based MPC was further verified by comparing it with two different RBC strategies. Two RBC cases were collected from the experimental system that differed in the priority of the TES discharging operation during the cooling hours. Firstly, the RBC-1 case commenced the TES discharging operation as soon as the cooling operation hours was started. On the other hand, the RBC-2 case operated the chiller to manage the thermal and the TES was discharged where he electricity price was highest during the occupied hours. Based on the comparative analysis between the MPC strategy and those two RBC strategies, the potential of cost savings of AI-based MPC strategy was further verified to save the operating costs by 9.7–22.5%.

Chapter 1. Introduction

Chapter 1. Introduction

1.1. Background and motivation

Globally, the building sector accounts for approximately 20–40% of total primary energy consumption [1,2]. Especially in existing buildings, heating, ventilation, and air-conditioning (HVAC) systems account for a major part of their total energy consumption during the operational phase [3]. For this reason, effective management of building energy systems that condition the building space is crucial for reducing energy use and greenhouse gas emissions.

In order to manage the energy use in the building sector, to introduce the active energy storage system such as thermal energy storage (TES) is known to be desirable. The TES can store thermal energy to be used at a later time for heating or cooling applications therefore the thermal peak load can be shifted, or the thermal load can be leveled. In a numerous previous article, it was found that the TES can provide operating cost savings by allowing the system to shift time of energy production to off-peak hours and also can improve energy efficiency by storing the excessive and waste heat and delivering to another or later time.

The Fig. 1-1 below shows the duck curve problem observed in Kyushu area, Japan. The duck curve problem can be an alarming concern since the generation resources like solar power significantly reduce the load during the daytime but not during the nighttime and thus a surge in demand may occur as the sun sets. Given this fact, the energy storage system is expected to play an important role by storing energy in low demand hours for use in high demand hours.

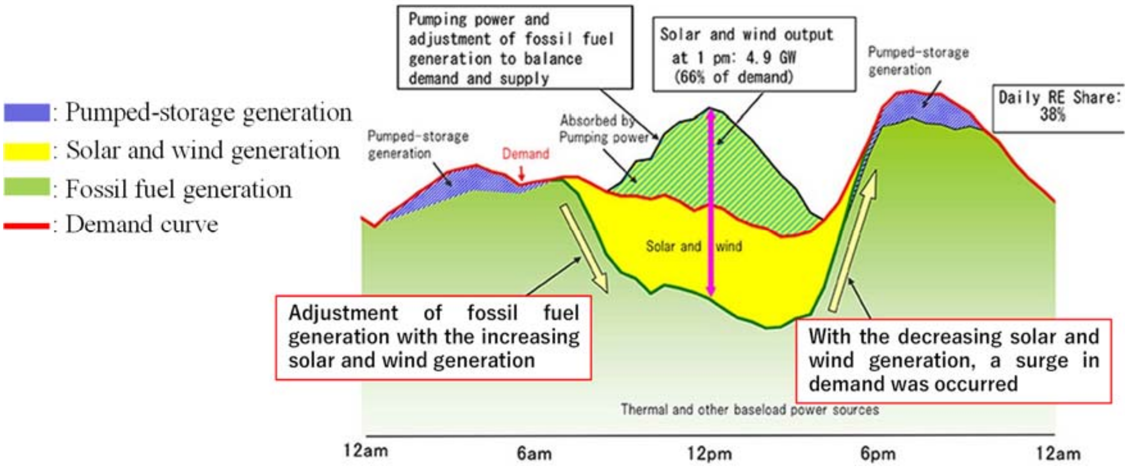

Fig. 1-1. The duck curve problem observed in Kyushu area, Japan (Kyushu Electric Power Co., Inc.).

To date, the energy storage system has been controlled by the three main conventional control strategies as follows: Storage-priority control, Chiller-priority control, and Constant-proportion control [4]. Those conventional control strategies can be included as the rule-based control (RBC) to manage the system based on the pre-defined simple if/then/else rules. According to the opinions from the people working in practice, the current situation is that the heat storage tank system is still controlled based on the constraint of a predetermined operating temperature in numerous existing buildings. However, it is necessary to develop intelligent ways to use TES rather than on/off schedule, for instance, optimizing the rate and time of TES discharge based on operational disturbances such as load, outdoor, price conditions.

In this respect, model predictive control (MPC) has received significant attention as an optimal control strategy for efficient building operations [5]. MPC is a promising optimal control method for HVAC systems because it determines the optimal control input based on the predicted future behavior of the HVAC system [6]. Because of the predictive nature of MPC, in contrast with conventional control strategies such as on/off or proportional-integral-differential (PID) control, MPC is especially useful for controlling on-site energy storage systems such as TES systems [7].

However, there are two main concerns in designing and implementing an appropriate MPC strategy as shown in. The core of the MPC controller consists of two main technologies: a prediction model to predict the dynamic behavior of the control subject and an optimization solver to find the optimal control input [8].

In recent years, many researchers have dedicated their efforts to designing MPC strategies for the building sector to solve the low efficiency of building energy systems [9]. MPC is a promising control scheme for building management to guarantee zone temperature regulation, efficient energy use, and competitive operating cost by flexibly manipulating the control variables under fluctuating operating conditions such as weather conditions, occupancy levels, and electricity prices [10].

However, practical use of the MPC strategy in building operations is still lacking. One major reason for its slow uptake in the building field is the initial difficulty with obtaining a practical MPC framework that has a fast and accurate prediction model and a reliable optimization solver without exorbitant computational costs. In this regard, the practicalities of the MPC can be addressed using a machine learning prediction model and optimization solver.

1.2. Literature review

In the last few years, MPC has been received significant attention as an optimal control strategy for building energy systems [10,11]. In fact, in the building sector, HVAC systems take a large portion of the total primary energy consumption in the building sector [12,13]. Considering that most of the existing buildings in the world are not newly built buildings, it is considered that the most effective way to manage the energy consumption in the building sector is to introduce an optimal control strategy for the HVAC systems [14].

In the MPC strategy, the MPC controller calculates the control law by minimizing or maximizing the objective function handling constraints to find the optimal solution to the control problem set by the operator for the purpose of the building's operation. The objectives of the operation in the building sector can be briefly categorized as follows: to increase the thermal comfort of occupants, to reduce operation costs, to reduce the energy consumption, to effectively control the heat source equipment, or the combination of these.

For example, Cigler adopted the MPC strategy to optimize the predicted mean vote (PMV) index and found that the energy can be saved further 10–15% while optimizing the PMV index [15]. Ferreira et al. also utilized the MPC strategy to satisfy the PMV index and save energy and found that energy can be saved greater than 50% while satisfying the PMV index for occupants' thermal comfort [16].

Also, Siroky et al. investigated that the MPC strategy had energy savings potential between 15% and 28% for building heating systems depending on the insulation level of the building envelop and the condition of the outside [17]. Rehrl et al. designed the MPC controller and found that it was well performed in the temperature control via water-to-air heat exchangers in HVAC systems [18].

Especially, the MPC algorithm is known that it has a huge potential to be applied to active energy storage systems such as thermal energy storage (TES) or renewable energy heat sources because of its capability to consider the objective function with constraints in the optimization problem, and the prediction of the future behavior of the plant system considering the unexpected disturbances [7]. Based on this potential of the MPC application, many previous studies have been focused on its application to building energy systems, especially on active energy storage systems.

For example, Ma et al. employed MPC strategy in the university building equipped with an active chilled water storage tank charged by a series of chillers and found that MPC could reduce the electricity bill up to 24.5% [19]. They also stated the formulation of MPC strategy in detail and shared the current issues of how to apply the MPC strategy for HVAC systems elaborately for its effective application to the thermal energy storage system in the previous publication of [20]. Also, Fiorentini et al. investigated a hybrid MPC strategy to control solar-assisted HVAC systems with on-site thermal energy generation and storage, and they found the hybrid MPC strategy could well perform to achieve the optimal operation schedule [21].

1.3. Current issue

The concept of MPC is not new; it was proposed 40 years ago to support the processing industry [22] and has also been developed for the building sector to have high potential as a well-advanced control scheme for building energy systems that outperform conventional control schemes. However, there are relatively few cases where the MPC strategy is actually applied to building energy systems considering that various studies as reviewed in the earlier section proposed and devised the MPC strategy verified as effective in building management. The considerable reason is that each building energy system has its own unique characteristics, so it requires considerable effort to create a predictive model and that an optimization method to solve large-scale optimization that is fast and efficient enough to be applied to real-time control must be prepared.

As stated above, there are two key elements in the MPC framework, i.e., prediction models and optimization solver that are needed to be designed carefully to maximize the performance of the MPC strategy. Prediction models can be classified into three main categories: white-box models, grey-box models, and black-box models [23]. In general, energy behavior modeling of the building system using thermal resistance capacity model and the energy simulation tools such as TRNSYS, EnergyPlus, ESP-r, and DOE-2 corresponds to the construction of a predictive model using a white-box model.

For example, Ma et al. [24] utilized a simulation tool of EnergyPlus to model a multi-zone equipped with a variable air volume cooling system. Candanedo et al. [25] also utilized the EnergyPlus to predict the behavior of radiant floor heating and solar-source heat pump. Henze et al. [26] constructed a TRNSYS building model to capture the thermal behavior of commercial buildings equipped with active and passive building thermal storage. However, it is time-consuming to validate them while the computational load is relatively high when they were linked with an optimization process for MPC schemes, although it can assure the prediction performance [14].

Black-box models have lower complexity and require fewer inputs than white-box models, which rely on the specific physics of the system. Black-box models can be constructed without an in-depth understanding of complex system physics. Another benefit of the black-box models is that they can overcome the inconsistencies in complex building energy systems with high speed, and thus, they are especially well-suited for use in MPC controllers [7].

Candanedo et al. used an MPC design for a building cooling operation with an ice storage device, and the system’s prediction models were identified with a simplified linear thermal model [27]. Touretzky et al. optimally managed the TES systems using an economic MPC strategy, where they configured the complex system, which included a chiller-based TES system, with an equation-oriented model based on the known physical parameters [28].

Also, in order to construct a grey-box model, both time-consuming processes for constructing a physical model and parameter identification for a data-driven model are required. Black-box models can suffer from imprecise prediction when the training data do not cover a wide range, however, it is known that they are well-suited for use in MPC controllers with high speed if they can be appropriately constructed with qualified training data [7].

Since simplified system models generally suffer from inaccuracies due to the simplifications, an advanced approach for MPC design is needed. Among the numerous black-box models available, artificial neural networks (ANNs) have been most commonly used for building predictions and HVAC control [29]. Using a surrogate ANN prediction model can overcome the drawback of the high computational load of white-box models while ensuring accurate predictions in MPC applications. Afram et al. designed an ANN-based MPC system and conducted a case study for managing residential HVAC systems with ground source heat pump systems. They found that the prediction performance of the proposed ANNs was significantly higher when utilized in practical MPC applications [30].

Optimization solvers can be segmented into two main categories: mathematical programming and metaheuristic algorithms [31]. Wakui et al. employed mixed-integer linear programming (MILP) as an optimization solver in the operation management of residential energy grids using an MPC strategy [32]. The MILP-based MPC controller was successful in limiting unnecessary shutdown and start-up of the cogeneration units. Kelman et al. utilized sequential quadratic programming (SQP) to solve the bilinear optimization problem in MPC implementation [33]. However, in general, the convergence speed of these mathematical-programming-based optimization problem solvers is slow because they are more appropriate for finding a solution to linear or convex problems rather than to nonlinear or nonconvex problems. Finding the optimal solution with high convergence speed and efficient constraint handling is needed for a reliable MPC controller.

Ikeda et al. proposed a type of metaheuristics optimization method, called epsilon constrained differential evolution with random jumping (εDE-RJ). The εDE-RJ method worked as a highly efficient problem solver to find the optimal solution for multiple heating systems, including ground source heat pumps [34]. Furthermore, the authors validated the proposed εDE-RJ method by comparing it with conventional optimization algorithms such as dynamic programming (DP) and genetic algorithm (GA) methods. Both the original and advanced εDE-RJ methods performed well in finding an optimal operation strategy in district cooling systems by significantly reducing the operating costs and computational load compared to conventional optimization solvers [35]. With the development of these artificial intelligence and metaheuristics tools, MPC is expected to be implemented at scale to increase the efficient management of building energy systems.

1.4. Overall objectives of present thesis

The present thesis aims to propose a model predictive control (MPC) strategy for building energy systems using artificial intelligence (AI). With the choice of target energy systems that include a TES system, the MPC controller was proposed using AI techniques in order to secure the practicality and applicability for constructing a prediction model and optimization solver. Also, a developed AI-based MPC strategy was investigated and analyzed based on both simulation and experimental results. The overall research flow of the present study is shown in Fig. 1-2.

In Chapter 1, the background, motivation, and purpose of this study are introduced. In this thesis, in order to develop an effective MPC strategy, the artificial neural network (ANN) was utilized as a prediction model, and metaheuristics were applied for an optimization solver. In Chapter 2, a basic theory about fundamentals of MPC algorithm, ANN, and metaheuristics optimization method utilized in this study are described. First of all, the feasibility analysis of ANNs for building energy systems was conducted in Chapter 3. In this chapter, the entire modeling process of the prediction models for stratified chilled water thermal energy storage (TES) and borehole heat exchanger (BHE) for ground source heat pump (GSHP) system using ANN is presented.

Based on the results from Chapter 3, it was found that ANN showed high prediction accuracy and low computational cost in predicting the behavior of the building energy systems. Therefore, the feasibility analysis of AI-based MPC strategy with the choice of a virtual office building and target energy systems including TES was conducted based on the simulation in Chapter 4. The simulation results obtained from Chapter 4 showed that the AI-based MPC strategy can obtain an optimal operation schedule of the building energy system including TES while reducing the total operating costs compared to the conventional rule-based control (RBC) strategy that prioritizes the TES operation.

Therefore, in order to experimentally validate the proposed AI-based MPC strategy, the experimental setup was constructed and explained in Chapter 5. In Chapter 6, the developed AI-based MPC strategy was tested under three different patterns of cooling load schedules where the load continues as high, medium, and low during the day. Also, in order to verify the cost-effectiveness of the AI-based MPC strategy, the RBC case of TES priority operation with PID controllers was collected from the experimental system.

In Chapter 7, the developed AI-based MPC strategy was tested and its results were compared with two RBC strategies that differed in the cooling operation with TES discharging priority. One of the RBC strategies commences the TES discharging operation as soon as the cooling mode commences and the other case begins the chiller cooling operation by itself, and the TES begins discharging when the electricity price is highest during the occupied hours. Finally, in Chapter 8, the conclusion of the present thesis was summarized, and the limitations of the research are addressed.

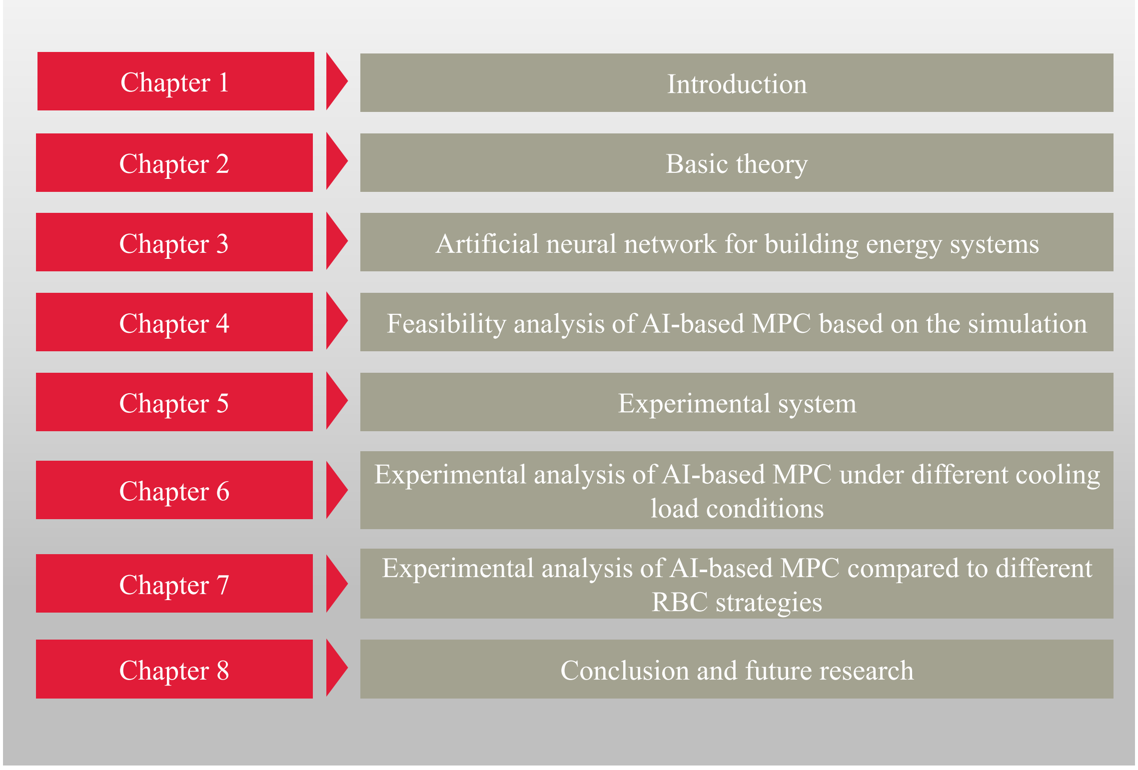

Fig. 1-2. Overall structure of thesis to propose and investigate AI-based model predictive control (MPC) for building energy system with thermal energy storage (TES).

Chapter 2. Basic theory

Chapter 2. Basic theory

2.1. Model predictive control (MPC)

Model predictive control (MPC) is a control algorithm that predicts the output of the system obtaining an optimized solution and assigns it as control input [36,37]. While a feedback control determines control input from previous information as shown in Fig. 2-1 (a). The MPC predicts the future behaviors of the control subject with the prediction model and determines a control input so that the object is optimized in a certain horizon as described in Fig. 2-1 (b).

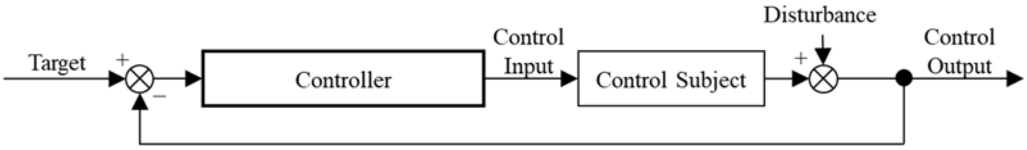

(a) Feedback control

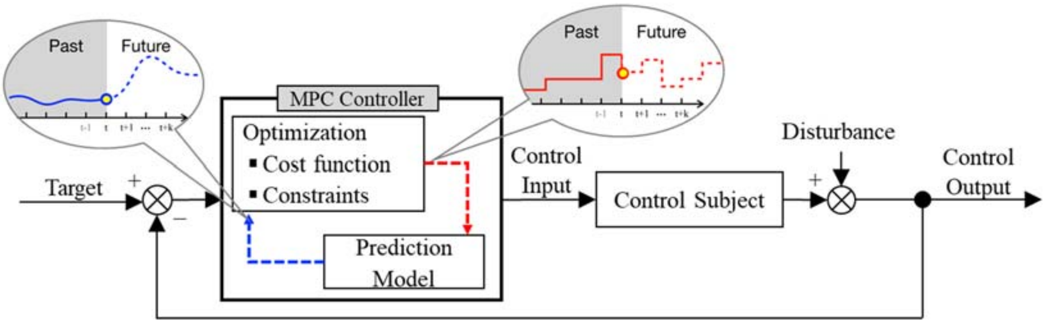

(b) Model predictive control

Fig. 2-1. Comparison of block diagram between feedback control and model predictive control (MPC).

In general, the control problem in the MPC strategy can be defined using a state-space model as Equations. (2-1) and (2-2) below. In Equations. (2-1) and (2-2), t is the discrete-time index, $u(t)$ is the control input, $x(t)$ is the state of the control subject, and $y(t)$ is the control output.

$$x(t+1) = Ax(t) + Bu(t) \tag{2-1}$$

$$y(t+1) = Cx(t+1) \tag{2-2}$$

For example, in building energy systems, $x(t)$ is considered as the status of the system such as inlet and outlet temperature of the heat source equipment or the temperature of the air-conditioning zone, $u(t)$ is the design variables to be chosen by the optimization solver such as the flow rate of supplying pump or the setpoint temperature of the heat source equipment, and $y(t)$ is the control output when the system was managed as of $u(t)$ such as the temperature of the air-conditioning zone, the electricity consumption of the heat source equipment, or the operating costs of the system.

Using the Equations. (2-1) and (2-2) that simply defined by the state-space model, the expected control output up to a certain future time horizon of H_P can be expected as shown in Equation. (2-3).

$$\hat{y}(t+H_P|t) = C\hat{x}(t+H_P|t) = C\left[A^{H_P}x(t) + \sum_{i=1}^{H_P} A^{i-1}Bu(t+H_C|t)\right] \tag{2-3}$$

Where the $\hat{y}(t+H_P|t)$ is the predicted control output from the current time step t to the prediction horizon $t+H_P$ at t timestep based on the predictive model, $\hat{x}(t+H_P|t)$ is the expected state of the system from the current time step t to the prediction horizon $t+H_P$ with the available information at t timestep, and $u(t+H_P-i|t)$ is the design variables (free variables) from the current time step t to the certain future horizon (i.e., control horizon) of $t+H_C$ to be chosen by optimizer at t timestep.

In MPC controller, the optimization solver searches for the design variables of $u(t)$ in order to obtain an optimal future output of $y(t)$ on the considered time horizon, and at the same, time the efforts to reduce the difference the present control input and that of next timestep can be made to manage the system more stably without assigning a fluctuating control input. Therefore, the objective function (J) to reach the target setpoint without changing the control amount suddenly in the MPC problem can be generalized as Equation. (2-4).

$$J = \sum_{j=1}^{H_P} \alpha(j)[\hat{y}(t+j|t) - y^*(t+j)]^2 + \sum_{j=1}^{H_C} \beta(j)[\Delta u(t+j-1)]^2 \tag{2-4}$$

Here, α is the penalty constant of the error between the predicted control output of $\hat{y}$ and the target control output of y^*, β is the penalty constant of the rate of change in control input ($\Delta u(t) = |u(t+1) - u(t)|$), H_P is the prediction horizon, and H_C is the control horizon.

In Equation. (2-4), when the discrete control time horizon is less than the prediction horizon ($H_C < H_P$), the difference of change in control input is zero ($\Delta u(t+H_C) = \Delta u(t+H_C+1) = \cdots \Delta u(t+H_P) = 0$), therefore, the control input in all timesteps beyond the control horizon have the same value as the control input applied at $t+H_C$ timestep of $u(t+H_C)$.

The schematic of the algorithm for the MPC was described in Fig. 2-2. The purpose of the MPC is to derive the optimal control input under the target command and use the moving horizon method (i.e., receding horizon method) in each timestep. To summarize, in MPC strategy, the control variables of $u^*(t+H_P|t)$ can be chosen based on the iterative searching from the optimization solver, based on the following steps (also see Fig. 2-2):

(Step 1) Define the current timestep as $t-1$ and acquire the measured value from the system (y_{t-1}).

(Step 2) Prediction model predicts the output of the system ($\hat{y}_{\mathrm{t+H_P}}$) in the future horizon of $[\mathrm{t}, \mathrm{t}+\mathrm{H_P}]$ based on the measured value ($y_{t\text{-}1}$).and control variables chosen by optimizer ($\hat{u}_{t+H_P|t}$).

(Step 3) Iterative calculation to find the optimal control input ($u^*_{t+H_C|t}$) in the future horizon of $[t, t+H_C]$ to minimize the objective function.

(Step 4) Of the optimal control inputs obtained in (Step 3), only the first set of u^*_t is assigned to the system from the next time t to $t+1$, and return to (Step 1).

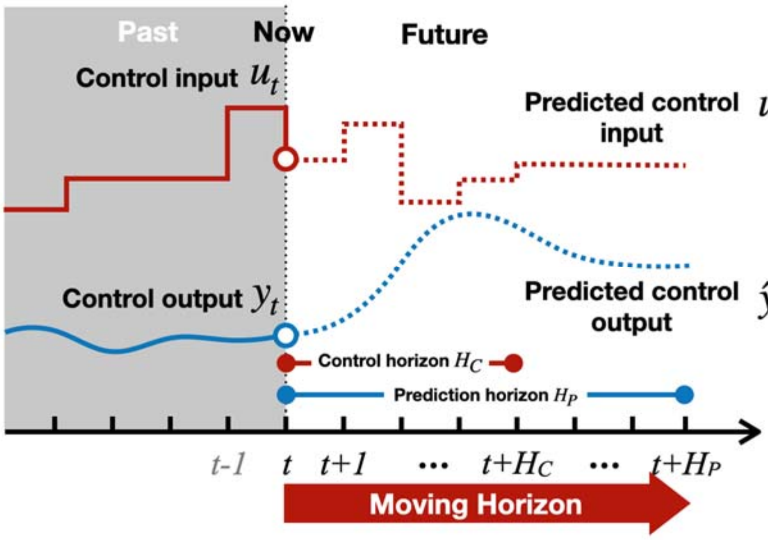

Fig. 2-2. Schematic of the moving horizon algorithm for model predictive control (MPC).

2.2. Artificial neural network (ANN)

The control problem of a building energy system composed of complex and various equipment corresponds to a nonlinear control problem [38]. Therefore, it is generally time-consuming to model accurate building and system physics. For this reason, in recent years, as the interest in technology improvement of artificial intelligence (AI) and big data processing has increased, artificial neural network (ANN) is widely used to predict and control the nonlinear characteristics of complex building energy systems [39]. The behavior of the ANN is simple to be understood, and the calculations performed at each node in the neural network can be mathematically explained [40]. There are various neural network models according to the structure of the neural network [41]. Although various neural network models such as recurrent neural network (RNN), convolutional neural network (CNN) are being utilized in recent years, the feedforward neural network model is still the most used [29].

2.2.1. Multi-layer feedforward network

A multi-layer perceptron is a neural network in which one or more hidden layers exist between an input layer and an output layer and connected in the direction of an input layer, a hidden layer, and an output layer. It is a feedforward type of network that the internal connection of each layer and the direct connection from the output layer to the input layer do not exist. The previous research [42] explains that the 3-layer feedforward type of neural network can emulate any function if the number of hidden neurons is set to a sufficient number. In general, the structure of a multi-layer perceptron can be described as shown in Fig. 2-3.

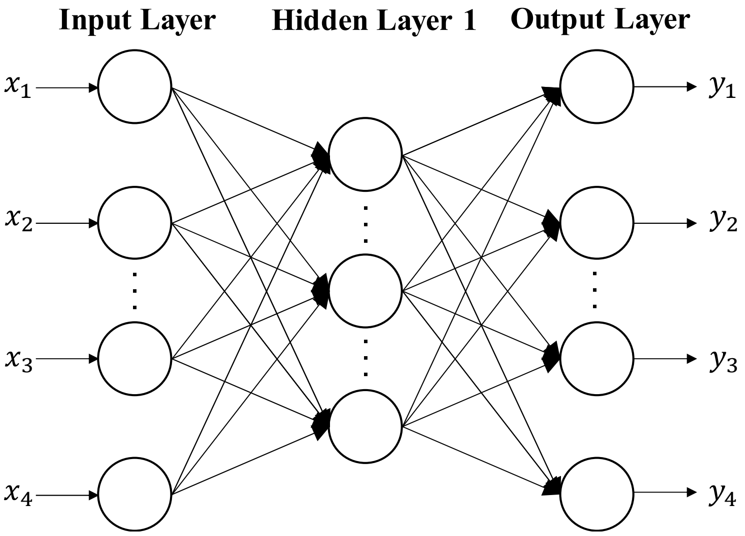

Fig. 2-3. The structure of multi-layer (3-layer) perceptron.

Among the numerous neurons that multi-layer perceptron has, one neuron of them can be expressed as shown in Fig. 2-4. Each neuron in the input node is connected to a neuron in the hidden layer by weight (w), and the neural network trains while updating this weight (w). This relation can be expressed by Equation. (2-5), where the f is an activation function.

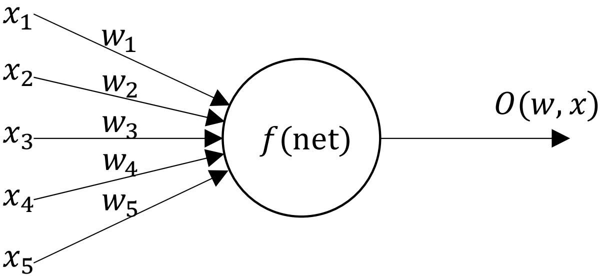

Fig. 2-4. Neuron modeling for artificial neural network (ANN).

$$\begin{aligned} \mathrm{o}(w,x) &= f\left(\sum_{i=0}^{n} w_i x_i\right) \\ &= f(\boldsymbol{w}^T \boldsymbol{x}) \\ &= f(net) \end{aligned} \tag{2-5}$$

When the sum of the product of the weight (w) and the input value (x) is positive, the function f is active. When the sum of the product of the weight (w) and the input value (x) is negative, then function f is inactive. There are several kinds of activation functions. Equation. (2-6) is used as a linear activation function when the range of mapping is not limited to a specific area. Equation. (2-7) is a hard limiting function (or can say as a step function), and if the value of net is larger than 0, it is mapped as 1. If the value of net is smaller than 0 then it is mapped as -1.

$$f(net) = \begin{cases} \mathrm{c} \cdot net, & net \geq 0 \\ c \cdot net, & net \leq 0 \end{cases} \quad (c = constant) \tag{2-6}$$

$$f(net) = \begin{cases} +1, & net \geq 0 \\ -1, & net \leq 0 \end{cases} \tag{2-7}$$

Equation. (2-8) describes a bipolar sigmoid function with a mapping range of −1 to +1. Equation. (2-9) is a unipolar sigmoid function with a mapping range of 0 to +1.

$$f(net) = \frac{2}{1 + e^{-\lambda net}} - 1 \tag{2-8}$$

$$f(net) = \frac{1}{1 + e^{-\lambda net}} \tag{2-9}$$

The derivatives of the above two functions in Equation. (2-8) and Equation. (2-9) can be easily represented in terms of their own values. The derivatives of the above two functions can be expressed as Equation. (2-10) and Equation. (2-11), respectively. Because of the simple result of their derivatives, the Equation. (2-10) and Equation. (2-11) are frequently used as active functions for artificial neural networks.

$$f'(net) = \frac{\lambda(1 - o^2)}{2} \tag{2-10}$$

$$f'(net) = \lambda o(1 - o) \tag{2-11}$$

2.2.2. Evaluation index

The training of the ANN can be verified with statistical index by evaluating how well the predicted data from the ANN prediction model are matched to the target data. As the error between the predicted data from the trained ANN and the target data is close to zero and the relationship between the input parameter and the target parameter is established, the ANN can be judged as well trained.

2.2.2.1 Coefficient of determination (R^2)

The coefficient of determination (R^2) can be obtained from the linear regression of the predicted and target data and indicate the variability of the data [43]. The range of the R^2 index is between 0 and 1, and the closer the value is to 1, the higher the correlation between the predicted data and the target data can be. However, since the result of error between predicted and target data is not considered with R^2, the prediction accuracy of the ANN may be low even if the R^2 value was shown close to 1. It is not appropriate to evaluate the accuracy of the ANN prediction model only with the R^2 index since the R^2 value is naturally increased if the number of independent variables increases. Therefore, it is recommended to be utilized together with other evaluation indices such as mean square error (MSE) which considers the error. The R^2 can be calculated based on the Equation. (2-12).

$$\mathrm{R}^2 = \frac{\frac{1}{N}\sum_{i=1}^{N} e_i^2}{\frac{1}{N}\sum_{i=1}^{N}(y_i - \bar{y})^2}\, or\, \frac{\sum_{i=1}^{N}\left(\hat{y}_i - \bar{\hat{y}}_i\right)^2}{\sum_{i=1}^{N}(y_i - \bar{y})^2} \tag{2-12}$$

Where the R^2 is the coefficient of determination, the e_i is the error between predicted data and target data, the y_i is the target data, the $\bar{y}$ is the average of target data, the $\hat{y}_i$ is the predicted data, the $\bar{\hat{y}}_i$ is the average of the predicted data, and N is the number of data.

2.2.2.2 Mean square error (MSE)

The mean squared error (MSE) is averaged over the square of the error. The MSE is often used as a qualitative measure of the accuracy of the statistical estimation because it is simple to calculate and perform statistical analysis. When the MSE value is closer to 0, this refers to the higher prediction performance. The MSE can be calculated according to the Equation. (2-13).

$$\mathrm{MSE} = \frac{1}{N}\sum_{i=1}^{N}(\hat{y}_i - y_i)^2 \tag{2-13}$$

Here, the MSE is the mean square error, the $\hat{y}_i$ is the predicted data, the y_i is the target data, and N is the number of data.

2.2.2.1 Root mean square error (RMSE)

The root mean squared error (RMSE) is a statistical index that can be calculated by the square root of the average of the error between the predicted data and target data, i.e., the square root of the MSE. The RMSE is a measure of how close the predicted data is to the target data. Statistically, the RMSE can assess how much the predicted data and the actual observed data have fallen on average. The RMSE can be calculated based on the Equation. (2-14).

$$\mathrm{RMSE} = \sqrt{\frac{1}{N}\sum_{i=1}^{N}(\hat{y}_i - y_i)^2} \tag{2-14}$$

2.2.2.1 Coefficient of variation of the root mean square error (CVRMSE)

The coefficient of variation of the root mean square error (CVRMSE), which can be derived from the RMSE, captures the variability in the error between the predicted and target values and is directly indicative of the uncertainty in the model used. When the CVRMSE is closer to 0%, the more accurate the prediction is. The CVRMSE can be derived from Equation. (2-15).

$$\mathrm{CVRMSE} = \frac{1}{\bar{y}}\sqrt{\frac{1}{n}\sum_{i=1}^{n}(y_i - \hat{y}_i)^2} \times 100 = \frac{\mathrm{RMSE}}{\bar{y}} \times 100 \tag{2-15}$$

2.3. Metaheuristics

2.3.1. Introduction

There are several criteria for classifying optimization techniques depending on the viewpoints, such as the number of objective functions and the presence or absence of constraints. Basically, optimization methods are classified depending on the nature of the set (domain) of the variables to be selected by the optimization solver [44]. Therefore, optimization methods can be classified into a continuous optimization that searches for continuous variables and a discrete optimization that searches for discrete variables as shown in Fig. 2-5. Discrete optimization is also called combinatorial optimization. Furthermore, the discrete optimization problems are classified into exact methods, which can find global optimum solutions, and approximate methods, which can find reasonably good solutions that are close to optimal.

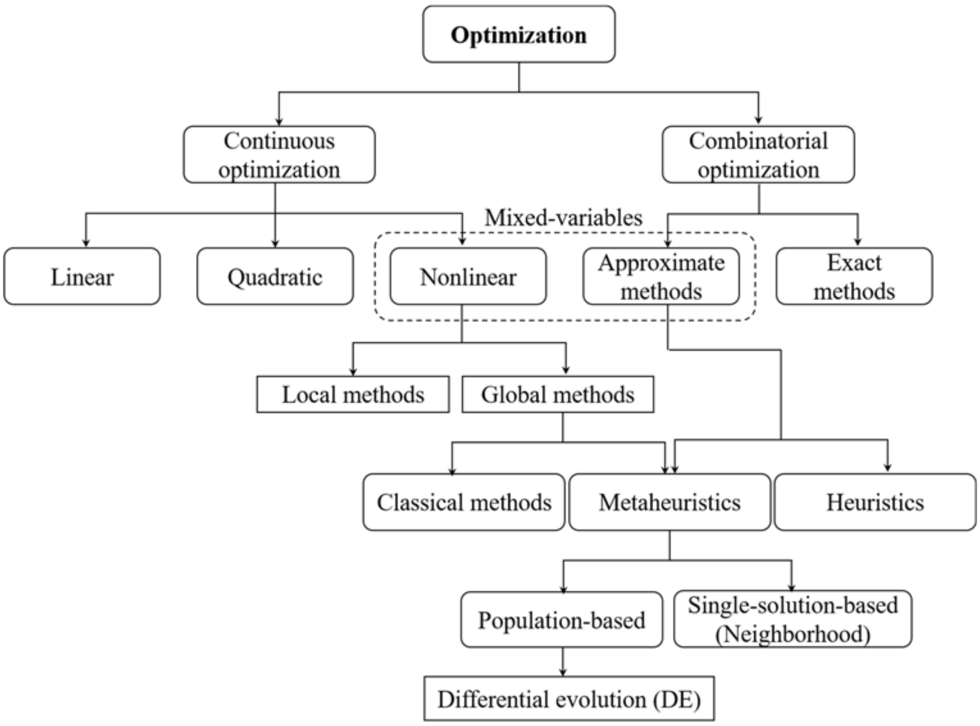

Fig. 2-5. Classification of optimization methods depending on the nature of the set (domain) of the design variables to be selected by the optimization solver [44].

The exact solution method includes a typical branch-and-bound method or a dynamic programming method. These methods can find a solution (i.e., exact solution) where the optimality is guaranteed even in an optimization problem having a large number of local optimum solutions. However, there is a disadvantage that it is difficult to converge in a problem that shows high non-linearity with numerous variables and cannot be differentiated. Under the condition of infinite iteration (i.e., when the time required for optimization calculation is infinite), it is desirable to pursue higher optimality, however, such convergence is meaningless in the application of real-life problems. It is practically impossible to solve a large-scale optimization problem in which the amount of calculation increases exponentially according to the size of the problem based on an exact solution method.

As stated above, it is almost impossible to find the global optimal solution in a reasonable time using the exact solution method. In this case, an approximate solution method that finds a reasonably good solution that is close to the optimum by proceeding a searching for solutions within the permissible time is a useful alternative [45]. Metaheuristics are a type of approximate solution that is likely to find a good solution in an efficient time. The term metaheuristics were first used by Glover [46], the prefix ‘meta’ means higher lever or beyond in Greek, and ‘heuristics’ means to discover or to find. Therefore, metaheuristics mean a general-purpose algorithm for high-level discovery approximation solutions.

2.3.2. Types of metaheuristics

From the 1960s to the present, various metaheuristic algorithms have been proposed as approximate solutions. These metaheuristics can be categorized in a wide variety of ways depending on the viewpoint, such as the number of candidate solutions to be used in each iteration, and the searching mechanism to find the optimal solution. In this chapter, the metaheuristic optimization solvers were classified as follows based on the phenomenon imitated by the metaheuristic algorithm.

(1) Evolutionary algorithm (EA) that imitates the evolutionary process of nature

The evolutionary process of nature is not only due to inevitability (rules), but also to coincidence (random or probability). The evolutionary algorithm that applies such a phenomenon to the search for a solution corresponds to Table 2-1.

Table 2-1. Examples of metaheuristic algorithms of evolutionary algorithm (EA) to imitate the evolutionary process of nature.

Year	Algorithm	Reference
1965	Evolutionary strategy (ES)	[47,48]
1966	Evolutionary programming (EP)	[49]
1975	Genetic algorithm (GA)	[50]
1992	Genetic programming (GP)	[51]
1995	Differential evolution (DE)	[52]

(2) Algorithm that mimics the behavior of living organisms living in a crowd

The algorithm that mimics the behavioral patterns of organisms that live in swarms or colony such as ants, bees, fish, and birds is classified in detail in Table 2-2.

Table 2-2. Examples of metaheuristic algorithms to mimic the behavior of living organisms living in a crowd.

Year	Algorithm	Reference
1992	Ant colony optimization (ACO)	[53]
1995	Particle swarm optimization (PSO)	[54]
2001–2002	Bee colony optimization (BCO)	[55,56]
2005	Artificial bee colony (ABC)	[57]

(3) Algorithm that imitates natural and social phenomena

Algorithms that mimic annealing in thermodynamics, human memory processes, and chord adjustment processes in music belong to this category as detailed in Table 2-3.

Table 2-3. Examples of metaheuristic algorithms to imitate natural and social phenomena.

Year	Algorithm	Reference
1983	Simulated annealing (SA)	[58]
1986	Tabu search (TS)	[46]
2001	Harmony search (HS)	[59]

(4) Algorithm that searches the neighborhood by systematic iteration

In addition, there are algorithms that search the neighborhood by systematic iteration that moves from the current solution area to the adjacent solution area in order to improve the objective function as shown in Table 2-4.

Table 2-4. Examples of metaheuristic algorithms to search the neighborhood by systematic iteration.

Year	Algorithm	Reference
1981	Iterated local search (ILS)	[60]
1997	Variable neighborhood search (VNS)	[61]
1998	Guided local search (GLS)	[62]

2.3.3. Differential evolution (DE)

Differential evolution (DE) was proposed by Storn and Price in 1995 [52,63] and corresponds to an evolutionary algorithm that mimics the evolutionary process of nature in metaheuristics. The basic idea is to allow a better individual to survive by arbitrarily selecting multiple individuals within the population, generating new individuals based on these differences, and comparing the new individuals with those within the generation. Here, an individual to be compared within a generation is called a target individual, and an individual newly generated from a difference between individuals within a generation for comparison is called a trial individual. Test individuals corresponding to each target individual are generated, and the excellent individual survives as the target individual of the next generation. As shown in Fig. 2-6, the process of mutation, crossover, and selection is mainly repeated to leave the good quality of individuals in the next generation and proceed with the search. In the latter section, each process of the differential evolution algorithm will be explained.

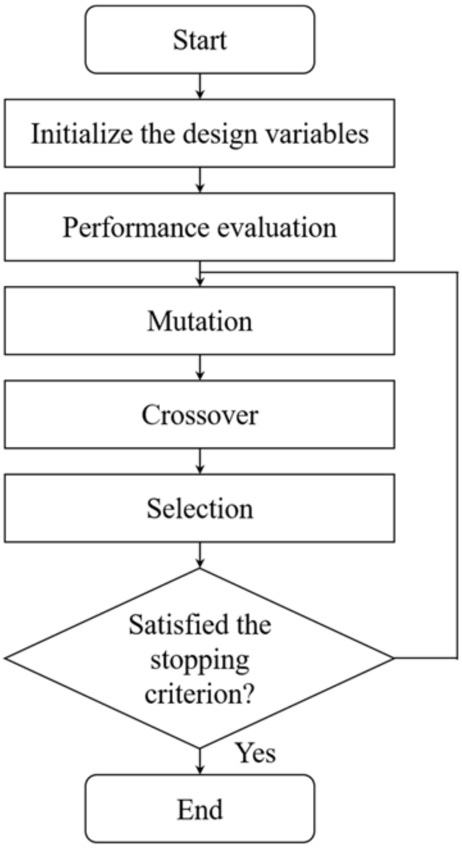

Fig. 2-6. Flow chart of differential evolution algorithm proposed by Storn and Price (1995) [52,63].

2.3.3.1 Optimization problem

An optimization problem is to find a solution that maximizes or minimizes an objective function under given constraints. Optimization is often used in real-life problems that occur in various fields such as science, engineering, business administration, and economics. It is solved by mathematically defining the objective function and constraints as shown in Equation. (2-16) according to the characteristics of the problem to be solved.

$$\begin{aligned} \textit{Minimize} \quad & f(\mathbf{x}) \\ \textit{Subject to} \quad & g_j(\mathbf{x}) \geq 0 \; (j = 1, \dots, m) \\ & h_k(\mathbf{x}) = 0 \; (k = 1, \dots, p) \\ & \mathbf{x}_l \leq \mathbf{x} \leq \mathbf{x}_u \\ \textit{where} \quad & \mathbf{x} = (x_1, x_2, \dots, x_n) \end{aligned} \tag{2-16}$$

Where the $f(\mathbf{x})$ is the objective function, the $g(\mathbf{x})$ is the inequality constraints, the $h(\mathbf{x})$ is the equality constraints, the $\mathbf{x}$ is the design variables or free variables to be chosen by optimization solver, the $\mathbf{x}_l$ is the lower limitation constraint on design variables of $\mathbf{x}$, and the $\mathbf{x}_u$ is the upper limitation constraint on design variables of $\mathbf{x}$.

2.3.3.2 Initialization

An individual of $\mathbf{x}_{i,g}$ is arbitrarily generated for the initialization as shown in Equation. (2-17). Here, N_P indicates the number of individuals and N_g indicates the number of generations. Therefore, individuals in D-dimensional can be expressed as shown in Equation. (2-18).

$$\mathbf{x}_{i,g} \; (i = 1,2, \dots, N_p, g = 1,2, \dots, N_g) \tag{2-17}$$

$$\mathbf{x}_{i,g} = \left(x_{i,j,g}\right) \; (j = 1,2, \dots, D) \tag{2-18}$$

If the upper and lower limits of an individual in the j-dimension are U_j and L_j, respectively, they can be randomly generated from the distribution of the range of (L_j, U_j) and initialized by the following Equation. (2-19).

$$x_{i,j,1} = rand_j(0,1)\left(U_j - L_j\right) + L_j(i = 1,2, \dots, N_p, j = 1,2, \dots, D) \tag{2-19}$$

2.3.3.3 Mutation

Once the initial population of individuals has been generated, N_P individuals are created for the test. In g generation, a test individual corresponding to each target individual is generated. Therefore, it is necessary to create a differential mutation. Mutations are generated by arbitrarily selecting two individuals and adding their scaled difference to an arbitrarily selected third individual as shown in

Fig. 2-7.

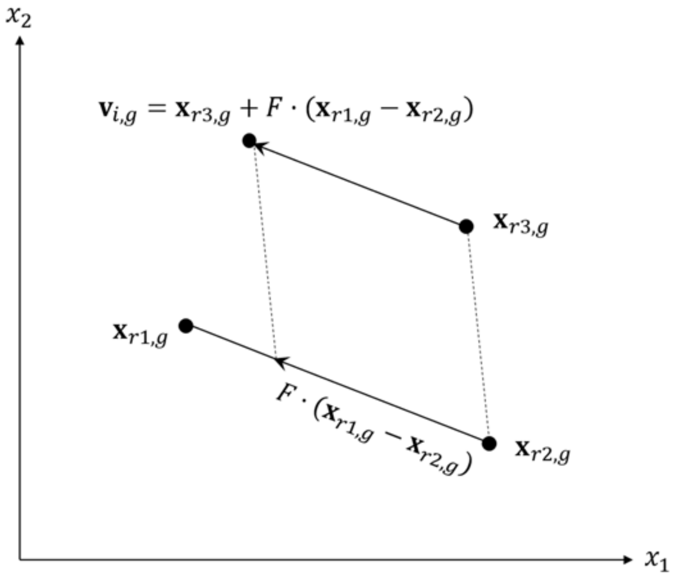

Fig. 2-7. Generation of differential mutation in DE algorithm [52,63].

The generated mutation can be expressed as an Equation. (2-20). Here, F is a scale factor, which is a parameter to change the moving length and adjusts the intensity of the search. The scaled difference vector of $F \cdot (\mathbf{x}_{r1,g} - \mathbf{x}_{r2,g})$ is the difference between arbitrarily generated vectors within a population, and thus, the more diverse the population, the more diverse directions, and lengths can be guaranteed.

$$\mathbf{v}_{i,g} = \mathbf{x}_{r3,g} + F \cdot (\mathbf{x}_{r1,g} - \mathbf{x}_{r2,g}) \tag{2-20}$$

Where the $\mathbf{v}_{i,g}$ is the trial vector, $\mathbf{x}_{r3,g}$ is the base vector, $\mathbf{x}_{r1,g} - \mathbf{x}_{r2,g}$ is the difference vector, and the F is the scale factor.

2.3.3.4 Crossover

In the DE algorithm, a crossover is adopted to compensate for the differential mutation. As shown in Fig. 2-8, the mutation vector of $v_{i,g}$ is crossed with the target vector of $x_{i,g}$ which is the parent individual, and the candidate vector of $u_{i,g}$ which denotes the child individual is obtained.

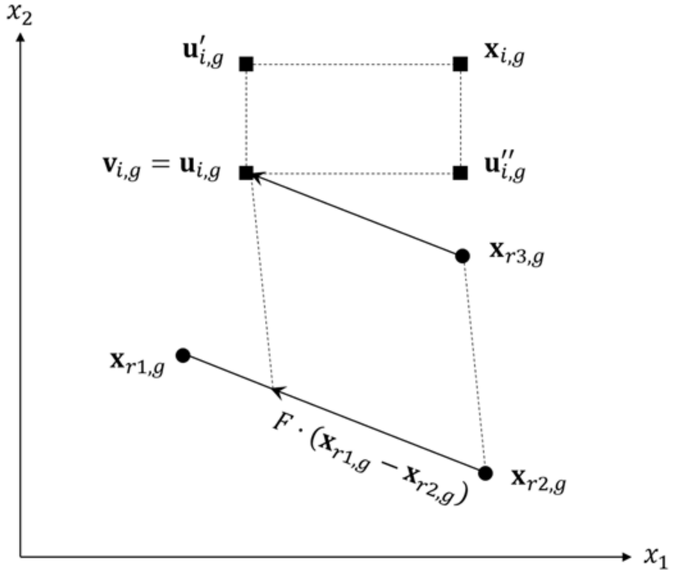

Fig. 2-8. Three candidate vectors of test individuals ($\mathbf{u}_{i,g}(= \mathbf{v}_{i,g}), \mathbf{u}'_{i,g}, \mathbf{u}''_{i,g}$) by crossover in DE algorithm [52,63].

There are several types of the way how to crossover, however when using the binomial crossover, the candidate vector is determined as shown in Equation. below. Here, $C_r \in [0,1]$ indicates the mutation rate of the probability that the target vector or mutation vector is selected. Also, $rand_j(0,1)$ represents a random number, and j_{rand} represents a natural number randomly selected in the range of $[1, D]$ that maximizes the D-dimension of the searching domain. In Equation. (2-21), the condition of $j = j_{rand}$ means that at least one individual inherits the mutation vector in order to prevent the candidate vector generated by the crossover from matching the target vector.

$$\mathbf{u}_{i,g} = \begin{cases} \mathbf{v}_{i,j,g} \ (rand_j(0,1) \leq C_r \cup j = j_{rand}) \\ \mathbf{x}_{i,j,g} \ (otherwise) \end{cases} \tag{2-21}$$

2.3.3.5 Selection

When a test individual of $\mathbf{u}_{i,g}$ is generated by mutation and crossover, a better individual is selected and survives as an individual for the next generation through the comparison with the target individual of $\mathbf{x}_{i,g}$ based on Equation. (2-22). Once the survival selection is complete, the same process is repeated until the termination conditions are met. The termination conditions may include the maximum number of generations, the degree of improvement of the solution, and the maximum calculation time.

$$\mathbf{x}_{i,g+1} = \begin{cases} \mathbf{u}_{i,g} \ (f(\mathbf{u}_{i,g}) \le f(\mathbf{x}_{i,g})) \\ \mathbf{x}_{i,g} \ (otherwise) \end{cases} \tag{2-22}$$

2.3.4. Epsilon (ε) constraint method

Constraint optimization problems generally have inequality constraints, equality constraints, and upper and lower limit constraints of design variables, and are defined as in Equation. as stated in the previous section. There are various processing methods for handling constraints, such as generating only possible solutions that satisfy the constraints in the solution searching process, easily ignoring non-possible solutions that exceed the constraints, and giving penalties when the solutions are exceeding the constraints.

In the epsilon (ε) constraint method [64,65], the degree of acceptance of constraints of $\varphi(\mathbf{x})$ is introduced to express how much the constraint deviates. The degree of acceptance of constraints of $\varphi(\mathbf{x})$ is a function that satisfies the following Equation. (2-23). Here, $D_{feasible}$ means a feasible region that satisfies all the constraints.

$$\begin{cases} \varphi(\mathbf{x}) = 0 \ (\mathbf{x} \in D_{feasible}) \\ \varphi(\mathbf{x}) > 0 \ (\mathbf{x} \notin D_{feasible}) \end{cases} \tag{2-23}$$

Therefore, Equation. (2-24) can be defined and the objective function is evaluated based on the satisfaction of the constraints of the design variables.

$$evaluate\ f(\mathbf{x}) = \begin{cases} f(\mathbf{x}) & (\mathbf{x} \in D_{feasible}) \\ f(\mathbf{x}) + \varphi(\mathbf{x}) & (\mathbf{x} \notin D_{feasible}) \end{cases} \tag{2-24}$$

The degree of acceptance of constraints of $\varphi(\mathbf{x})$ defines the degree of violation in the j constraint based on the penalty function as shown in Equation. (2-25) and Equation. (2-26). In Equations. (2-25)–(2-26), P denotes a constant.

$$\varphi(\mathbf{x}) = max\left\{\max_j\{0, g_j(\mathbf{x})\}, \max_j |h_j(\mathbf{x})|\right\} \tag{2-25}$$

$$\varphi(\mathbf{x}) = \sum_j max\{0, g_j(\mathbf{x})\}^P + \sum_j |h_j(\mathbf{x})|^P \tag{2-26}$$

On the set of the objective function and the degree of acceptance of constraints (f, φ), if the degree of acceptance of constraints of φ is less than ε, priority is given to the magnitude relationship of the objective function of f. In other cases, the magnitude relationship of the degree of acceptance of constraints of φ is prioritized. This process is called ε level comparison [64,65]. If the results of the objective function at points x_1 and x_2 are f_1 and f_2, and the degree of acceptance of constraints are φ_1 and φ_2, then the normal magnitude relationship of $<$ and $\leq$ corresponding to the set of the objective function and the degree of acceptance of constraints (f_i, φ_i) is compared in the ε level magnitude relationship as defined in Equation (2-27) and Equation (2-28) below.

$$(f_1, \varphi_1) <_\varepsilon (f_2, \varphi_2) \Leftrightarrow \begin{cases} f_1 < f_2 & (\varphi_1, \varphi_2 \leq \varepsilon) \\ f_1 < f_2 & (\varphi_1 = \varphi_2) \\ \varphi_1 < \varphi_2 & (otherwise) \end{cases} \tag{2-27}$$

$$(f_1, \varphi_1) \leq_\varepsilon (f_2, \varphi_2) \Leftrightarrow \begin{cases} f_1 \leq f_2 & (\varphi_1, \varphi_2 \leq \varepsilon) \\ f_1 \leq f_2 & (\varphi_1 = \varphi_2) \\ \varphi_1 < \varphi_2 & (otherwise) \end{cases} \tag{2-28}$$

2.3.5. Epsilon-constrained differential evolution with random jumping (εDE-RJ)

Epsilon constrained differential evolution with random jumping (εDE-RJ) is the algorithm proposed by Ikeda et al., [66] to improve the algorithm of b, which is the addition of epsilon constrained differential evolution (εDE) to prevent it from being captured in a local minimum. The εDE-RJ is a solution searching method that improves the searching performance of constrained optimization problems by combining the DE algorithm, the ε constraint method, and the random jumping. When the target individuals in the population of $\mathbf{x}_{r3,g}$ and $\mathbf{x}_{r4,g}$ are similar, the following Equation. (2-29) is applied to Equation. (2-20). The validity of the εDE-RJ method has been already evaluated in previous studies [67,68].

$$\mathbf{x}_{r3,g+1} = \begin{cases} \mathbf{x}_{r1,g} + F \cdot \left(\mathbf{x}_{r2,g} - \mathbf{x}_{r4,g}\right) & (|\mathbf{x}_{r2,g} - \mathbf{x}_{r4,g}| > 1.0 \times 10^{-3}) \\ \mathbf{x}_{r1,g} + rand_j(0,1) & \left(|\mathbf{x}_{r2,g} - \mathbf{x}_{r4,g}| \leq 1.0 \times 10^{-3}\right) \end{cases} \tag{2-29}$$

Chapter 3. Artificial neural network models for building energy systems

Chapter 3.
Artificial neural network models for building energy systems

Based on:

D. Lee, R. Ooka, S. Ikeda, W. Choi, Artificial neural network prediction models of stratified thermal energy storage system and borehole heat exchanger for model predictive control, Sci. Technol. Built Environ. 25 (2019) 534–548. https://doi.org/10.1080/23744731.2018.1557464.

3.1. Introduction

Buildings have a long-term life cycle that takes at least several decades from being constructed to being destroyed. Most of the energy consumption of buildings is consumed by HVAC systems, and the efficient operation of such an energy-consuming HVAC systems greatly contributes to energy cost savings as well as reduction of greenhouse gas emissions. It is known that it is desirable to introduce active energy storage systems such as thermal energy storage (TES) as well as renewable energy source systems such as ground-source heat pump (GSHP) systems. Also, it is important to adopt the optimal operational strategy of these systems for efficient energy use of building energy systems.

In this regard, model predictive control (MPC) has received a significant attention as an optimal control strategy for building energy systems [68,69]. The MPC is well-suited control strategy especially for energy storage systems and renewable energy systems since it determines the control inputs by solving an optimization problem consecutively based on the prediction of the system's future behavior in a certain future time horizon [36]. However, to establish a MPC strategy, prediction models representing the systems present in the building facility are needed. The construction of these prediction models is the most fundamental and time-consuming part of the MPC design process and the model accuracy hugely affect the MPC's efficiency [71].

Considering the intrinsic nature of the MPC problem, which involves iterative calculations, calculation time of prediction while maintaining a high prediction accuracy is a critical issue. According to the ASHRAE guideline [23], prediction models to represent the building energy systems can be constructed by three main approaches: white-box models, grey-box models, and black-box models. Comprehensive comparison of the advantages and disadvantages of each modeling method can be found in previous researches [6,72]. Based on the analysis from these previous publications, generally, black-box models have lower complexity and involve fewer parameters and can be constructed without an in-depth understanding of the complex system physics. The huge benefits of black-box models are that they can deal with the nonlinearities in the system with high speed and are therefore especially well-suited for MPC design [7].

Further, among the numerous black-box models available, artificial neural networks (ANNs) have been used most commonly for the predictions and control of HVAC systems [29]. Using a ANN prediction model trained by the historical data is one way to overcome the drawback of the high computational load while ensuring accurate predictions at relatively high speeds during MPC applications.

However, ANN models have a typical drawback that reliable predictions cannot be assured when the data points lie outside the range covered by the training dataset. Thus, the utilization of a comprehensive training dataset that captures the system dynamics quantitatively as well as qualitatively is essential. Furthermore, when using ANN models, the researcher’s ability to establish and process a suitable training dataset and design an effective training structure is the most influential factor, as there are no reliable guidelines for determining the appropriate training structure. For these reasons, the final trained model is usually selected depending on the researcher’s experience in accordance with their research subject and purpose.

For instance, in previous research [73], various parameters of the input data and the training structure were appropriately determined through a sufficient trial and error approach for the prediction of the performance of a central heating and cooling plant. Incorrect training using an improper training dataset may lead to errors in prediction. Thus, the training method and dataset, namely, the parameters to be used as the input data, and the structure of the ANN should be established with care.

Therefore, in this chapter, an appropriate method for constructing ANN models of the stratified chilled water TES system and the borehole heat exchanger (BHE) of a GSHP system for use with MPC applications was investigated.

3.2. Thermal energy storage

3.2.1. Model description

In order to generate the historical data of stratified chilled water TES tank, a multi-node model was used [74,75]. The entire TES tank was discretized into 20 nodes and each divided node was considered as fully mixed state so that the vertical temperature stratification can be modeled. A schematic of the TES system for charging and discharging modes is shown in Fig. 3-1. Inside the stratified TES tank, temperature stratification is occurred by the water density difference. The inflowing water entering the tank from the heat source and load side depending on the charging or discharging operation naturally streams into the i-th node where its density nearly matches. However, in this study, the inflowing position of the circulating water coming from the heat source side and the load side was fixed, and simultaneous operation of charging and discharging mode was not considered.

During the charging operation, the inflowing water from the heat source side enters the bottom node inside the tank. The temperature of the inlet water (T_C) to the TES tank from the heat source was assumed as 4 °C. During the discharging operation, the returning water from the building load side flows into the top node inside the tank. The water temperature returning to the TES from the load side (T_L) was assumed to be 14 °C. Also, the top node was denoted as node 1 while the bottom node was labeled as node 20. The initial temperature of the TES tank was set to 14 °C.

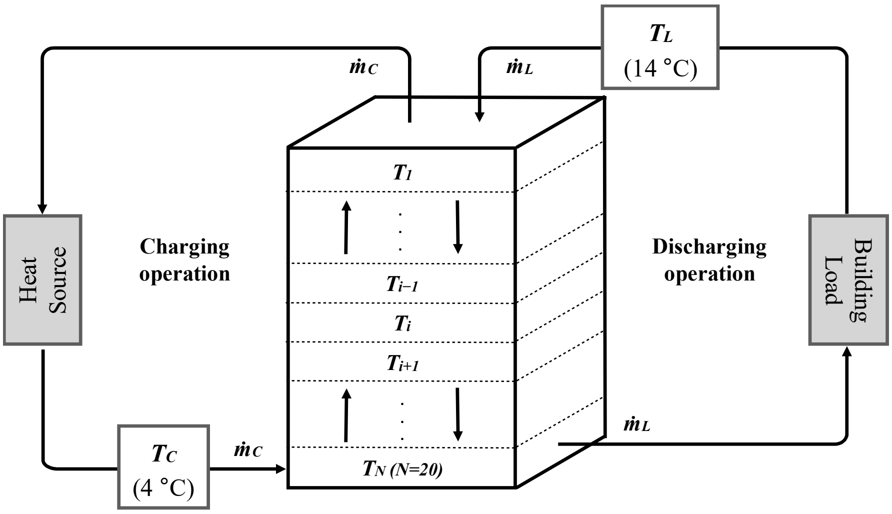

Fig. 3-1. Multi-node model of stratified chilled water TES.

The Equations (3-1)–(3-6) describe the temperature variation in each node subject to the inlet water temperature (T_C and T_L), mass flow rate of source and load sides ($\dot{m}_C$ and $\dot{m}_L$), and the surrounding air temperature (T_a). Since the inflowing water is introduced in a fixed position, the energy balance equation at each node can be summarized by that of the top node where the chilled water flows from the heat source side, the bottom node where the returning water flows from the load side, and the i-th node therebetween.

The Equations (3-1) and (3-2) show the energy balance equation of the top node during the charging operation and discharging operation, respectively. In charging mode, the chilled water flows into the bottom node and continuously flows upward, so that the equation can be established with the temperature difference between the second node (T_2) and mass flow rate of the source side ($\dot{m}_C$). On the other hand, in discharging mode, the returning water directly enters the top node. Therefore, the equation can be defined with the temperature difference between the water temperature of returning water from the load side (T_L) and its mass flow rate ($\dot{m}_L$).

$$m_1\frac{dT_1}{dt}=\frac{UA_1}{c_f}(T_a-T_1)+\dot{m}_C(T_2-T_1) \tag{3-1}$$

$$m_1\frac{dT_1}{dt}=\frac{UA_1}{c_f}(T_a-T_1)+\dot{m}_L(T_L-T_1) \tag{3-2}$$

The energy balance equation on the i-th node in charging and discharging operation can be expressed as Equation (3-3) and Equation (3-4), respectively. The temperature variation at the i-th node can be derived based on the temperature difference between the upper and lower nodes and the mass flow rate.

$$m_i\frac{dT_i}{dt}=\frac{UA_i}{c_f}(T_a-T_i)+\dot{m}_C(T_{i+1}-T_i) \tag{3-3}$$

$$m_i\frac{dT_i}{dt}=\frac{UA_i}{c_f}(T_a-T_i)+\dot{m}_L(T_{i-1}-T_i) \tag{3-4}$$

In charging operation, the chilled water streams into the bottom node so that the energy balance equation on the bottom node in charging operation mode can be described subject to the temperature difference between the chilled water temperature from the heat source side (T_C) and its mass flow rate ($\dot{m}_C$) as shown in Equation (3-5). The temperature change of the bottom node in discharging operation can be expressed by the temperature difference between the upper node (T_{19}) and the mass flow rate of the load side ($\dot{m}_L$) as shown in Equation (3-6).

$$m_{20}\frac{dT_{20}}{dt}=\frac{UA_{20}}{c_f}(T_a-T_{20})+\dot{m}_C(T_C-T_{20}) \tag{3-5}$$

$$m_{20}\frac{dT_{20}}{dt}=\frac{UA_{20}}{c_f}(T_a-T_{20})+\dot{m}_L(T_{19}-T_{20}) \tag{3-6}$$

The node which has information of quantities of partial tank volume was assumed to represent a fully mixed state. Thus, the nonlinear temperature stratification in the TES tank due to the density difference is simplified to a linear behavior. The temperature change of 20 nodes was solved by the fourth-order Runge-Kutta method [76,77] based on the energy balance equations described above. The calculation time step was set to 10 sec. Also, the coefficient of overall heat transmission of the wall of the TES tank (U) was assumed to be 0.5 W/(m^{2}K).

3.2.2. Training dataset

As shown in Fig. 3-2, a suitable training dataset of 2,000 operation patterns that covers a wide range of charging and discharging amount for the stratified TES tank were constructed. In the literature of CASCADEIII 2003 [78], a monthly average cooling load by the different building usage in Japan is open to the public. The 2,000 patterns of the TES operation scheme was constructed based on the monthly average cooling load data for August, within the executable range referred from the literature [66]. Fig. 3-3 describes the results of a 1-day-long simulation of the temperature distribution of all the nodes based on 1 pattern of the TES operation among the 2,000 patterns. In conclusion, the 960,000 data points calculated on an hourly basis (24 h × 2,000 patterns × 20 nodes) were obtained as the training dataset.

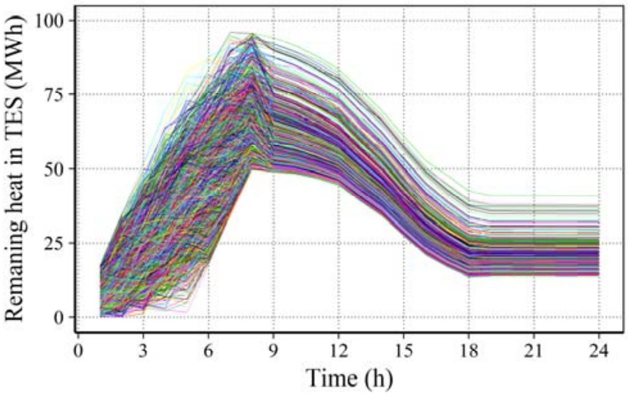

Fig. 3-2. 2,000 operation patterns for the stratified TES tank.

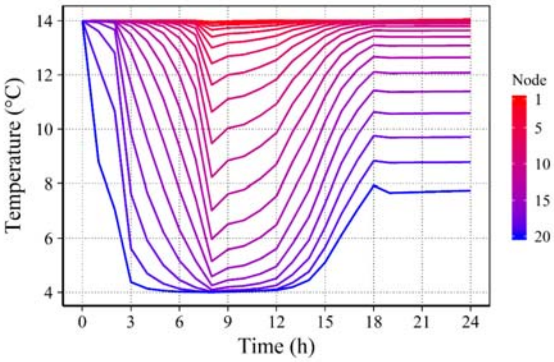

Fig. 3-3. Temperature distributions of 20 nodes inside stratified TES tank after 1-day-long calculation (corresponding to 1 operation pattern among the Fig. 3-2).

3.3. Borehole heat exchanger

3.3.1. Model description

To date, analytical response models such as the infinite line source model [79,80] and infinite cylindrical source model [79] have been utilized to recreate the temperature response of BHE. However, in such models, the heat transfer inside the BHE is simplified by using the steady-state thermal resistance without considering the heat capacity of the BHE itself. Hence, the early-time response and short-term changes subject to an abrupt heat flux change are not guaranteed to be accurate. Given the dynamic changes in thermal loads, the resultant temperature response is either overestimated or underestimated.

On the other hand, when detailed numerical models are used, drawbacks in classical analytical models can be overcome, because they consider the shape and thermal properties of BHE components. Thus, a three-dimensional numerical model based on the finite element method was constructed to achieve high accuracy. However, a numerical model for BHE has a disadvantage of a huge computational load because of BHE's extremely slender geometrical characteristics. As an alternative to reduce the computational load for MPC applications, the feasibility of using an ANN model was examined in this chapter.

The physical properties of porous material of the ground must be considered by that of solid and fluid simultaneously. Therefore, in order to solve these difficulties in analysis, all properties of the ground element were assumed as one ideal bulk property based on the following equation. In Equation (3-7), the ε represents the porosity of soil, and the subscript b, f, and s denote the bulk, fluid, and solid properties, respectively.

$$\rho_b c_b = \varepsilon \rho_f c_f + (1-\varepsilon)\rho_s c_s \tag{3-7}$$

Based on the law of Hagen–Poiseuille flow [81,82], the fluid flow in the U-tube was simulated as a one-dimensional (1D) flow element. The 1D flow element was applied for the center of the pipe, and the fluid was assumed to be a pseudo-fluid to consider the turbulent movement in the actual pipe flow. As listed in Table 3-1, pseudo-fluid has a low thermal capacity of 1×10^{-6} MJ/(m^{3}K) and notably high thermal conductivity of 1000 W/(mK). Since the high thermal conductivity of this pseudo-fluid occurs in anisotropic and its thermal conductivity in the vertical direction is zero, it is possible to reproduce turbulent flow dominant in the radial direction. Except for the pseudo-fluid in the 1D flow element, the boundary condition was set by the physical properties of general water. Besides the 1D flow elements in the U-tube, the numerical model is governed by the equation of energy conservation, as shown in Equation (3-8). Also, further details regarding numerical modeling using the 1D flow element and its validation using experimental data can be found in [83].

$$\rho_b c_b \frac{\partial T}{\partial t} - \nabla \lambda_b \nabla T = S_T \tag{3-8}$$

Table 3-1. Material properties utilized in numerical siumulation of BHE.

	Volumetric thermal capacity (MJ/(m^{3}K))	Thermal conductivity (W/(mK))
Soil (bulk)	2.6	1.8
Fluid (water)	4.2	0.6
Grout backfill	2.1	1.6
U-shaped pipe	1.8	0.45
Pseudo-fluid in tube	1×10^{-6}	1,000

The calculation domain of BHE has 60 m in length, 60 m in width, and 150 m in depth as shown in Fig. 3-4. The height of the BHE was set as 100 m so that the axial heat transfer at the bottom end of BHE can be properly considered. The radius of the borehole was 0.062 m, the inner radius of the U-tube leg was 0.013 m, the pipe thickness was 0.003 m, and the center distance between the inlet and outlet of the U-tube (shank space) was set to 0.056 m. The numerical model has a total of 767,084 mesh elements, and more fine meshes were adopted for the BHE and near the depth of 100 m to consider the steep temperature gradient.

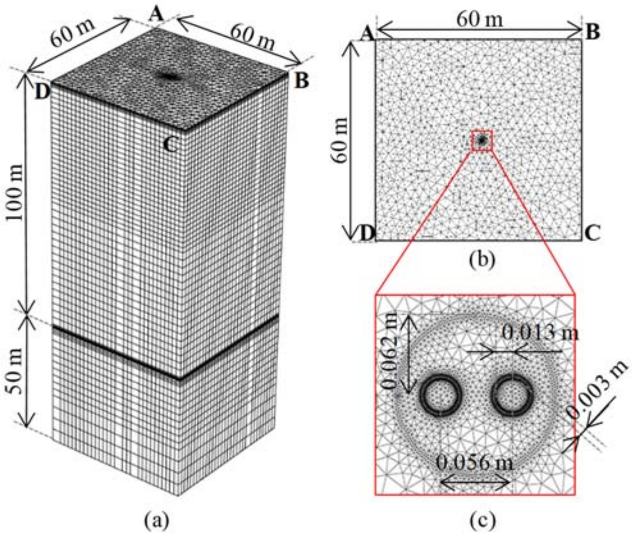

Fig. 3-4. Numerical model for BHE: (a) Overview, (b) Ground plan, and (c) Magnified plan of area around BHE.

All the boundary conditions are listed in Table 3-2. The surface of the top layer was set to be adiabatic. A Dirichlet condition of 17 °C was assigned to the lateral and bottom surfaces. The U-tube legs were modeled using a one-dimensional linear element as stated in the earlier section. In addition, a time varying Dirichlet condition was assigned to the BHE inlet element based on Equation (3-9). In Table 3-2, the negative and positive signs for the well-type of boundary conditions represent the inflow and outflow to the numerical model domain, respectively. Furthermore, the initial temperature of the entire model domain was set to 17 °C.

Table 3-2. Boundary conditions for numerical simulation of BHE.

Surface or Element	Condition	Value
Top surface	Adiabatic	-
Lateral surface	Dirichlet	17 °C
Bottom surface	Dirichlet	17 °C
BHE inlet (linear element)	Dirichlet (Time varying)	Equation (3-9)
	Well-type	–20 L/min
BHE outlet (linear element)	Well-type	+20 L/min

The time varying boundary condition assigned to the BHE inlet is described in Equation (3-9). The inlet fluid temperature of the BHE at the current time step (T_{in}^{t}) was determined by retrieving the outlet fluid temperature at the previous time step (T_{out}^{t-1}) and the heat rate at the current time step (q_{BHE}^{t}), which is transferred from the GSHP to the circulating fluid. The sign of the second term on the right-hand side in Equation (3-9) is negative when the GSHP operates in the heating mode and positive when the operating mode is cooling. However, in this study, only the heating operation mode was examined. Also, the calculation time step was set to 1 h.

$$T_{in}^{t} = T_{out}^{t-1} \pm q_{BHE}^{t}/\rho_f c_f \dot{V}_f \tag{3-9}$$

3.3.2. Training dataset

The heat rates assigned to the BHE (q_{BHE}^{t}) were generated with the simple random sampling method with the extracted BHE heat rates (q_{BHE}^{t}) within the probabilistic range of 0–4.3 kW to ensure the wide operational range of 0–4.3 kW. The data were generated for 100 weeks on a weekly basis using 1-h intervals. Hence, the total number of data points was 16,800 (24 h × 7 days × 100 weeks). The data obtained by substituting the 16,800 data points during the numerical simulation were used as the training dataset to construct the ANN model.

Moreover, when the numerical model was simulated all at once continuously with the whole 100 weeks data of the extracted BHE heat rates (q_{BHE}^{t}), the training data corresponding to the change from the initial ground temperature were found to be insufficient while assuming the initial ground temperature was set as 17 °C. Thus, the numerical simulation was conducted 10 times separately by dividing the data into 10-week intervals. The Fig. 3-5 shows an example of 10 weeks of randomly generated heat rate patterns and the Fig. 3-6 shows the simulation results of the BHE inlet and outlet temperature as calculated using the 10-week heat rate pattern described in Fig. 3-5.

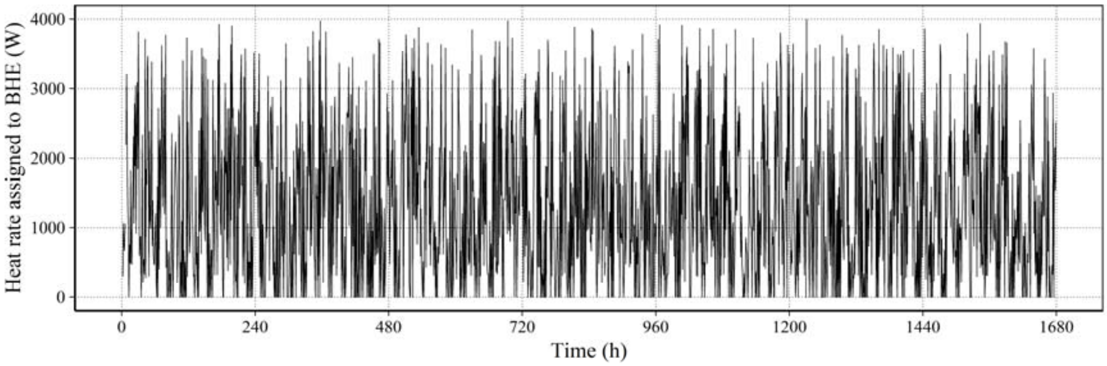

Fig. 3-5. Sample 10-week heat rate pattern for numerical simulation of BHE.

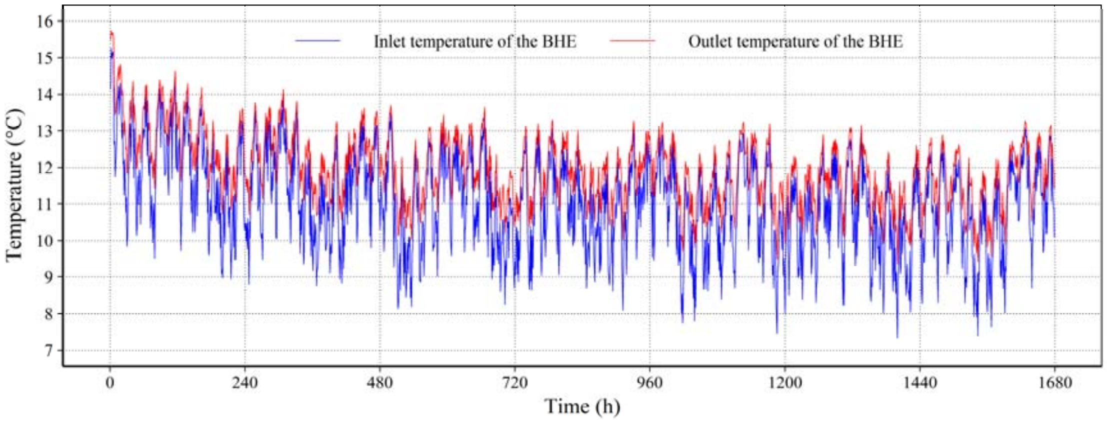

Fig. 3-6. Temperature changes as determined using numerical model and sample 10-week heat rate pattern of BHE corresponding to the heat rate in **Fig. 3-5**.

3.4. Construction of ANNs

3.4.1. Training conditions

Several types of neural network structures have been reported in the literature [41]. Among them, the feed-forward type of neural network is the most generic structure and utilized most widely. The Fig. 3-7 shows a schematic diagram of a multilayer feed-forward-type neural network structure, which consists of two hidden layers. The neuron is the basic processor to receive a number of inputs from the other neurons with weighted interconnections (w) and generate one output.

In this study, a general feed-forward type of neural network was considered, and the back-propagation algorithm was utilized for ANN construction. Also, the sigmoid function and linear function was applied as an activation function for hidden layers and output later, respectively. The number of hidden layers and their neurons can be determined differently, depending on the complexity and nature of the problem at hand.

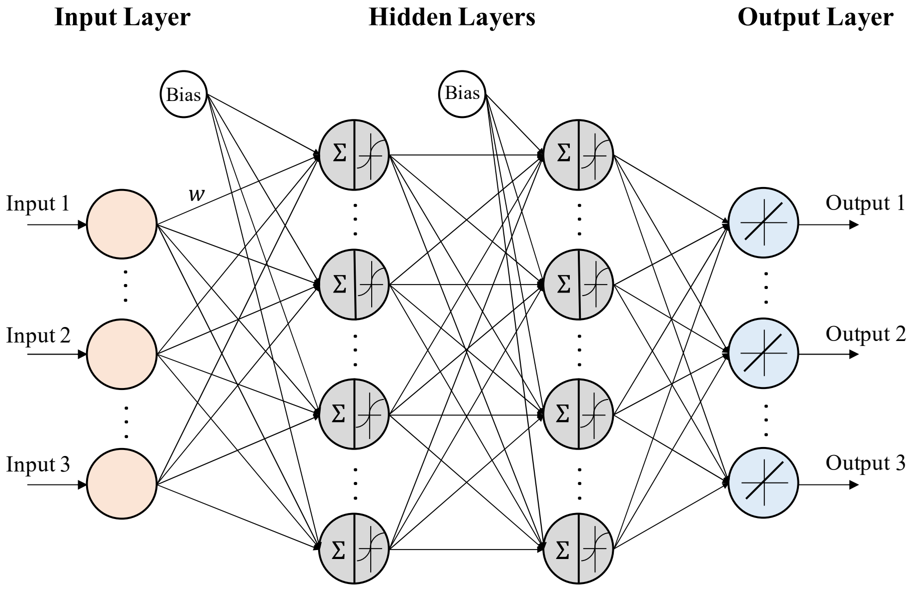

Fig. 3-7. Structure of multilayer (four-layer) feed-forward type of artificial neural network.

The Levenberg–Marquardt (LM) algorithm [84,85] was applied for the training optimization algorithm using the software of MATLAB. The entire dataset was normalized in a range of [–1, 1], since it is know that more efficient training can be performed when the input and target parameters are normalized [86]. When the training was completed, the output parameters were back into the original units. During the training, the dataset was divided into three groups in a random manner for the training (70%), validation to prevent overfitting (15%), and the evaluation (15%) purposes.

3.4.2. Case study

3.4.2.1 TES

Total six cases were examined with the different combinations of input parameters as shown in Table 3-3. The cases of TES 1 to TES 3 commonly included the previous time step of top and bottom node temperatures (T_1^{t-1} and T_{20}^{t-1}) and the current time step of heat remaining amount (Q_{TES}^t). However, each case has a difference in input parameters whether to consider the average tank temperature (T_{avg}^{t-1}) and the temperature distributions for all nodes ($T_1^{t-1}, T_2^{t-1}, \cdots, T_{19}^{t-1}$, and T_{20}^{t-1}) at the previous time step. In case of TES 4 to TES 6, the amount of heat remaining in the previous time step (Q_{TES}^{t-1}) was additionally considered in each of case TES 1 to TES 3 based on the assumption that more information would improve the prediction performance.

Table 3-3. Input and target parameters for ANN models of stratified TES.

Case	Input data	Target data
TES 1	$Q_{TES}^{t}, T_1^{t-1}, T_{20}^{t-1}$	T_1^t, T_{20}^t
TES 2	$Q_{TES}^{t}, T_1^{t-1}, T_{avg}^{t-1}, T_{20}^{t-1}$	
TES 3	$Q_{TES}^{t}, T_1^{t-1}, T_2^{t-1}, \cdots, T_{19}^{t-1}, T_{20}^{t-1}$	
TES 4	$Q_{TES}^{t-1}, Q^{t}, T_1^{t-1}, T_{20}^{t-1}$	
TES 5	$Q_{TES}^{t-1}, Q_{TES}^{t}, T_1^{t-1}, T_{avg}^{t-1}, T_{20}^{t-1}$	
TES 6	$Q_{TES}^{t-1}, Q_{TES}^{t}, T_1^{t-1}, T_2^{t-1}, \cdots, T_{19}^{t-1}, T_{20}^{t-1}$	

3.4.2.2 BHE

The prediction accuracy of ANN models to predict the outlet temperature of the BHE at the current time step (T_{out}^t) was examined in eight cases shown in Table 3-4 with the various combination of following input parameters: the outlet temperature of the BHE (T_{out}), the rate of heat extraction from the BHE (q_{BHE}), the cumulative amount of heat extracted by the BHE (Q_{BHE}), and the difference in the rates of heat extraction between consecutive time steps (Δq_{BHE}).

Table 3-4. Input and target parameters for ANN models of BHE.

Case	Input data	Target data
BHE 1	$T_{out}^{t-2}, T_{out}^{t-1}, q_{BHE}^{t-1}, q_{BHE}^{t}$	T_{out}^t
BHE 2	$T_{out}^{t-1}, q_{BHE}^{t}$	
BHE 3	$T_{out}^{t-2}, T_{out}^{t-1}, q_{BHE}^{t}$	
BHE 4	$T_{out}^{t-1}, q_{BHE}^{t-1}, q_{BHE}^{t}$	
BHE 5	$T_{out}^{t-1}, q_{BHE}^{t}, Q_{BHE}^{t}$	
BHE 6	$T_{out}^{t-2}, T_{out}^{t-1}, q_{BHE}^{t}, Q_{BHE}^{t}$	
BHE 7	$T_{out}^{t-1}, \Delta q_{BHE}^{t}$	
BHE 8	$T_{out}^{t-2}, T_{out}^{t-1}, \Delta q_{BHE}^{t-1}, \Delta q_{BHE}^{t}$	

3.5. Results and discussion

3.5.1. Evaluation index

To compare the prediction accuracy of each trained ANN model, following statistical indices were utilized: the coefficient of determination (R^2), the root mean square error (RMSE), and the coefficient of variation of the root mean square error (CVRMSE). The ASHRAE Guideline 14-2002 suggests using the R^2 and the CVRMSE to evaluate the surrogate models, and a model with more than 0.8 of R^2 and less than 30% of CVRMSE is a suitable [87]. The CVRMSE can be derived from the RMSE and capture the variability in the prediction error and model uncertainty. The RMSE and the CVRMSE were calculated using Equations (3-10) and (3-11), respectively.

$$\mathrm{RMSE} = \sqrt{\frac{1}{n}\sum\nolimits_{i=1}^{n}(y_i - \widehat{y_i})^2} \tag{3-10}$$

$$\mathrm{CVRMSE} = \frac{1}{\bar{y}}\sqrt{\frac{1}{n}\sum\nolimits_{i=1}^{n}(y_i - \widehat{y_i})^2} \times 100 = \frac{\mathrm{RMSE}}{\bar{y}} \times 100 \tag{3-11}$$

3.5.2. ANN selection for TES

3.5.2.1 Model evaluation

The results of R^2, RMSE, and CVRMSE indices for each case were investigated as shown in Fig. 3-8. All the cases showed a high R^2 results greater than 0.99, however, the results were differed in the CVRMSE. (Detailed results of model evaluation can be found in Appendix 1).

As a result, it was possible to predict the current outlet temperatures (T_1^t and T_{20}^t) with ease when the amount of heat remaining at the current time step (Q_{TES}^t) and the outlet temperatures at the previous time step (T_1^{t-1} and T_{20}^{t-1}) were known. Basically, the R^2 value showed a high result in every case with over than 0.99, however, the RMSE and CVRMSE could be hugely improved by adding a parameter of the tank average temperature at the previous time step (T_{avg}^{t-1}). Also, the information of the temperature distributions in all nodes at the previous time step ($T_1^{t-1}, T_2^{t-1}, \cdots, T_{19}^{t-1}$, and T_{20}^{t-1}) could help to improve the accuracy as the case of TES 3 showed better results compared to TES 2 case. Moreover, it was verified that additional input parameters of the heat remaining at the current time step (Q_{TES}^t) as well as that at the previous time step (Q_{TES}^{t-1}) can further increase the accuracy.

Regarding the training structure of the ANN model, it was confirmed that the prediction performance could be generally improved when the number of hidden layers and hidden neurons was increased except for few cases.

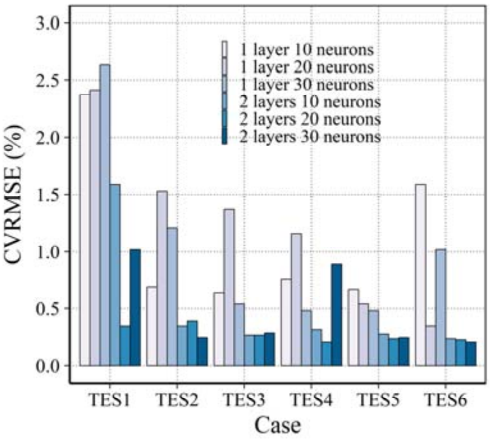

Fig. 3-8. Model evaluation with CVRMSE comparison in all cases for stratified chilled water TES system.

In conclusion, the ANN model of TES 6 case consists of two hidden layers and thirty neurons each showed the highest prediction performance, with the highest R^2 and the lowest RMSE and CVRMSE results. The Fig. 3-9 and Fig. 3-10 show the detailed evaluation results of the TES 6 case using the 15% of separated dataset.

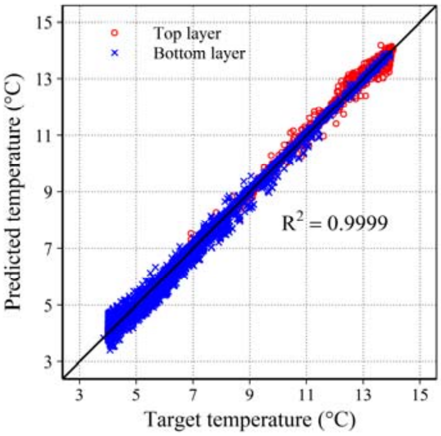

Fig. 3-9. Results of correlation analysis between predicted and target temperatures for selected ANN model (case TES 6) with two hidden layers and thirty neurons each.

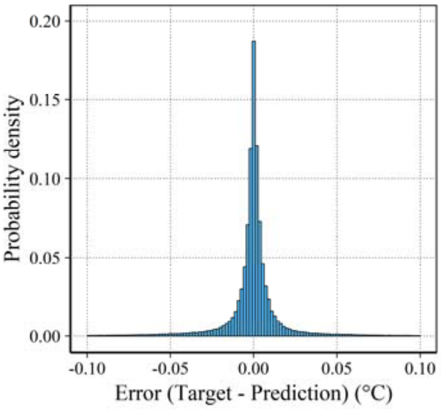

Fig. 3-10. Histogram of error between predicted and target temperatures for selected ANN model (case TES 6) with two hidden layers and thirty neurons each.

3.5.2.2 Computational cost

The computational cost of the selected ANN model (TES 6 case with two hidden layers and thirty hidden neurons) was confirmed in order to investigate its applicability for MPC framework. According to the paper by Serale et al., the prediction horizon for MPC is generally set as 24 h [14]. Therefore, the computational speed of the selected ANN to predict the target data for 24 h ahead was tested on a personal computer (Windows 10 64-bit machine with an Intel Core i7 4790 3.6 GHz processor and 8 GB RAM). As a results, given the fact that the ANN model took only 0.27 s and the physical model took 13 s, the computational cost was available to be reduced sharply by adopting an ANN model (see the Fig. 3-11). The time of 13 s from the physical model may seem very fast but this result refers only the time taken to perform the prediction. Any reductions in prediction speed can be a significant advantage in the MPC framework, since the MPC involves large amount of consecutive optimization calculations in each control time step.

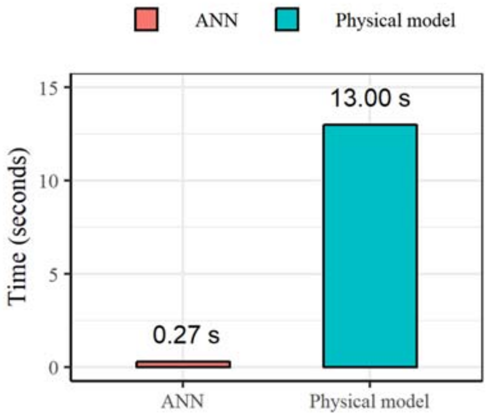

Fig. 3-11. Comparison of prediction speed between selected ANN and physical model for stratified chilled water TES system.

3.5.3. ANN selection for BHE

3.5.3.1 Model evaluation

The evaluation results of the different cases can be compared in Fig. 3-12 and also in Appendix 2. In the comparative results in different training structures, any meaningful difference of R^2, RMSE, and CVRMSE results were found. In the case of BHE 4, the heat extraction rate at the previous time step (q_{BHE}^{t-1}) was added in case of BHE 2 and showed a better prediction accuracy. In BHE 5 case, the cumulative heat extracted until the current time step (Q_{BHE}^{t}) was additionally considered in BHE 2 case and showed a better prediction accuracy. Given this fact, it can be inferred that the heat extraction rate and the cumulative heat extraction is a valid input parameter to predict the outlet temperature of the BHE system.

For BHE 7, the difference in the rates of heat extraction for the current and previous time steps (Δq_{BHE}^{t}) was additionally considered as an input parameter, however, showed the worst prediction accuracy of all the cases. Therefore, it can be inferred that the difference in the rates of heat extraction (Δq_{BHE}) is not an influential parameter and can be excluded in the training data. Similar to the case of BHE 7, the case of BHE 8 also considered the input parameter of the difference in the rates of heat extraction. However, in the latter case, the more information between the rates for the previous time step and the two-step-prior time step (Δq_{BHE}^{t-1}) and the outlet temperature at the two-steps-prior time step (T_{out}^{t-2}) was considered, therefore, it can be surmised that ANN considers more information about the parameter of the outlet temperature (T_{out}) and the difference in the rates of heat extraction (Δq_{BHE}^{t}) with the consecutive time steps similar to the current rate of heat extraction (Δq_{BHE}^{t}) itself.

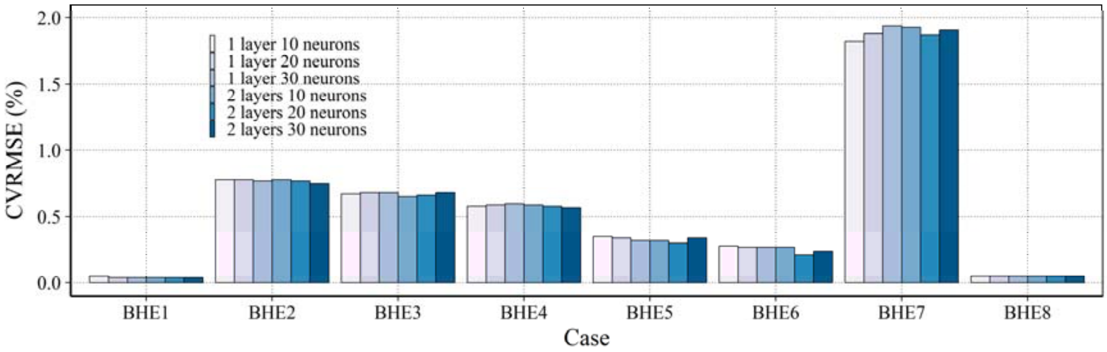

Fig. 3-12. Model evaluation with CVRMSE comparison in all cases for the BHE of GSHP system.

In conclusion, the ANN model that showed the best prediction performance was the case of BHE 1 consists of two hidden layers with thirty neurons each (R^2 value was 0.9999, RMSE value was 0.0053 °C, and CVRMSE value was 0.04%). Detailed evaluation results from the case of BHE 1 using the separated evaluation dataset can be found in Fig. 3-13 and Fig. 3-14 below.

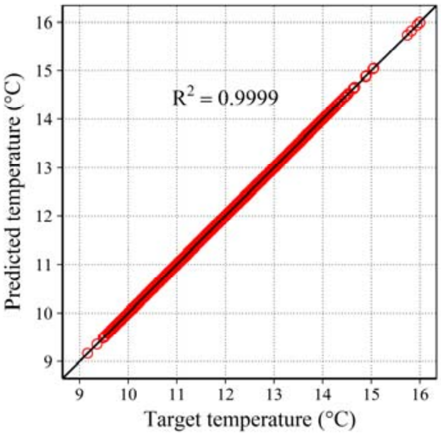

Fig. 3-13. Results of correlation analysis between predicted and target temperatures for selected ANN model (case BHE 1) with two hidden layers and thirty neurons each.

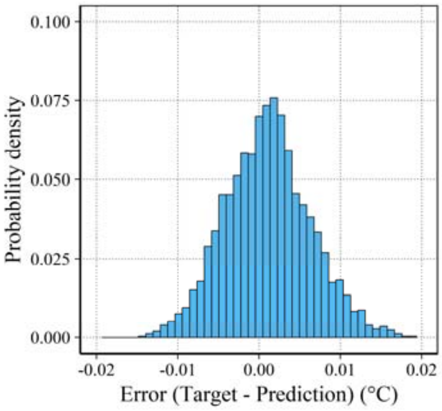

Fig. 3-14. Histogram of error between predicted and target temperatures for selected ANN model (case BHE 1) with two hidden layers and thirty neurons each.

3.5.3.2 Computational cost

The computational cost of the selected ANN model (case BHE 1 with two hidden layers and thirty neurons each) was examined. As shown in Fig. 3-15, the prediction speed with the numerical model and the ANN model were 261.82 s and 0.46 s, respectively. Thus, it was verified that the computational cost was hugely saved with using the ANN model instead of the numerical model.

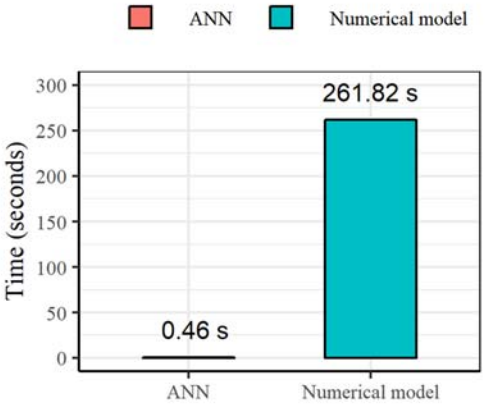

Fig. 3-15. Comparison of prediction speed between selected ANN and numerical model for BHE system.

3.6. Conclusion

In this study, ANN prediction models of the stratified chilled water TES system and the BHE for a GSHP system were constructed based on a case study to determine the appropriate combination of input parameters and training structures. This study could verify that a highly accurate ANN models with the significant savings in computational cost can be constructed by combining the valid input parameters and training structures. The primary results of the study can be summarized as follows:

- For the stratified chilled water TES system, the amount of heat remaining during the current and previous time steps (Q_{TES}^{t-1} and Q_{TES}^{t}) as well as information regarding temperature stratification during the previous time step ($T_1^{t-1}, T_2^{t-1}, \cdots, T_{19}^{t-1}$, and T_{20}^{t-1}) are valid as input parameters to predict the outlet temperature in charging and discharging operation (T_1^t and T_{20}^t).
- Regarding the BHE for the GSHP system, the outlet temperature during the two-steps-prior time step and that during the previous time step (T_{out}^{t-1} and T_{out}^{t-2}) as well as the rate of heat extraction during the current time step and that during the previous time step (q_{BHE}^t and q_{BHE}^{t-1}) must be included as the input parameters for ANN model training in order to predict the current outlet temperature (T_{out}^t).
- Furthermore, the constructed ANN model can be adequately utilized as a prediction model in the MPC scheme its computational cost can be remarkably reduced compared to the conventional physics-based or numerical model.

Chapter 4. Feasibility analysis of AI-based MPC based on simulation

Chapter 4.
Feasibility analysis of AI-based MPC based on simulation

Based on:

D. Lee, R. Ooka, S. Ikeda, W. Choi, Y. Kwak, Model predictive control of building energy systems with thermal energy storage in response to occupancy variations and time-variant electricity prices, Energy Build. 225 (2020) 110291. https://doi.org/10.1016/j.enbuild.2020.110291.

4.1. Introduction

Energy storage systems such as thermal energy storage (TES) systems that shift on-peak loads to off-peak hours are known to improve the effectiveness of HVAC operations [88]. It is well known that introducing a TES to the building energy systems has great potential to reduce the thermal peak load and increase cost savings compared to conventional chilled water systems [89]. However, it is important to develop effective operational strategies to maximize the utilization of the TES systems avoiding the mismatch the gap between the energy supply and building's end-user demand with dynamically varying occupancy schedules and electricity prices. In this respect, model predictive control (MPC) has received huge attention as an optimal control strategy for efficient building operations with TES [6].

MPC is a promising control strategy for HVAC systems with TES tank because it determines the optimal control input based on the predicted future behavior [36]. Because of its predictive nature, MPC is especially useful for operating on-site energy storage systems that have incorporated TES unlike the conventional control strategies such as on/off or proportional-integral-differential (PID) control [7]. According to the previous research, the operating cost of a building energy system with TES component could be reduced by adopting the MPC strategy by up to 8% [90] and 25–30% [91].

One of the advantages of the MPC strategy is that it considers future disturbances. The disturbances that affect the building energy management can be classified into three categories: climatic disturbances, occupant-behavior-related disturbances, and time-variant electricity pricing disturbances [14]. These three elements are key factors that need to be considered to manage to build facilities effectively. For this reason, various studies have been conducted to show how building energy systems can be controlled efficiently when considering these dynamic elements. For instance, it was confirmed that the control of HAVC system using a real-time occupancy recognition showed high savings in energy consumption in large public space [92]. Also, it was found that variations in occupancy status may cause additional energy consumption by 25%, and this is more influential compared to the measurement error of the outside temperature and solar irradiation [93].

MPC is promising way to avoid the mismatch the gap between the charged heat amount and the internal heat load that can affect optimal building operations with regard to TES systems more than with other HVAC systems [94]. In this respect, it is highly advantageous to account for dynamic information around these three elements when using MPC to optimize the operation of building facilities with a TES system. However, to date, research that examines the ability of MPC to manage unexpected operational disturbances for TES systems is insufficient.

Therefore, the purpose of this study is to examine the ability of MPC strategy to manage the unexpected operational disturbances for the operation of TES system. The Fig. 4-1 shows the flowchart of the present study in this chapter. Target building and its energy systems with the TES tank was assumed and modeled by the building simulation tool. To secure a practically applicable MPC controller, artificial intelligence tools were utilized to construct a prediction model and optimization solver. In this chapter, a case study was conducted to examine the MPC's ability to handle future disturbance scenarios subject to time-varying occupancy profiles and electricity prices. Optimal control results of the MPC strategy were evaluated by comparing it to a conventional rule-based control (RBC) strategy, which prioritized the operation of the TES.

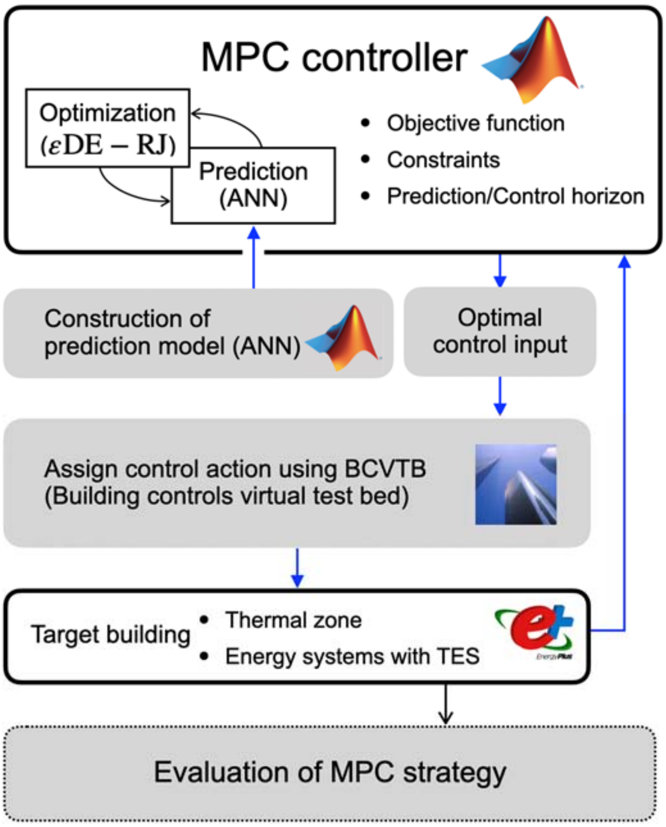

Fig. 4-1. Overall flowchart of the study to develop and evaluate AI-based MPC strategy based on the simulation analysis.

4.2. Description of building

A virtual building with a simple floor plan located in Tokyo was considered as a target building. A software of OpenStudio version 2.3.0 [95] and EnergyPlus version 8.5.0 [96] were utilized to modeling the virtual structure. The weather data used for the simulation were obtained from a Tokyo weather file that was created by referring to the expanded Automated Meteorological Data Acquisition System (AMeDAS) design weather data [97]. The cooling operation of the HVAC system was considered and the air-conditioning period for zone cooling was set from June 15 to September 15, during the weekdays.

The target building was an eight-story office building with a total floor area of 6,110.56 m^2 and the Fig. 4-2 shows the target building's overview and reference floor plan. As the figure shows, the office area was divided into two main spaces: the core space and the office space. The air-conditioning was conducted only in the office working area, and the thermal zone was modeled as a single lumped zone to simplify the analysis.

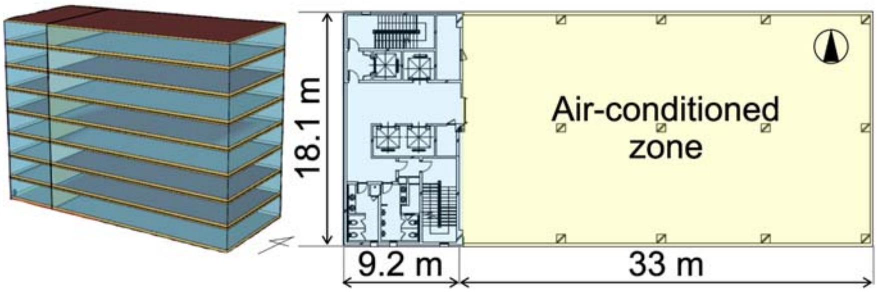

(a) Overview (b) Reference floor plan

Fig. 4-2. Target building.

The window-to-wall ratio was set at 80% and the design flow rate of the building infiltration was set at 0.0167 m^3/s. The material properties of the building envelop were set as follows: exterior wall = 0.95 $W/(m^2K)$; roof = 0.49 $W/(m^2K)$; floor = 0.71 $W/(m^2K)$; and window = 2.97 $W/(m^2K)$. The baseline for the internal heat load elements were considered referring from the previous studies which modeled the Japanese office buildings [98–100] and was set as follows: occupancy density = 0.35 $person/m^2$; metabolic heat gain from a person = 120 W/person; lighting = 10 W/m^2; and equipment = 15 W/m^2. The occupied office hours were set from 9 am to 6 pm and cooling operation was conducted from 8 am to 6 pm including one hour of pre-cooling with a single cooling setpoint temperature of 26 °C.

4.3. Description of system

The building energy systems including TES tank considered in this study are illustrated in the Fig. 4-3. The system consisted of four main components: air-source heat pump chiller (Chiller in Fig. 4-3) and one stratified chilled water thermal energy storage (TES) system for the primary side, as well as two fan coil units (FCU_1, FCU_2) for the secondary side. During the charging operation, the chiller sent chilled water to the TES tank and TES can manage the cooling load of the thermal zone during the discharging operation. When the TES was not available to manage the cooling load individually, the chiller began to operate in parallel.

As shown in Fig. 4-3, four water loops were connected by three counter-flow-type of fluid-to-fluid heat exchangers (HEX_1–HEX_3) and five variable-speed pumps ($Pump_1$–$Pump_5$). The control variables were the mass flow rates of Pump1–Pump5. Since the setpoint temperature of the chiller outlet was fixed at 4 °C, the output of the system could be managed by the variable mass flow rates. Also, the TES tank was assumed to have 10-layer temperature stratifications, and the fans attached to fan coil units were set to be controlled by a constant flow.

According to the pre-simulation results, the cooling peak load was confirmed as 229 kW. Therefore, the nominal capacity of the system components was fixed. The nominal capacity of FCU_1 and FCU_2 was set to 150 kW so that each fan coil unit could have a 30% safety margin to the half of the cooling peak load of 114.5 kW. The cooling capacity of the chiller was set to 390 kW to have a 30% margin to the sum of the nominal capacity of the two fan coil units. The volume of the TES tank was set to 170 m^3 to manage the daily cooling load of 762.8 kWh (40% of the maximum daily cumulative cooling load of 1,907 kWh).

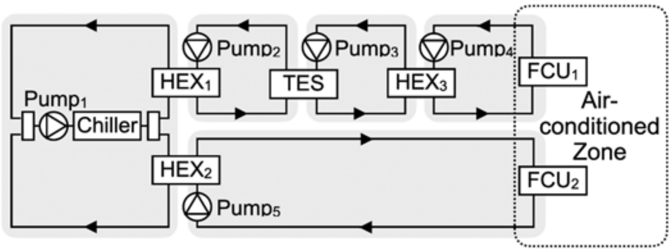

Fig. 4-3. Schematic of the target building energy system with TES.

4.4. Construction of ANNs

In the MPC strategy, an artificial neural network (ANN) was utilized as a surrogate model of the target thermal zone and its energy system. In the training of the network, a neural network toolbox from MATLAB software was utilized.

4.4.1. Training datasets

To prepare the appropriate training data, 64 datasets were obtained by combining the following simulation conditions: random occupancy density, four sets; constant occupancy density with 25% intervals, four sets; random mass flow rate of pumps, four sets; and constant mass flow rate of pumps with 25% intervals, four sets. Therefore, a total of 142,848 (93 d × 24 h × 64 datasets) hourly data were prepared. During the training process, the dataset was divided by three groups for the training (70%), validation to avoid excessive training (15%) and evaluation (15%) process based on the simple random method. The batch size was set at 1, and when the training was completed, the trained ANNs were estimated by the separated 15% of dataset with the results of the coefficients of determination (R^2), root mean square error (RMSE), and the coefficients of variation of the root mean square error (CVRMSE).

4.4.2. Input and target parameters

When using ANN models, a researcher's ability to select a suitable input and target data is crucial since there is any specific guidelines to determine the combination of input parameters. The input parameters are generally selected based on the researcher's experience and in accordance with the research subject and purpose. For instance, in a previous study, various parameters were tested and analyzed to increase the accuracy to predict the target data and the final combination of input parameters was determined through a sufficient trial-and-error [101]. This study constructed a four ANNs to predict the following parameters of the zone and system: room temperature, the temperature of the top and bottom layers inside the TES tank, inlet and outlet temperatures of the chiller, and the electricity consumption of the chiller. This study also conducted a sufficient trial-and-error approach to decide the best input parameter to obtain the high prediction accuracy and the selected input parameters are listed in the Table 4-1. The prediction of the room temperature was utilized in optimization solver to calculate the error between the cooling setpoint temperature.

Table 4-1. Selected input and target parameters of four constructed ANNs.

	Prediction subject	Input parameter	Target parameter
1	Air-conditioned zone	$T^t_{\text{out}}, S^t_{\text{diff}}, S^t_{\text{dir}}, N^t_{\text{occu}}, T^{t-1}_{\text{zone}},$ $\dot{m}^t_{\text{pump1}}, \dot{m}^t_{\text{pump2}}, \dot{m}^t_{\text{pump3}}, \dot{m}^t_{\text{pump4}}, \dot{m}^t_{\text{pump5}}$	T^t_{zone}
2	TES	$T^{t-1}_{\text{TES,top}}, T^{t-1}_{\text{TES,bot}}, T^t_{\text{zone}},$ $\dot{m}^t_{\text{pump1}}, \dot{m}^t_{\text{pump2}}, \dot{m}^t_{\text{pump3}}, \dot{m}^t_{\text{pump4}}, \dot{m}^t_{\text{pump5}}$	$T^t_{\text{TES,top}}, T^t_{\text{TES,bot}}$
3	Chiller	$T^t_{\text{out}}, RH^t, T^t_{\text{zone}}, T^{t-1}_{\text{c,in}}, T^{t-1}_{\text{c,out}}, T^t_{\text{TES,top}}, T^t_{\text{TES,bot}},$ $\dot{m}^t_{\text{pump1}}, \dot{m}^t_{\text{pump2}}, \dot{m}^t_{\text{pump3}}, \dot{m}^t_{\text{pump4}}, \dot{m}^t_{\text{pump5}}$	$T^t_{\text{c,in}}, T^t_{\text{c,out}}$
4		$T^t_{\text{out}}, RH^t, T^t_{\text{zone}}, T^t_{\text{TES,top}}, T^t_{\text{TES,bot}}, T^t_{\text{c,in}}, T^t_{\text{c,out}},$ $\dot{m}^t_{\text{pump1}}, \dot{m}^t_{\text{pump2}}, \dot{m}^t_{\text{pump3}}, \dot{m}^t_{\text{pump4}}, \dot{m}^t_{\text{pump5}}$	E^t_{chiler}

Fig. 4-4 shows the flowchart to search optimum control variables by the optimization solver based on the predicted parameters from the trained ANNs. In each ANN, the mass flow rate of the five variable-speed pumps ($\dot{m}_{\text{pump1}}$–$\dot{m}_{\text{pump5}}$) was included as input parameter therefore to capture the system behaviors according to the variations of decision variables. At the initial step, the mass flow rates of each pump were set as random values, and at the final step, the optimum mass flow rate of each pump can be found as the number of optimization calculation increased.

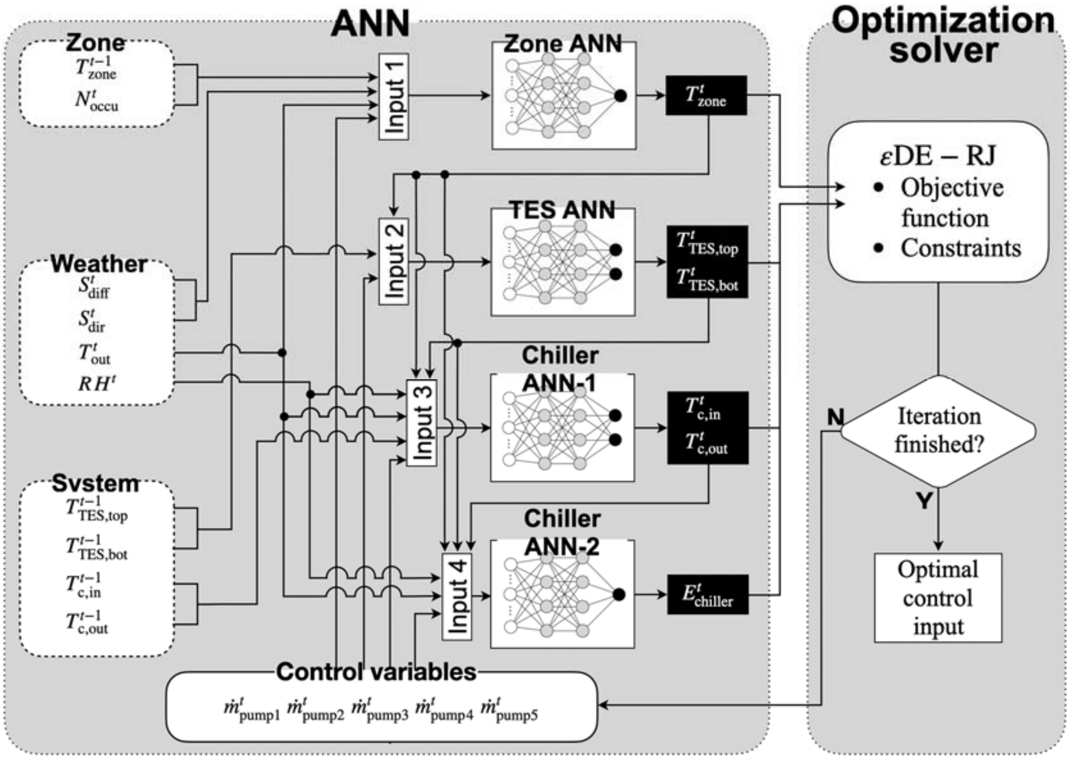

Fig. 4-4. Flowchart to search optimal control variables using ANNs and optimization solver.

4.4.3. Hyperparameters

A multilayer feed-forward-type neural network structure was adopted and the back-propagation algorithm was employed. The sigmoid function was used as an activation function for the hidden layers and as a linear function for the output layer. The Levenberg–Marquardt (LM) algorithm [84,85] was used as the training optimization algorithm. The entire training dataset was normalized in the range of [–1, 1] because the data preprocessing of normalization is known to improve the prediction performance of the neural network [86]. After the network was trained, the output parameters were back to the same units.

The number of hidden layers and their hidden neurons can be determined based on the complexity and nature of the problem at hand. Based on the trial-and-error approach, various combinations with different numbers of hidden layers and their neurons were confirmed. The evaluation results from the different number of hidden layers and neurons are illustrated in Fig. 4-5. In conclusion, a four-layer feed-forward type network composed of two hidden layers with thirty neurons was selected.

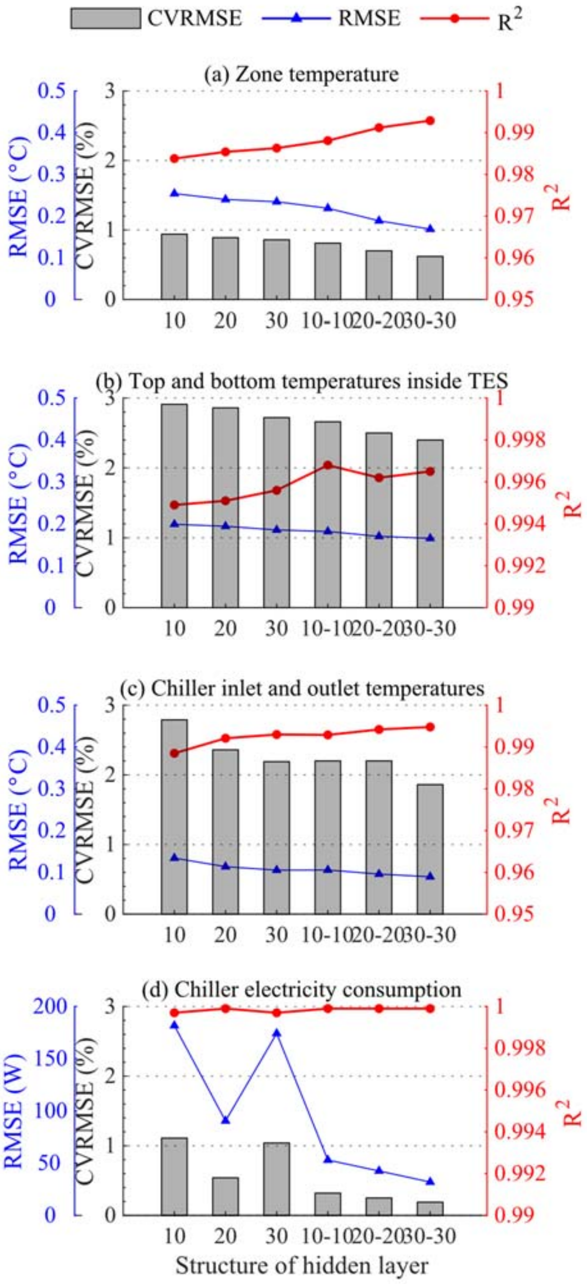

Fig. 4-5. Evaluation results of trained ANNs with different numbers of hidden layers and hidden neurons.

4.4.4. Model evaluation

The correlation analysis and the error histogram between the target and predicted data are described in Fig. 4-6 (a)–(d). The R^2 results of all ANNs showed a very high accuracy with over 0.9. Also, the RMSE were resulted as less than 0.167 °C for the temperature prediction of thermal zone and TES component. Moreover, the RMSE was results with a higher accuracy (0.0894 °C) for the temperature of the chiller component. Regarding the electricity consumption of the chiller component, the prediction accuracy was shown as high with the RMSE results of 0.031 kWh.

(a) ANN of room temperature prediction

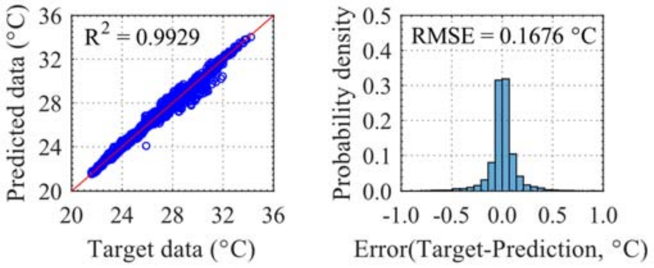

(b) ANN of TES temperature prediction

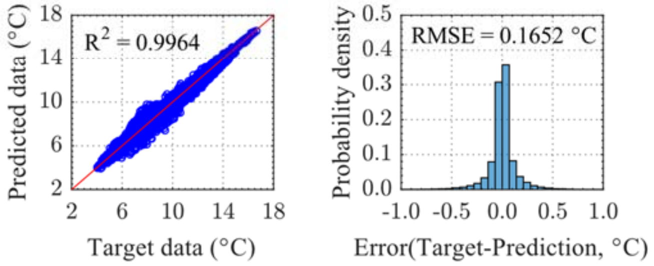

(c) ANN of chiller temperature prediction

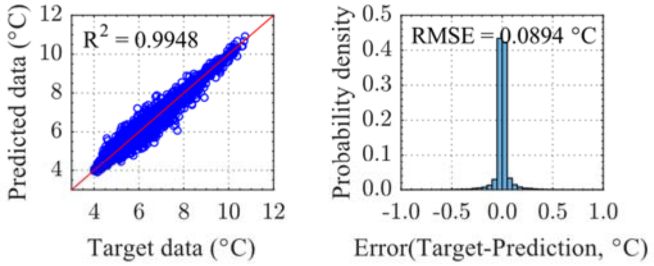

(d) ANN of chiller electricity consumption prediction

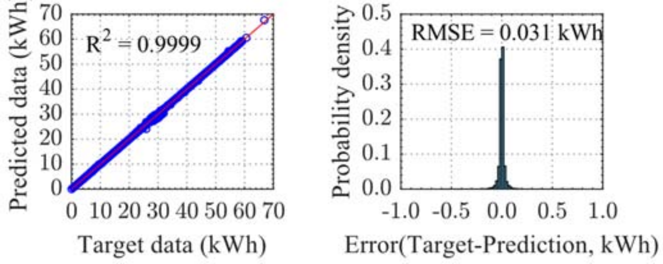

Fig. 4-6. Evaluation results of trained four-layer feed forward type (two hidden layers and 30 hidden neurons) ANNs.

4.5. MPC implementation

The MPC strategy was implemented for the target thermal zone and system using trained ANNs and optimization solver. The ANNs predicted the future states of the building and its energy system from ahead to the prediction time horizon and optimization solver searches optimal mass flow rates based on the predicted results at control time step intervals. The analysis was conducted based on the simulation for four weekdays where the outdoor temperature was shown as the highest. A third-party software, building controls virtual test bed (BCVTB) version 1.6.0 [102] in the Ptolemy II environment [103] was utilized for the flow rate control.

4.5.1. Schedule of disturbances

In this study, an unexpected variation in occupants internal loads and electricity prices were considered in MPC implementation. An unexpected variation was considered as operational disturbances in order to estimate the robustness of the MPC strategy. The two occupancy profiles are illustrated in the Fig. 4-7. The O_{baseline} refers to the baseline occupancy schedule assumed for the target building, and the $O_{\text{variation}}$ refers to a sudden unexpected increasement of occupants internal loads that can be captured only in the present time step. Therefore, a set of occupancy profiles ($O_{t+H_{\text{P}}|t}$) within the prediction horizon (H_{P}) at the present time step (t) was considered at every time step using Equation (4-1). In regards with the electricity prices, the time variant profile during the day was utilized as shown in Fig. 4-8.

$$O_{t+H_p|t} = \{O_{\text{variation}}^{t}, O_{\text{baseline}}^{t+1}, O_{\text{baseline}}^{t+2}, \cdots, O_{\text{baseline}}^{t+H_P}\} \tag{4-1}$$

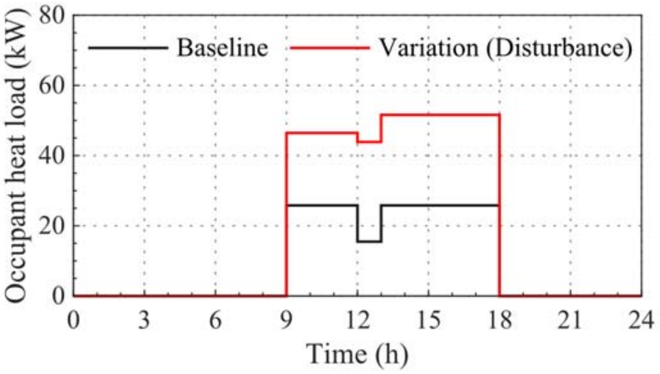

Fig. 4-7. Two profiles of occupant heat load considered as operational disturbances.

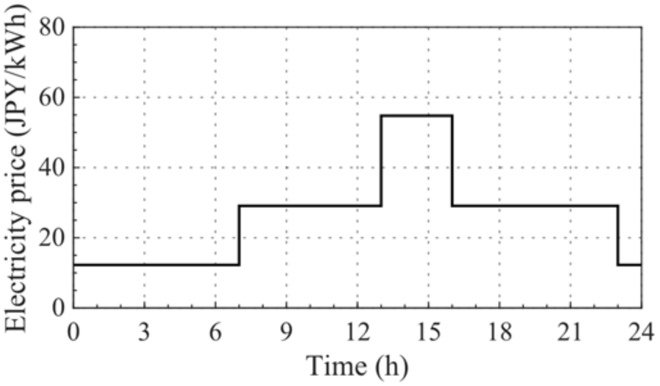

Fig. 4-8. Time-variant electricity prices.

4.5.2. Objective function and constraints

The objective function and constraints defined for the optimization calculation are described in Equations (4-2)–(4-15). The objective function (J_s) can be defined as a function of the mass flow rats for the primary side ($\dot{m}_{\text{pump1}}$–$\dot{m}_{\text{pump5}}$) because they were the decision variables to control the system as Equation (4-3). The optimization solver searches the optimal mass flow rates to minimize the total operating cost within the prediction horizon (H_P). Moreover, the zone temperature was constrained at 26°C of cooling setpoint temperature during occupied hours, and the mass flow rates for the primary side was restricted to be determined within their designed capacity. The air-conditioning was operated during the occupied hours including 1 hour of pre-cooling, i.e., 8 am to 6 pm, and the Pump$_2$ was constrained not to be operated ($\dot{m}_{\text{pump2}}$ $= 0$ (Equation (4-6)) since this pump was for the TES charging operation. During non-occupied hours, the system was operated for the TES discharging, therefore, the mass flow rates of Pump$_3$–Pump$_5$ ($\dot{m}_{\text{pump3}}$–$\dot{m}_{\text{pump5}}$) were set at 0 as expressed in Equations

(4-12)–(4-14). The system parameters that are necessary for the optimization calculation were predicted from the trained ANNs, however, the electricity consumption of pump (E_{pump}^{t}) was predicted by the linear regression equation expressed in Equation (4-15).

$$\text{Minimize } J_s = \sum_{i=t}^{t+H_P}\left\{\left(E_{\mathrm{chiller}}^{i} + \sum_{n=1}^{5} E_{\mathrm{pump}n}^{i}\right)\cdot P^{i}\right\} \tag{4-2}$$

$$J_s = f(\dot{m}_{\mathrm{pump1}}, \dot{m}_{\mathrm{pump2}}, \dot{m}_{\mathrm{pump3}}, \dot{m}_{\mathrm{pump4}}, \dot{m}_{\mathrm{pump5}}) \tag{4-3}$$

Subject to

$$T_{\mathrm{zone}} \leq 26\ °\mathrm{C} \text{ at 9 am to 6 pm} \tag{4-4}$$

If 8 am $\leq t <$ 6 pm

$$2.715\ \mathrm{kg/s} \leq \dot{m}_{\mathrm{pump1}} \leq 10.86\ \mathrm{kg/s} \tag{4-5}$$

$$\dot{m}_{\mathrm{pump2}} = 0 \tag{4-6}$$

$$2.055\ \mathrm{kg/s} \leq \dot{m}_{\mathrm{pump3}} \leq 8.22\ \mathrm{kg/s} \tag{4-7}$$

$$2.055\ \mathrm{kg/s} \leq \dot{m}_{\mathrm{pump4}} \leq 8.22\ \mathrm{kg/s} \tag{4-8}$$

$$2.055\ \mathrm{kg/s} \leq \dot{m}_{\mathrm{pump5}} \leq 8.22\ \mathrm{kg/s} \tag{4-9}$$

else

$$2.715\ \mathrm{kg/s} \leq \dot{m}_{\mathrm{pump1}} \leq 10.86\ \mathrm{kg/s} \tag{4-10}$$

$$2.715\ \mathrm{kg/s} \leq \dot{m}_{\mathrm{pump2}} \leq 10.86\ \mathrm{kg/s} \tag{4-11}$$

$$\dot{m}_{\mathrm{pump3}} = 0 \tag{4-12}$$

$$\dot{m}_{\mathrm{pump4}} = 0 \tag{4-13}$$

$$\dot{m}_{\mathrm{pump5}} = 0 \tag{4-14}$$

where

$$E_{\mathrm{pump}}^{t}\ (\mathrm{kWh}) = 0.2555 \cdot \dot{m}^{t}{}_{\mathrm{pump}} \tag{4-15}$$

4.5.3. Optimization solver (εDE-RJ)

One kind of metaheuristic optimization solver, εDE-RJ method was employed as an optimization solver. The εDE-RJ was proposed by Ikeda et al., which is combined optimization algorithm of the differential evolution (DE) algorithm, the epsilon (ε)-constrained method, and the random jumping (RJ) method. Originally, the DE was developed by Storn and Price [63]. The ε-constrained method was applied to the DE algorithm in order to handle the multiple constraints efficiently [65]. Also, the random jumping method was supplemented to prevent from getting stuck at a local minimum when the solution for a certain population in the later generations are the same. Details on the εDE-RJ algorithm and the comparative analysis to validate its algorithm beyond other conventional optimization solvers are described in [35].

The number of population and generations were set to 40 and 100, respectively. Therefore, 4,000 optimization calculations were proceeded at every control timesteps.

4.5.4. Case study

The results of the MPC implementation were compared with that of the conventional rule-based control (RBC). In RBC strategy, the system was controlled by the pre-defined schedules, and this study defined the operation rule as a TES priority operation. Therefore, the TES was charged by the constant mass flow rate of 10.86 kg/s during non-cooling operation hours and was discharged by the constant mass flow rate of 8.22 kg/s via HEX_3 during cooling operation hours. Since the capacity of the TES was designed as deficient to fully manage the thermal load, the chiller was parallelly operated during the cooling operation hours.

Four scenarios were compared in this study and the conditions of their operational strategy are summarized in Table 4-2. The Case 1 was operated by the RBC strategy when the building was occupied with basic occupancy profiles. The RBC strategy was also considered in Case 2 with the unexpectedly increased occupancy profiles was considered but mass flow rates for the primary side were controlled by the same values with the Case 1. The Case 2 was considered in order to investigate the influence of the occupancy increasement on the zone temperature regulation. The RBC strategy was normally applied in the Case 3, and the MPC strategy was implemented in Case 4, when the occupant heat load was suddenly increased.

Table 4-2. Summary of comparable operation scenarios.

Case	Disturbance	Control scheme	Description
	Occupancy		
Case 1	×	RBC	RBC considering no disturbances
Case 2	○	RBC	RBC considering disturbance but controlled by pump mass flow rates obtained from Case 1
Case 3	○	RBC	RBC considering disturbance
Case 4	○	MPC	MPC considering disturbance

4.6. Results and discussion

4.6.1. Prediction and control timestep

In the design of MPC controller, the prediction horizon of 24 h and the 1-h intervals of the control timestep are the most generally used in a numerous previous studies [14]. However, the design parameters of the prediction horizon and control timesteps can hugely affect the efficiency of the MPC controller. Thus, it is essential to elucidate the proper value of the prediction horizon and control timesteps prior to implementing the MPC. Therefore, different time horizons in the prediction (H_P = 48 h, 24 h, 12 h, 6 h, and 3 h) and control timestep (t = 60 min, and 30 min) were firstly examined. The control horizon (H_C) was set as the same as the value of the prediction horizon (H_P). The error in temperature regulation (T_err, °C (Mean ± SD)) between the MPC-controlled zone temperature ($T_\mathrm{zone,MPC}$) and cooling setpoint temperature (T_setpoint = 26 °C) in the different combinations of prediction horizon and control timesteps was estimated by Equation (4-16) and the results are illustrated in the Fig. 4-9.

$$T_\mathrm{err} = T_\mathrm{zone,MPC} - T_\mathrm{setpoint} \quad \text{(at 9 am to 6 pm)} \tag{4-16}$$

As a result, the control error was increased when the prediction horizon was shorter. With the 48 h of the prediction horizon, the control error was slightly increased, however the computation load was also significantly increased because multiple solutions are needed to be found with the enlarged solution space. When the prediction horizon was set at 24 h, the zone temperature was maintained with an error range (Mean ± SD) of 0.1 ± 0.2 °C with a control timestep of 60 min, and 0.2 ± 0.3 °C with a control timestep of 30 min, respectively. Therefore, the prediction horizon of 24 h and the control time step of 60 min was selected as the design parameters in MPC implementation.

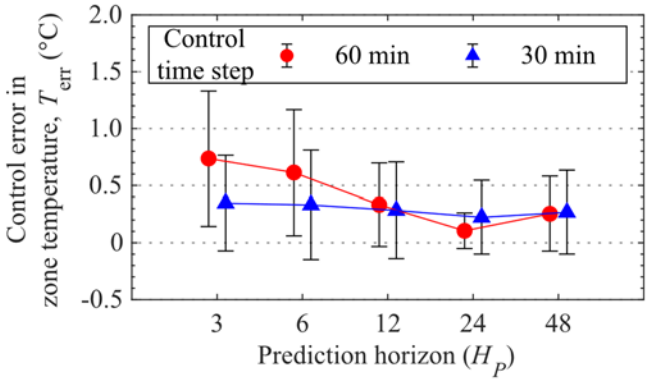

Fig. 4-9. Control error (Mean ± SD) between MPC controlled zone temperature and cooling setpoint over different prediction horizons and control timesteps.

4.6.2. Flow rate control

The results of flow rate control for Case 3 (RBC operation) and Case 4 (MPC operation) are shown in the Fig. 4-10. Because the RBC strategy was defined as a TES priority operation, in Case 3, the mass flow rates of pumps for TES charging and discharging operation were controlled at a constant level. On the other hand, in Case 4, the MPC predicted the system behavior looking ahead of 24 h at each 1 h interval and assigned the optimum mass flow rate by adequately controlling the charging and discharging amount in order to minimize the total operating costs.

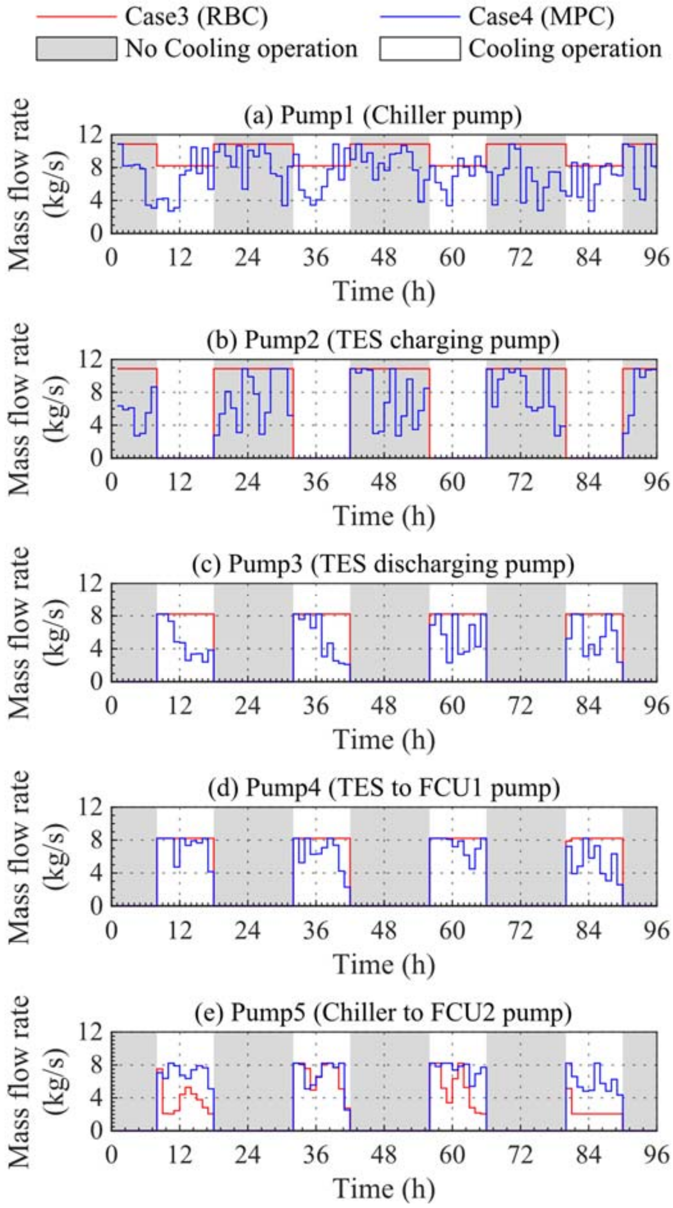

Fig. 4-10. Flow rate control results in RBC (Case 3) and MPC (Case 4).

4.6.3. ANNs performance

It is necessary to confirm the prediction accuracy compared to the actual measurement of the system when MPC was implemented since the model accuracy hugely affects the efficiency for finding the optimal control variables. Therefore, the predicted results from the ANNs were compared to the actual control output obtained from the model of target building on EnergyPlus in time series during the actual MPC operation phase.

As shown in the Fig. 4-11 (a), the zone temperature was well predicted by the ANN compared to the regulated zone temperature. During the non-cooling operation hours, the error between the predicted and actual zone temperature was larger. However, during the cooling operation hours, the predicted results were well-aligned with the actual zone temperature.

In regards with the prediction of temperatures inside the TES tank (top and bottom temperatures), the error ranged from 0.01 °C to 3.37 °C, and that of the bottom layer ranged from 0.008 °C to 0.09 °C, as shown in Fig. 4-11 (b) and Fig. 4-11 (c). Also, the temperature prediction for the chiller components were well forecasted, since the minimum and maximum errors resulted as 0.0006 °C and 2.35 °C for the inlet temperature, and 0 °C and 0.009 °C for the outlet temperature, respectively, as shown in Fig. 4-11 (d) and Fig. 4-11 (e). The prediction performance for the chiller electricity consumption showed also a high accuracy with the error range of 0.16 kWh to 13.32 kWh, as shown in Fig. 4-11 (f).

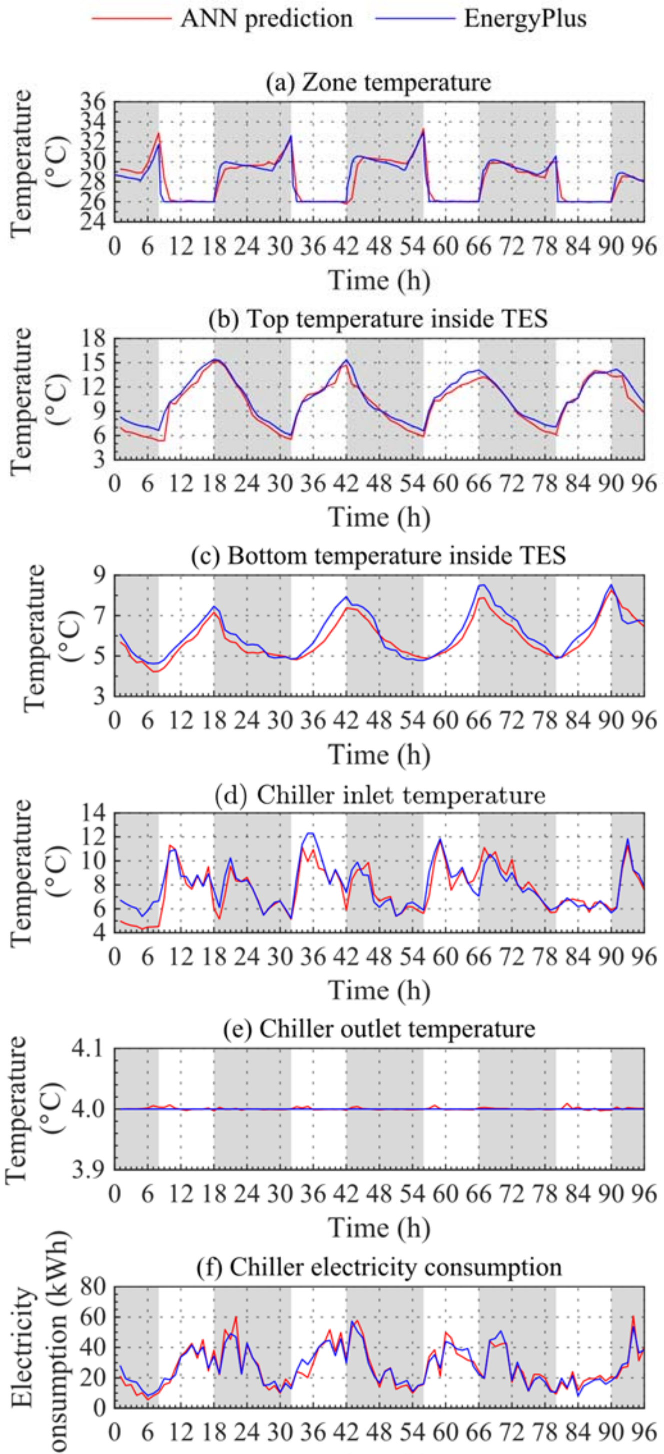

Fig. 4-11. Accuracy evaluation of trained ANNs during the MPC operation phase.

4.6.4. Zone temperature regulation

The results of zone temperature regulation in every case are illustrated in Fig. 4-12 (b)–(f). Also, the outdoor condition during the simulation period is described in the Fig. 4-12 (a). In the Fig. 4-12 (b), the results of zone temperature regulation are displayed where the Fig. 4-12 (c)–(f) shows enlarged results during the cooling operation hours. In Case 2, the zone temperature was not well controlled and exceeded the cooling setpoint temperature of 26 °C in cooling operated hours. This is because the supplying chilled water to the secondary side was not enough to manage the thermal load when the occupant heat load was suddenly increased. It can be inferred that it is necessary to manipulate the supplying flow rate by considering the operational disturbances. Except for the Case 2, the zone temperature was adequately regulated near the cooling setpoint temperature of 26 °C.

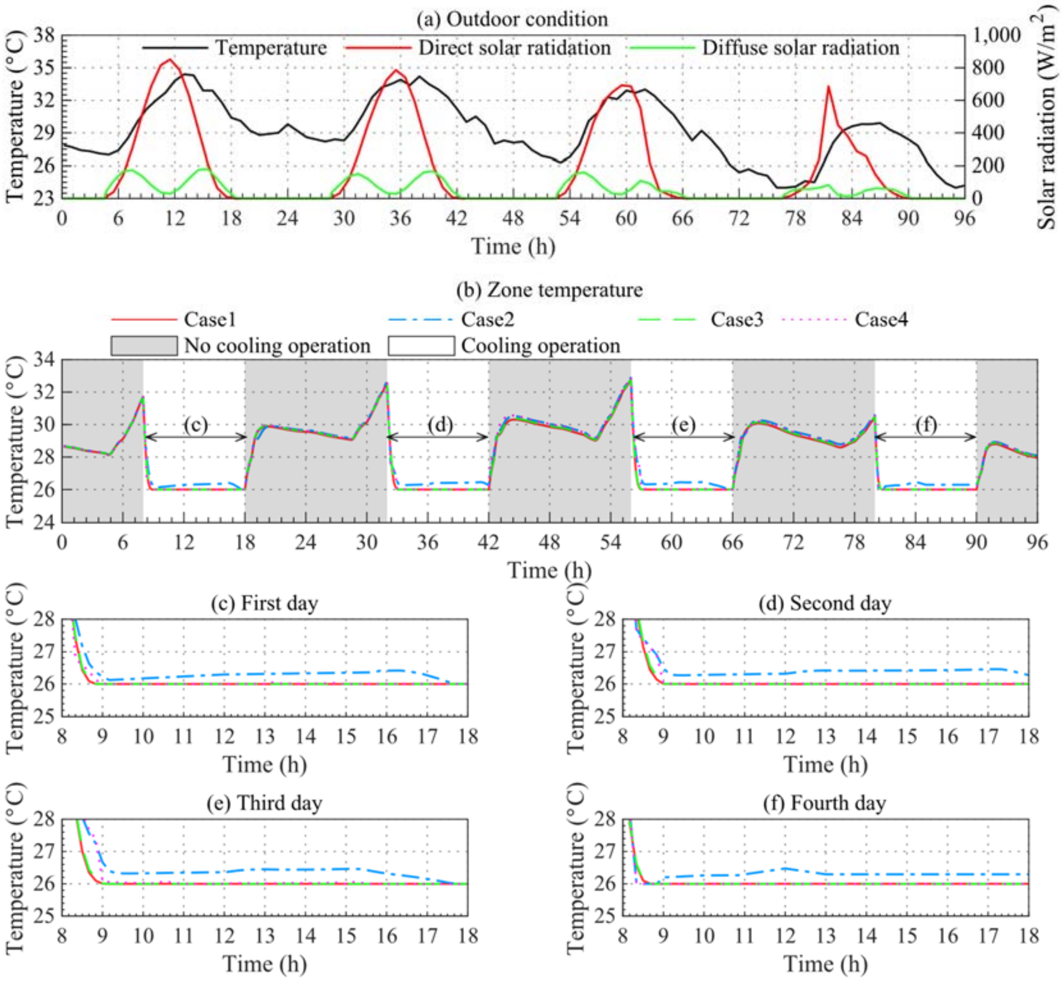

Fig. 4-12. Results of zone temperature regulation and outdoor conditions during the simulation period in each case.

4.6.5. Electricity consumption

The results of the electricity consumption of system's equipment in RBC case and MPC case were compared in the Fig. 4-13 (a) and Fig. 4-13 (b). As shown in the figures, the chiller took a large portion of the total energy used rather than pumps in the system. Thus, the operational strategy how well to control the chiller component is the key factor to reduce the total operating costs. When the system was manipulated by the RBC strategy, the operation rate of the chiller was overall lower during cooling operation hours because RBC took the priority in the TES operation. On the other hand, during the non-cooling operation hours, the chiller was much more operated for fully charging the TES tank.

However, when the system was operated by the MPC strategy, the operation rate of the chiller component was optimally assigned by the optimal mass flow rate. In a certain data points, the electricity consumption was greater in MPC strategy than the RBC strategy, but this is because the MPC determined the operation rate of the chiller considering to minimize the total cumulative operation cost, not just that of this moment.

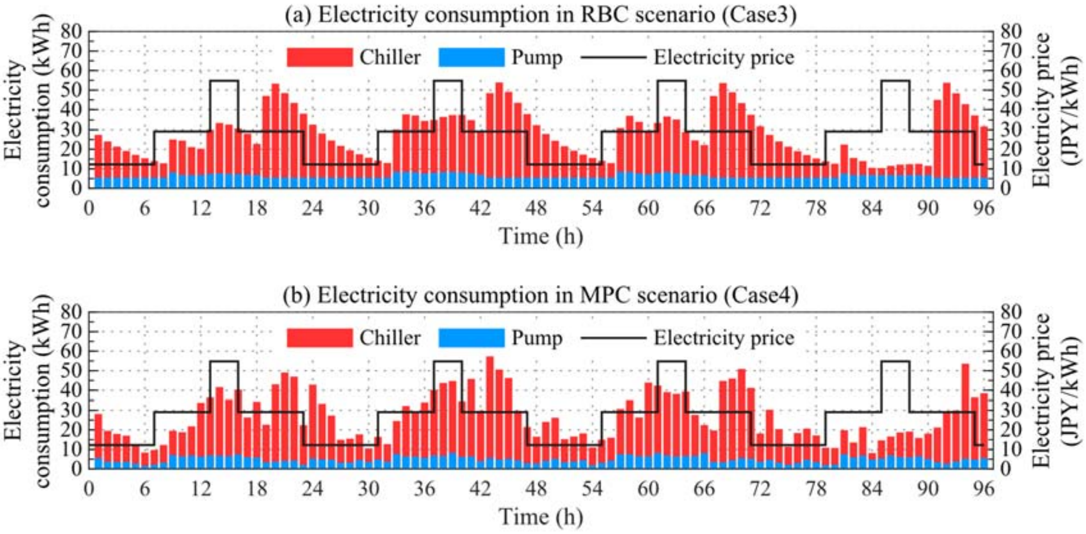
(a) Electricity consumption in RBC scenario (Case3)

(b) Electricity consumption in MPC scenario (Case4)

Fig. 4-13. Electricity consumption in RBC (Case 3) and MPC (Case 4) strategy.

4.6.6. Total operating costs

Total operation costs resulted in each case are compared in the Fig. 4-14. The cumulative operation cost in Case 2—that manipulated supplying flow rate same as the Case 1, but the occupant heat load was assumed as increased—were higher than those in Case 1 because the returning water temperature from the thermal zone was differed depending on the occupant heat load levels. Also, the operation cost from the Case 2 was shown as similar with the Case 3 since those two cases were manipulated by the RBC strategy and both cases considered the occupant heat load increasement. However, in Case 2, the zone temperature was not well regulated with the deficient supplying of the chiller water. In conclusion, the operation cost was saved by 1.5–7.2% by the MPC strategy—since Case 4 saved operation cost compared to the Case 3—depending on the outdoor conditions (see in Fig. 4-12 (a)).

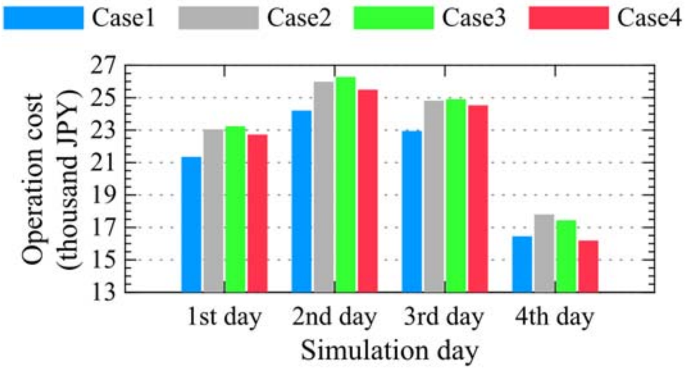

Fig. 4-14. Total operation cost in each case.

The cumulative cost savings in time series was compared between the RBC strategy (Case 3) and MPC strategy (Case 4) as shown in the Fig. 4-15. On the first day of the simulation period, the savings in operation cost was accumulated continuously during the non-cooling operation hours, however, it was started to be decreased during the cooling operation hours. This is because the MPC manipulated the chiller operation less than the RBC during the TES charging phase, therefore the chiller was necessary to operated more to handle the thermal load during the occupied hours. Despite this fact, total cumulative savings were recovered again during the nighttime and eventually the cumulative savings was accumulated day by day. Given this fact, the long-term application of the MPC strategy is worth to be examined in further studies.

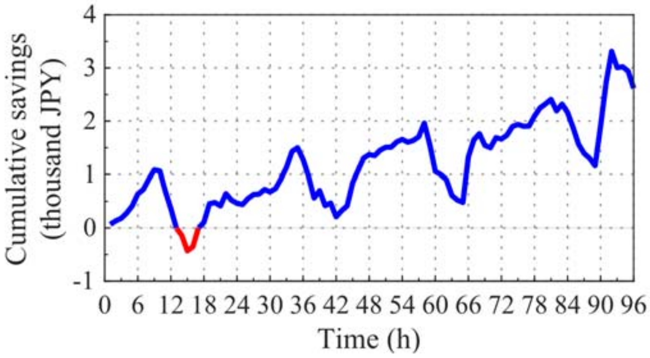

Fig. 4-15. Cumulative savings of operating costs in the MPC (Case 4) compared to the RBC (Case 3) strategy.

4.6.7. Computational cost

When the MPC strategy was implemented in the simulation analysis on a personal laptop (64-bit Windows 10, i7-8700 CPU (3.20 GHz), 8 GB RAM), the computational time to calculate the optimal flow rates took averagely 497 s as shown in the Fig. 4-16. The computational cost at the fist execution was approximately 600 s because the additional loading time was necessary. Given this fact, it can be inferred that the computation cost of the ε DE-RJ solver was sufficiently executable and its applicability for the MPC framework is high enough. Additionally, further details about the convergence speed of various metaheuristic optimization solvers can be referred from the previous study [104].

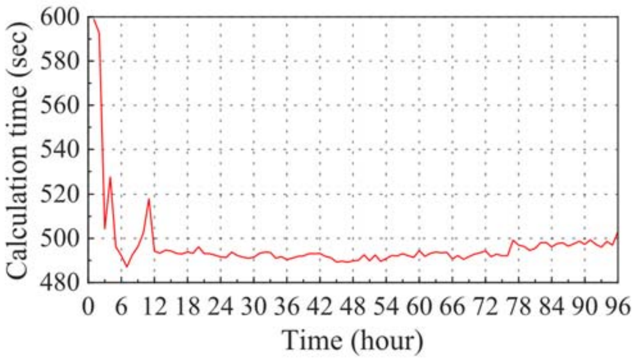

Fig. 4-16. Computational cost of εDE-RJ optimization solver (Calculation condition: the number of population was 40, the number of generation was 10, the prediction horizon was 24 h, and the control timestep was 1 h interval).

4.7. Conclusion

In this Chapter, the AI-based MPC strategy was established for the building energy systems equipped with the TES tank. An artificial neural network (ANN) was utilized to predict the future behavior of the building energy systems, and the epsilon constrained differential evolution with random jumping (εDE-RJ) was implemented as an optimization solver to minimize operating costs. The proposed AI-based MPC was examined based on the simulation analysis considering the sudden occupancy increasement as an operational disturbance. The results from the MPC operation were compared to the conventional rule-based control (RBC) strategy that prioritized the TES operation.

In conclusion, the MPC strategy could reduce the total operation cost of the system by 3.4% compared to the RBC strategy during the four-day of simulation period. However, the proposed AI-based MPC is still necessary to be validated via experimental implementation to analyze its feasibility to the real existing system.

Chapter 5. Experimental system to investigate AI-based MPC strategy

Chapter 5.
Experimental system to investigate AI-based MPC strategy

5.1. Introduction

In recent years, many researchers have dedicated their efforts to designing MPC strategies for the building sector to solve the low efficiency of building energy systems [105]. While numerous studies are striving to establish MPC strategy using machine learning for more efficient control of building energy systems, most of them are limited to simulation-based analysis. There are still few examples of real implementations introduced in actual building energy systems [11].

However, the experimental verification of MPC strategy using machine learning is necessary considering the following points. First, the historical data obtained from the simulation building model is quantitatively and qualitatively better than actual operational data since normally the real operation data incudes a huge noise and uncertainty in the measurement.

Furthermore, in the simulation-based analysis, the system physics occurred in the actual system such as mechanical characteristics of equipment when the operation starts and stops the driving, the heat loss that occurs when the heat is transferred from the primary side to the secondary side, and the time delay or the fluctuation of the zone temperature regulation that occurs when the heat is supplied from the primary side to the secondary side cannot be carefully considered. Finally, the MPC controller should be tested both in a software manner and a hardware manner, by linking the main MPC calculator and the system.

Therefore, the downscaled mock-up system was devised to validate the developed AI-based MPC strategy in Chapter 4. In this chapter, the detailed specifications of the experimental system, its different operation modes, and the configuration of the MPC controller was explained.

5.2. Experimental system

5.2.1. System description

To validate the developed AI-based MPC strategy in Chapter 4, the experimental system was constructed. The experimental system was installed in the Technical Research Laboratory of DAI-DAN Co. Ltd, located in Saitama, Japan as shown in the Fig. 5-1. The design and construction of this experimental system was conducted based on the industrial-educational cooperation with DAI-DAN Co. Ltd.

Fig. 5-1. Overview of the experimental system installed in Technical Research Laboratory located in DAI-DAN Co., Ltd, Saitama, Japan.

The schematic of the experimental system is illustrated in the Fig. 5-2. The system consisted of an air-source heat pump chiller (Chiller), thermal energy storage (TES), heat exchangers (HEX-1–HEX-3), variable speed pumps (P-1–P-5). Also, the overview of the installed equipment is illustrated in the Fig. 5-3.

The air-conditioning space was replaced by a water tank and the cooling demand was generated by an electric immersion heater installed inside the water tank (see Fig. 5-3 (d)). The cooling operation was investigated with this experimental system, and the control variables were the flow rates of P-1–P-4 for the primary side. The flow rate of P-5 for the secondary side was locally controlled by a PID controller to maintain the temperature of the water tank (TEW-12 in Fig. 5-2) at the cooling setpoint temperature.

The inlet and outlet temperatures between each equipment were measured, and the flow rates of each water loop were measured. The air temperature and the relative humidity of the outdoor near the air-source heat pump were installed, and the indoor air temperature around the place where the water tank was installed was measured. In addition, the power consumption of the chiller and pump components (P-1–P-5), and the electric immersion heater installed inside the water tank was measured.

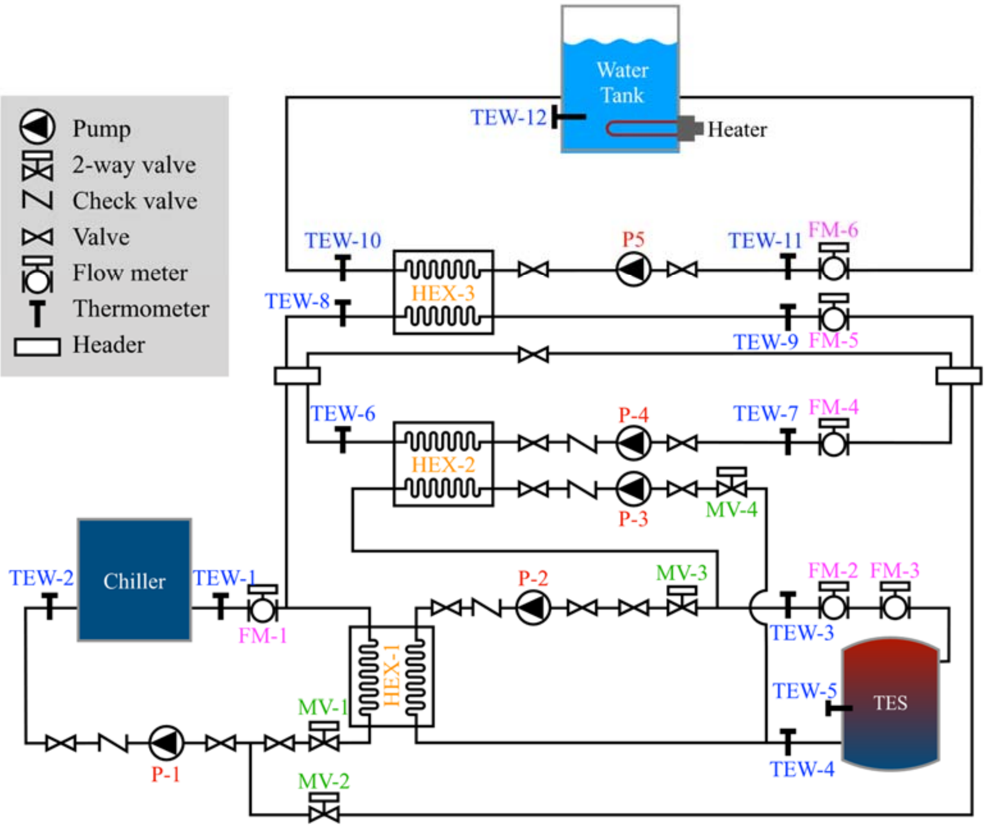

Fig. 5-2. Schematic of the experimental system.

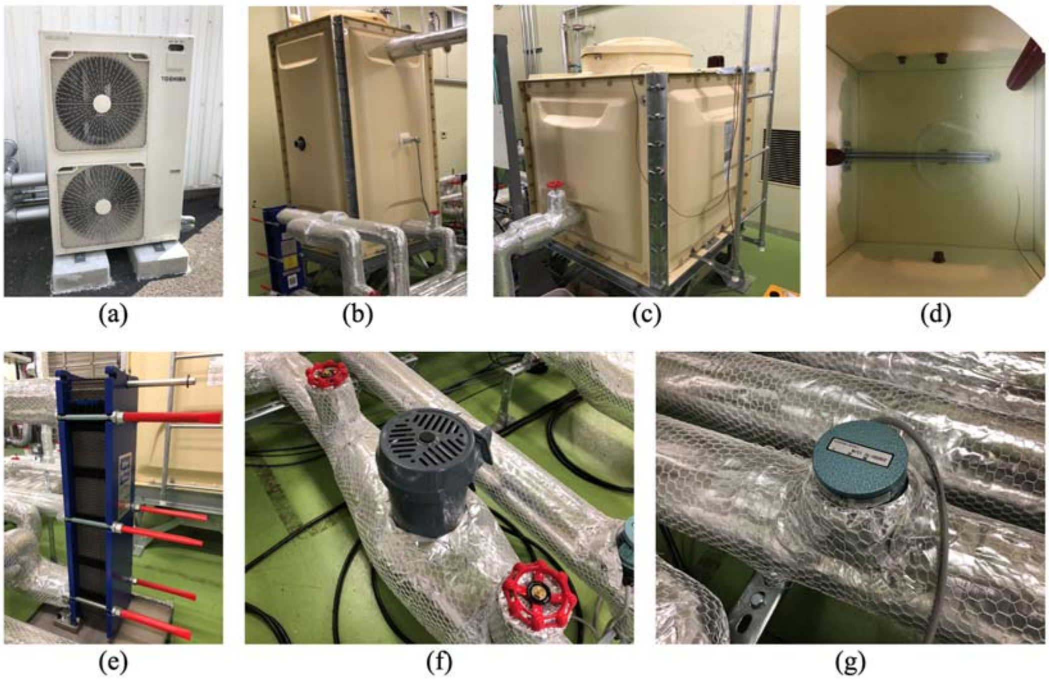

Fig. 5-3. Equipment of the experimental system: (a) air-source heat pump chiller, (b) thermal energy storage tank, (c) water tank to simulate the air-conditioning space, (d) electric immersion heater to assign a cooling demand installed inside the water tank, (e) heat exchanger, (f) variable speed pump, and (g) 2-way valve.

This experimental system is a scaled-down system designed under the assumption that the cooling peak load ($Q_{peakload}$) of 12 kW, therefore, the nominal cooling capacity of the main heat source, i.e., the air-source heat pump chiller ($Q_{chiller}$) was chosen to be 12.5 kW. With the assumption that the cooling peak load is 12 kW, the volume of the thermal energy storage tank was designed to manage the worst condition of the maximum daily cumulative cooling load ($Q_{max,dailyload}$) that the cooling peak load lasts for 9 hours during the air-conditioning hours. Therefore, the amount of heat storage required for the thermal energy storage tank (Q_{charge}) can be derived through Equation. (5-1) below.

$$Q_{charge} = 12\ \text{kW} \times \left(9\ \text{hours} \times \frac{1}{6} \times 3600\right) \text{seconds} \times 0.4 = 25{,}920\ \text{kJ} \qquad (5\text{-}1)$$

Based on the designed required amount of heat storage (Q_{charge}), the volume of the thermal energy storage tank (V_{TES}) can be derived based on the following Equation. (5-2).

$$V_{TES} = \frac{Q_{charge}}{\rho c_p \Delta T} = \frac{25{,}920}{1{,}000 \times 4.2 \times 5} = 1.23 \text{ m}^3 < 1.2 \text{ m}^3 \tag{5-2}$$

Where the ρ is the density of the flowing water assumed as 1,000 kg/m^3, the c_p is the specific heat of the flowing water assumed as 4.2 kJ/(kg K), the ΔT is the temperature difference in the usage of thermal energy storage tank assumed as 5 K, and the Q_{charge} is the required amount of heat storage for thermal energy storage assumed as 25,920 kJ derived from Equation. (5-1).

Moreover, the volume of the water tank to simulate the air-conditioning space was designed assuming the indoor space with a floor area of 240 m^2, with a ceiling height of 2.8 m. Therefore, the volume of the water tank (V_{tank}) was calculated based on the thermal capacity of assumed indoor space (C_{space}) with the volume of 672 m^3 as shown in Equation. (5-3) and Equation. (5-4).

$$C_{space} = \rho_a c_{p_a} V_{space} = 1.2 \times 1 \times 672 = 806.4 \text{ kJ/°C} \tag{5-3}$$

$$V_{tank} = \frac{C_{space}}{\rho c_p} = \frac{806.4}{1{,}000 \times 4.2} = 0.192 \text{ m}^3 < 0.2 \text{ m}^3 \tag{5-4}$$

Where the ρ_a is the density of the air assumed as 1.2 kg/m^3, the c_{p_a} is the specific heat of the air assumed as 1 kJ/(kg K), the V_{space} is the volume of the assumed indoor air-conditioning space set as 672 m^3, and the V_{tank} is the designed volume of the water tank to emulate the indoor air-conditioning space.

The temperature change rate ($R_{\Delta T}$) according to the volume of the water tank can be theoretically calculated by dividing the heat capacity of the water tank (C_{tank}) by the cooling peak load ($Q_{peakload}$) as expressed in the Equation (5-5). The Fig. 5-4 shows the results of temperature change rate according to the volume of the water tank when the 12 kW of the cooling peak load ($Q_{peakload}$) is generated by the electric immersion heater installed inside the water tank. When the volume of water tank (V_{tank}) was designed as 0.2 m^3 as shown in Equation. (5-4). Theoretically, it would take about 70 seconds to change the tank temperature by 1 °C.

$$R_{\Delta T} = \frac{C_{tank}}{Q_{peakload}} = \frac{\rho c_p V_{tank}}{Q_{peakload}} = \frac{1{,}000 \times 4.2 \times 0.2}{12} = 70 \text{ s/°C} \tag{5-5}$$

Where the ρ is the density of the flowing water assumed as 1,000 kg/m^3, the c_p is the specific heat of the flowing water assumed as 4.2 kJ/(kg K), the V_{tank} is the volume of the water tank designed as 0.2 m^3, and the $Q_{peakload}$ is the cooling peak load generated by electric immersion heater assumed as 12 kW.

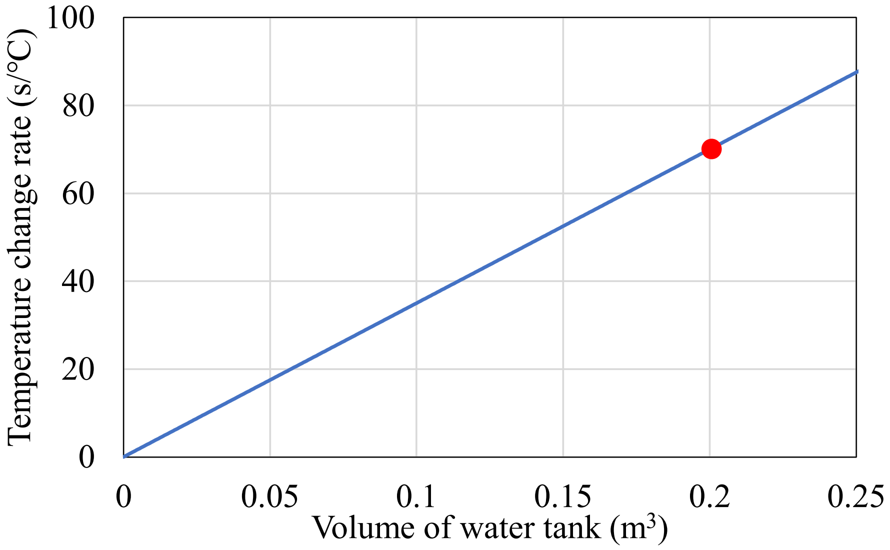

Fig. 5-4. Temperature change rate theoretically calculated according to the volume of the water tank when the heat generation by electric immersion heater is 12 kW.

The detailed specifications of each equipment in the experimental system are summarized in Table 5-1 below.

Table 5-1. Specifications of equipment in experimetal system.

Equipment/Component	Specification	
Air-source heat pump chiller (AHP)	Cooling capacity	12.5 kW
	Water flow rate	36.3 L/min
	Power consumption	4.03 kW
HEX-1, HEX-2	Heat exchanged	12.5 kW
	Pressure drop (hot side)	8 kPa
	Pressure drop (cold side)	8 kPa
HEX-3	Heat exchanged	12.5 kW
	Pressure drop (hot side)	14 kPa
	Pressure drop (cold side)	33 kPa
P-1, P-4	Water flow rate	36.3 L/min
	Total head	15 m
	Power consumption	0.4 kW
P-2, P-3	Water flow rate	36.3 L/min
	Total head	11 m
	Power consumption	0.25 kW
P-5	Water flow rate	18 L/min
	Total head	10 m
	Power consumption	0.15 kW
Electric immersion heater	Heat generation range	0–12 kW
Thermal energy storage (TES)	Effective volume	1.8 m^3
Water tank	Effective volume	0.2 m^3

5.2.2. Operation modes

Four operation modes are available in this experimental system: the TES charging operation, the cooling operation by the TES discharging, the cooling operation simultaneously by the TES discharging and the chiller operation, and the cooling operation by the chiller operation alone. The outlet temperature of the chiller for producing chilled water was set at 5 °C during the TES charging operation, and 7 °C for the cooling operation, respectively. Each operating mode can be implemented by controlling the on-off status of the equipment, the open-close status of 2-way valves based on the control table, and by assigning the analog input value (L/min scaled by the voltage value) to control the supplying flow rate in each water loop as described in Table 5-2.

Table 5-2. Control table for switching the operation modes of experimental system.

Equipment	Operation mode Mode 0	Mode 1	Mode 2	Mode 3	Mode 4
	Stop/Stand by	TES charging mode	Cooling mode (TES discharging)	Cooling mode (TES discharging + Chiller operation)	Cooling mode (Chiller operation)
Chiller	Off	On	Off	On	On
P1	Off	On	Off	On	On
P2	Off	On	Off	Off	Off
P3	Off	Off	On	On	Off
P4	Off	Off	On	On	Off
P5	Off	Off	On	On	On
MV1	Close	Open	Close	Open	Close
MV2	Close	Close	Close	Close	Open
MV3	Close	Open	Close	Close	Close
MV4	Close	Close	Open	Open	Close
Heater	Off	Off	On	On	On

5.2.2.1 Mode 1 (TES charging mode)

Fig. 5-5 shows a schematic diagram of the experimental system when the system is operated by operation mode 1. Operation mode 1 was considered for the TES charging operation where the chiller sends the chilled water to the heat storage tank to charge during the nighttime. This operation mode can be implemented by opening the 2-way valves of MV-1 and MV-3 and closing all other 2-way valves. During this TES charging operation mode, the chiller was set to send chilled water of 5 °C. The amount of supplying heat from the chiller to the TES tank can be adjusted by operating the pump of P-1 and P-2 by assigning the setpoint of the desired flow rate value and controlling the frequency of the inverter.

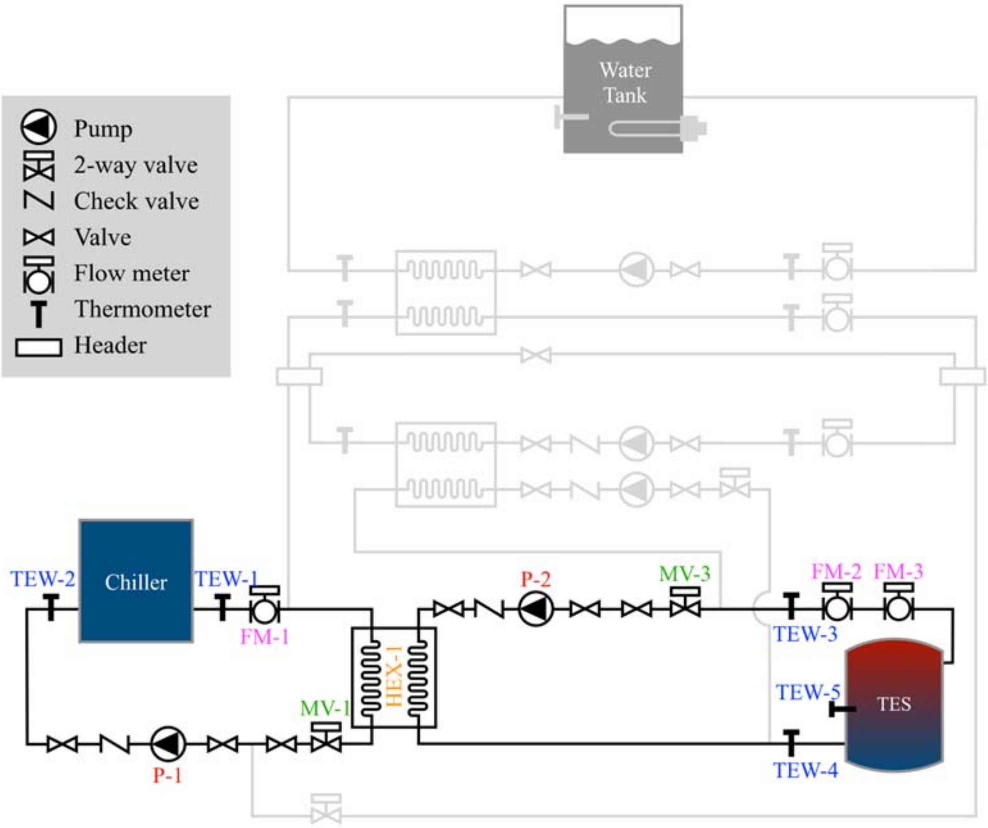

Fig. 5-5. Schematic diagram of experimental system in operation mode 1 (TES charging mode).

5.2.2.2 Mode 2 (Cooling mode with TES discharging operation)

When the system is operated to cool the secondary side by the TES discharging operation, the system diagram can be expressed as shown in the Fig. 5-6. The Mode 2 refers to the cooling mode by the TES discharging operation when the cooling demand is emerged by the heat generation from the electric immersion heater. This cooling mode with the TES discharging operation (Mode 2) can be implemented by opening the 2-way valve of MV-4 and closing all other 2-way valves. During this operation mode, the amount of supplying heat from the TES tank to the secondary side can be manipulated by assigning the flow rates of P-3 and P-4 and locally controlling the frequency of the inverters. The flow rate of P-5 for the secondary side was controlled by the local PID controller to maintain the water tank temperature of TEW-12 at the defined cooling setpoint temperature.

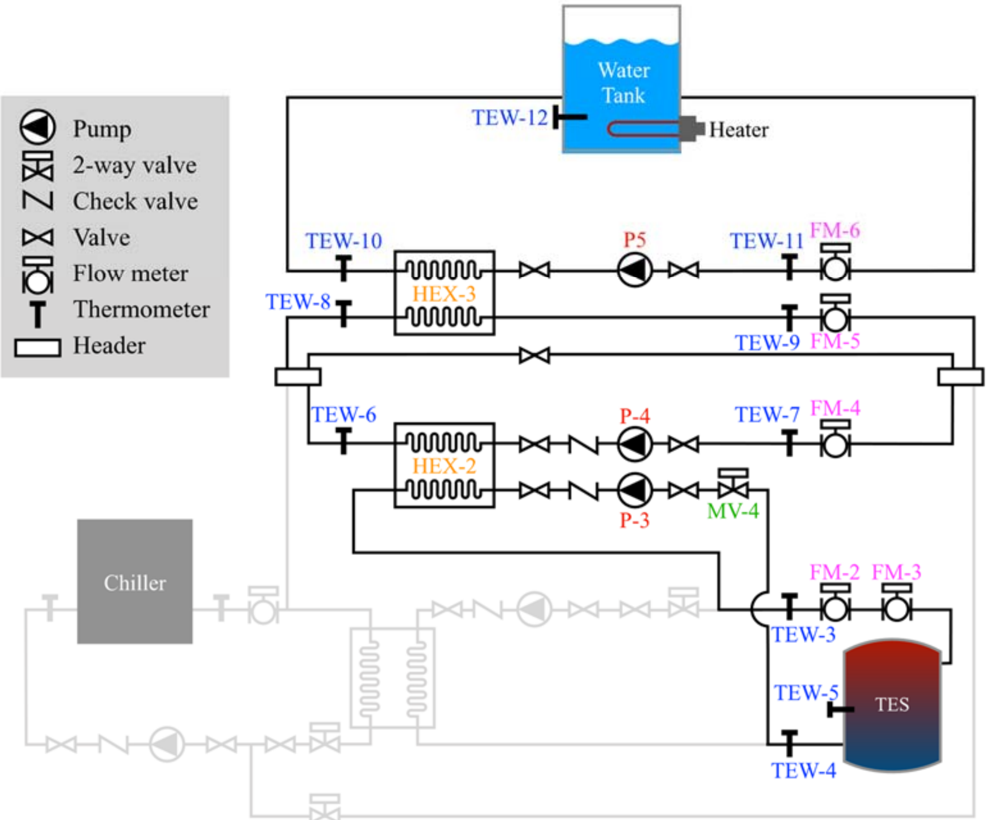

Fig. 5-6. Schematic diagram of experimental system in operation mode 2 (Cooling mode with TES discharging operation).

5.2.2.3 Mode 3 (Cooling mode with TES discharging and chiller operation)

Fig. 5-7 shows a schematic diagram of the experimental system when the system is operated by operation mode 3. The thermal load can be managed by the parallel operation of the TES discharging and the chiller. During the cooling operation, the chiller was set to send chilled water of 7 °C directly to the secondary side. The cooling operation through this parallel operation of this TES discharging and chiller (Mode 3) can be implemented by opening the 2-way valves of MV-2 and MV-4 and operating the pumps of P-1, P-3, and P-4. Each amount of supplying heat to the secondary side from the TES and from the chiller can be managed by the frequency control of each inverter.

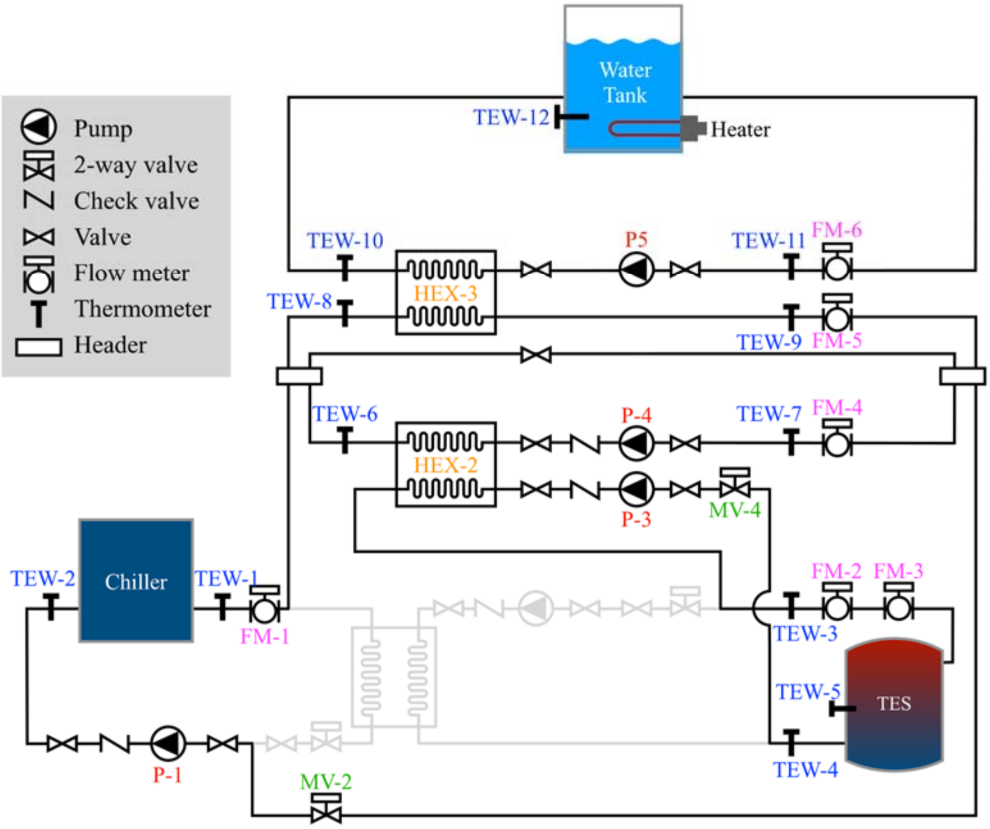

Fig. 5-7. Schematic diagram of experimental system in operation mode 3 (Cooling mode with TES discharging and chiller operation).

5.2.2.4 Mode 4 (Cooling mode with chiller operation)

Fig. 5-8 shows a schematic diagram of the experimental system when the system is operated by operation mode 4. When the charged heat amount of the TES tank is all used up, the chiller can solely manage the thermal load emerged in the secondary side. As same as the other cooling operation modes, the chiller directly sends the chilled water of 7 °C to the secondary side. The cooling mode by the chiller operation (Mode 4) can be implemented by opening the 2-way valve of MV-2 and operating the pump of P-1. Also, the amount of supplying heat from the chiller loop to the secondary loop can be managed by the frequency control of the inverter.

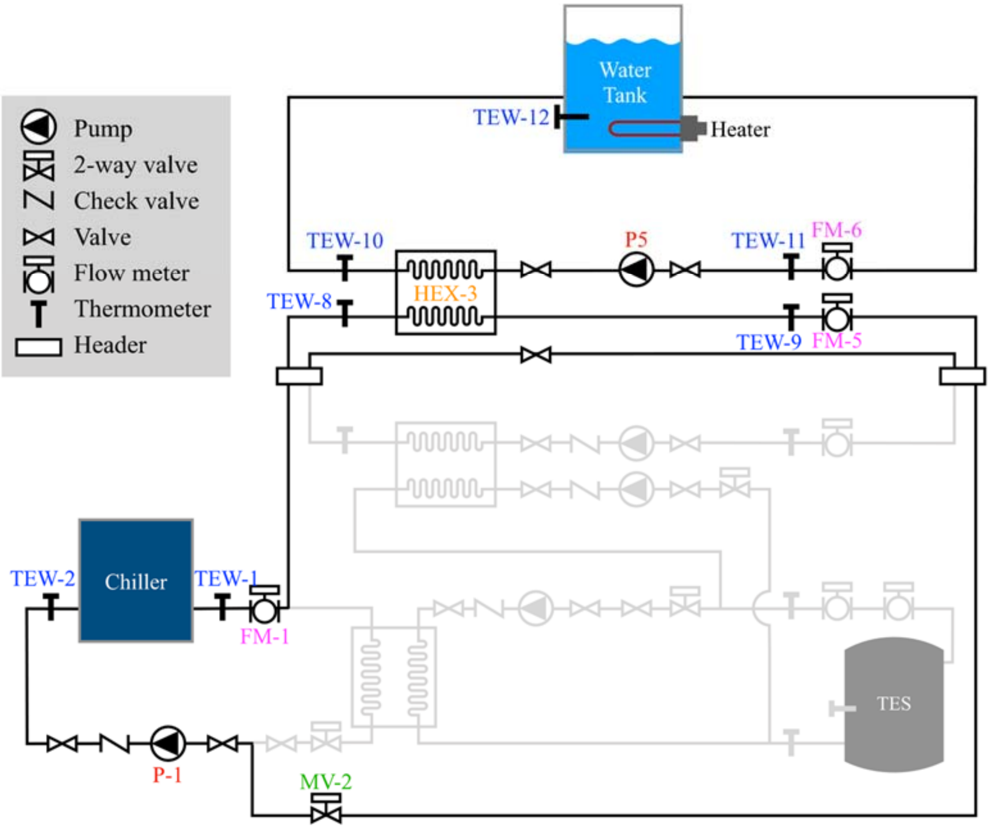

Fig. 5-8. Schematic diagram of experimental system in operation mode 3 (Cooling mode with chiller operation).

5.2.3. Data acquisition and control system

The configuration of the measurement and control for the data acquisition and control of the experimental system is described in the Fig. 5-9. Each equipment (i.e., air-source heat pump chiller, inverter, 2-way valve), and sensors to measure the air and water temperature, relative humidity, flow rate, and power consumption are wired into the control panel with analog signals. Then, the National Instrument's DAQ system [106] was wired to the control panel for receiving and sending a analog/digital signals to acquire the measured data and assign the control status for the system. The DAQ system was able to communicate with the main PC which contains the MATLAB via the software of LabVIEW. Therefore, the measured data can be saved in the main PC and the control input obtained from the MATLAB can be assigned via LabVIEW. The overview of the control panel wired with the DAQ system, and the main PC installed in the field can be found in Fig. 5-10.

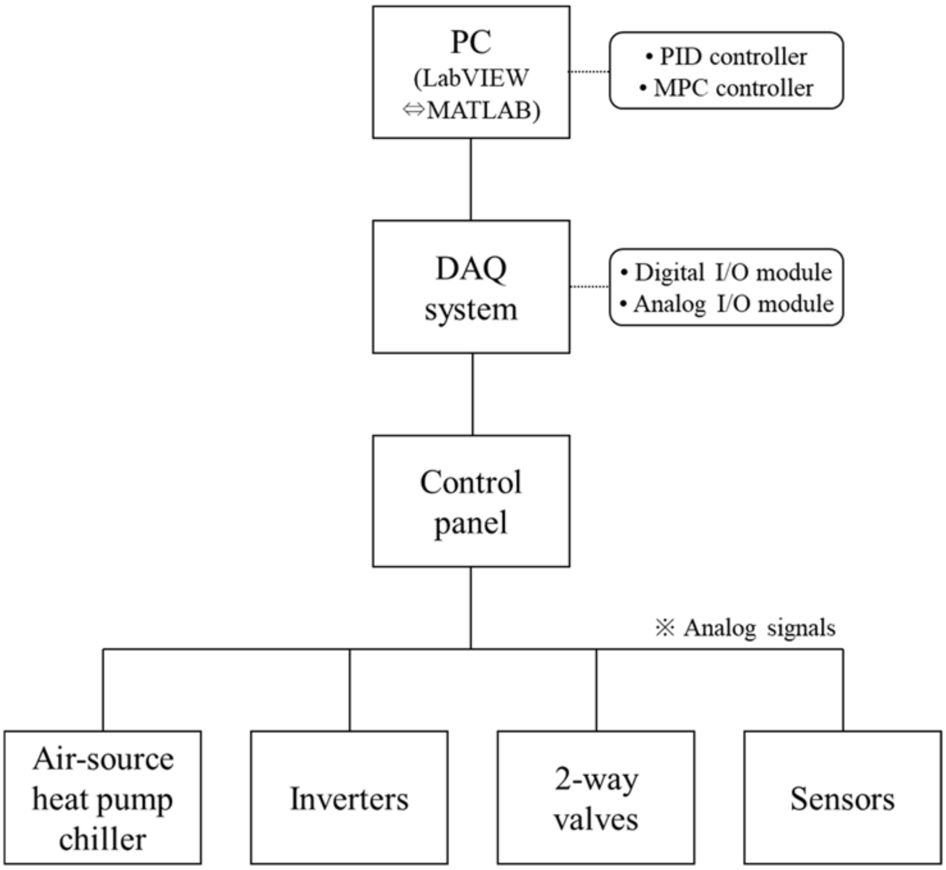

Fig. 5-9. Configuration of the measurement and control system for acquiring the measured data and assigning the control signals for the experimental system.

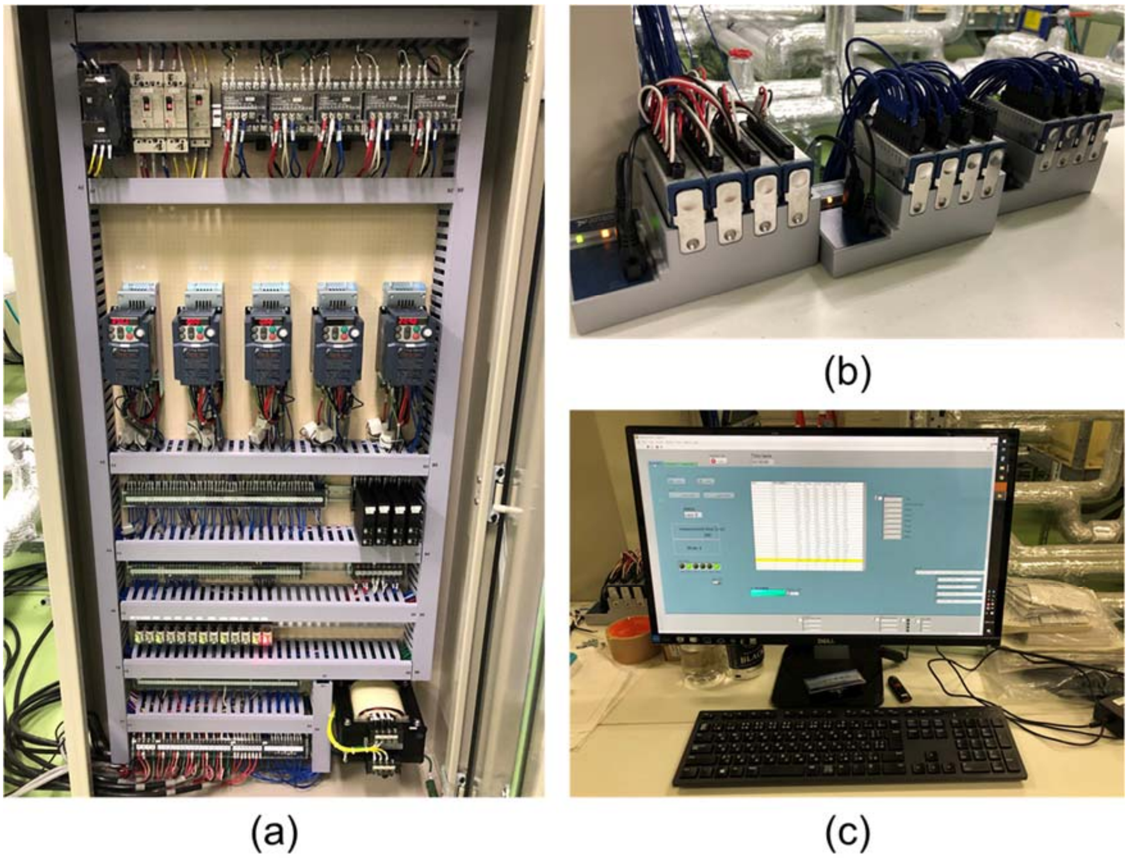

Fig. 5-10. Overview of the data acquisition and control system installed in the field: (a) Control panel, (b) National Instrument's DAQ system consists of analog I/O and digital I/O module, (c) LabVIEW environment in main PC controller.

In this study, the control variables are the flow rates of pumps (P-1–P-4) on the primary side of the experimental system. Therefore, the measurement of the flow rate in each water loop and the control of the inverter's frequency is necessary to be configured. A detailed flow chart to measure and control the pump flow rate is illustrated in Fig. 5-11. The flow rate meter in each water loop is wired into the isolator, and the analog signal from the sensor is sent both to the inverter and DAQ system via the control panel, respectively. The inverter receives the target flow rate determined from the main PC controller, and at the same time, controls the frequency of the inverter with the internal PID controller based on the feedbacked measured flow rate.

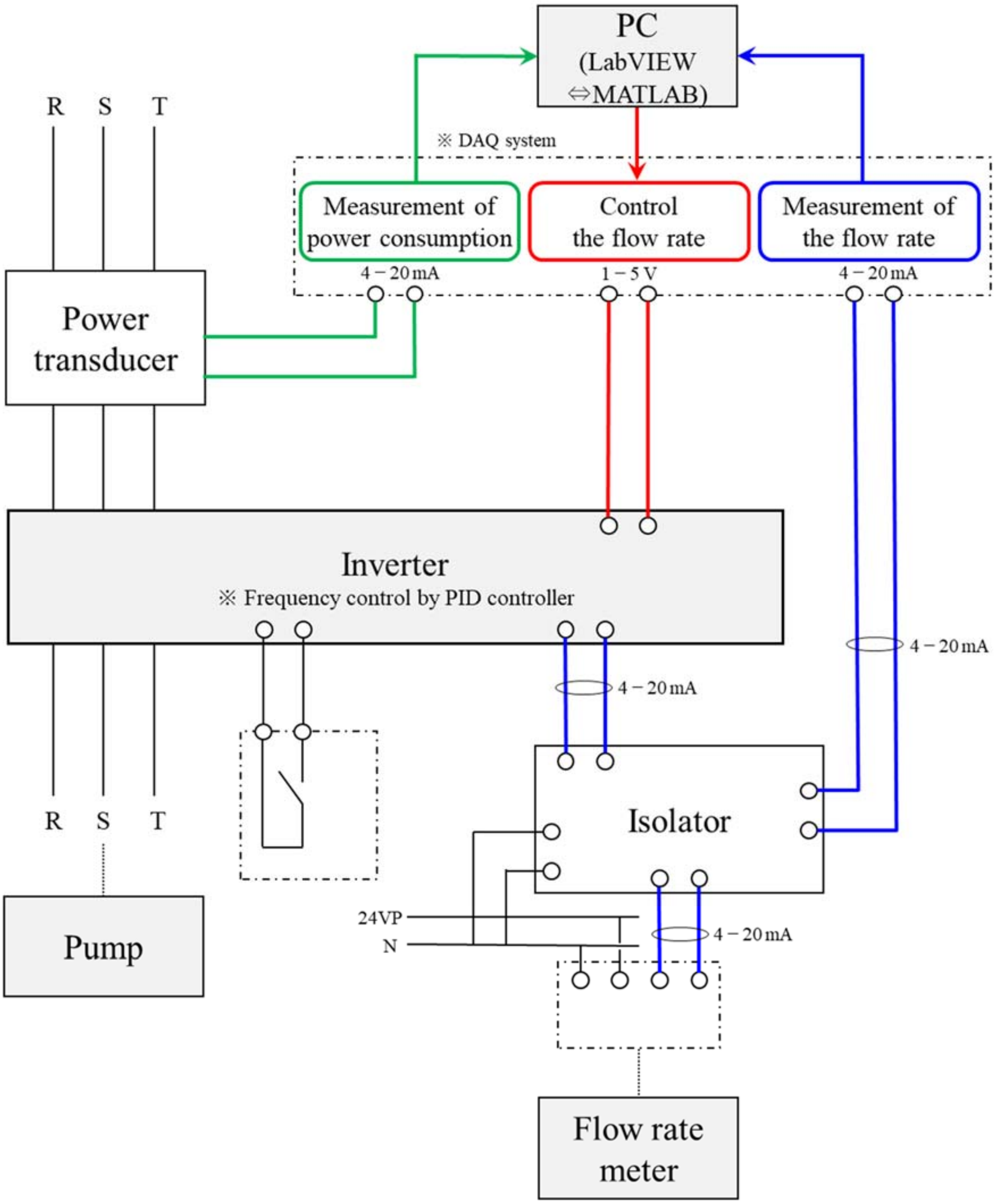

Fig. 5-11. Schematic diagram of measurement of the flow rate in each water loop and control of the inverter frequency by the main PC controller.

5.2.3.1 Control of RBC strategy

To experimentally validate the developed AI-based MPC strategy, the conventional rule-based control (RBC) strategy was also operated. This study defined the RBC strategy to prioritize the TES operation based on PID controllers. The TES was charged during the non-cooling operation hours at a nominal flow rate of 36.3 L/min to fully charge the TES tank and lower the mean tank temperature to 6 °C. The discharging operation was conducted until the charged heat amount in the storage tank is ran out i.e., the mean tank temperature increased to 11 °C.

In the TES discharging operation, the flow rate of P-3 and P-4 were manipulated by the PID controllers to send the chilled water at 7 °C to the secondary side and to maintain the water tank temperature at 26 °C, respectively. The setting condition of the PID controllers, i.e., the target setpoint values (setpoint, SP), measured values to feedback (process value, PV), and manipulated values (manipulated value, MV) can be found in the Table 5-3. Each PID controller was programmed by National Instrument's LabVIEW software [106] as shown in Fig. 5-12 and Appendix 6, Appendix 7, Appendix 18, and Appendix 19.

Generally, the heat source equipment in the primary side is controlled to supply the chilled water in a certain stable temperature. However, it was difficult to maintain the supplying chilled water temperature in a stable manner thus the control problem was considered to directly regulate the water tank temperature.

Table 5-3. Conditions of PID controllers used in RBC strategy.

Operation mode		PV	SP	MV
Cooling operation	TES discharging operation (Mode 2)	TEW-6	7 °C	Flow rate of P-3
		TEW-12	26 °C	Flow rate of P-4
	Chiller operation (Mode 4)	TEW-12	26 °C	Flow rate of P-1

*Note that TEW-6 is the temperature of supplying water from TES tank to the secondary side during TES discharging operation, and TEW-12 is the water tank temperature (see Fig. 5-2)

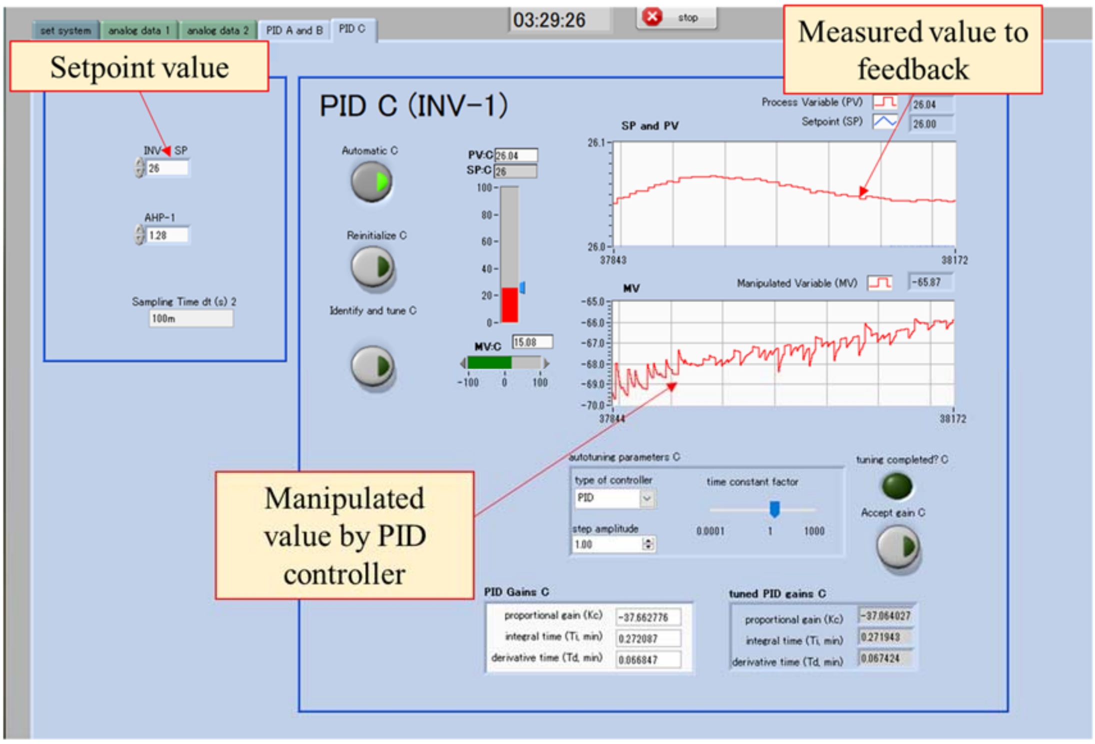

Setpoint value

Measured value to feedback

Manipulated value by PID controller

INV-1 SP: 26

AHP-1: 1.28

Sampling Time dt (s) 2: 100m

PV:C 26.04

SP:C 26

MV:C 15.08

Process Variable (PV): 26.04

Setpoint (SP): 26.00

Manipulated Variable (MV): −65.87

autotuning parameters C

type of controller: PID

step amplitude: 1.00

time constant factor: 1

PID Gains C

proportional gain (Kc)	-37.662776
integral time (Ti, min)	0.272087
derivative time (Td, min)	0.066847

tuned PID gains C

proportional gain (Kc)	-37.064027
integral time (Ti, min)	0.271943
derivative time (Td, min)	0.067424

Fig. 5-12. Control panel of PID controller programmed in LabVIEW environment used in RBC strategy.

5.2.3.2 Control of MPC strategy

As stated in the earlier section, four operating modes are available to be switched in the experimental system: the TES charging operation (Mode 1), the cooling operation by TES discharging operation (Mode 2), the cooling operation by TES discharging and chiller operation simultaneously (Mode 3), and the cooling operation only by the chiller operation (Mode 4).

Unlike the RBC strategy which operates the system according to the pre-defined rule i.e., TES priority operation, in the MPC strategy, the operation mode can be determined differently at every control timestep according to the result from the optimization solver. Therefore, it is necessary to establish the logic for an automatic control of the system based on the optimal solution given by the MPC controller.

A flowchart of control logic described in the Fig. 5-13 was applied to freely switch the operation modes by the optimization results at the current timestep. When the solution for flow rates of pumps on the primary side was decided by the optimization solver, the operation mode was identified and automatically switched based on this logic.

Also, when switching the operation mode, the control signals were given in the order of (1) open/close of 2-way valves, (2) on-off status and flow rate control of pumps, and (3) on-off status of the chiller at the start of the operation, and (1) on-off status of the chiller, (2) on-off status and flow rate control of pumps, and (3) open/close of 2-way valves at the end of operation for the safe operation of the experimental system.

The AI-based MPC algorithm was constructed using MATLAB R2020b, receiving the measurement results, and assigning optimal control inputs to the system by linking with the national instrument's data acquisition (DAQ) system and LabVIEW [106]. The control panel of the MPC controller programmed in the LabVIEW environment are shown in Fig. 5-14 and can also found in Appendix 4 and Appendix 12.

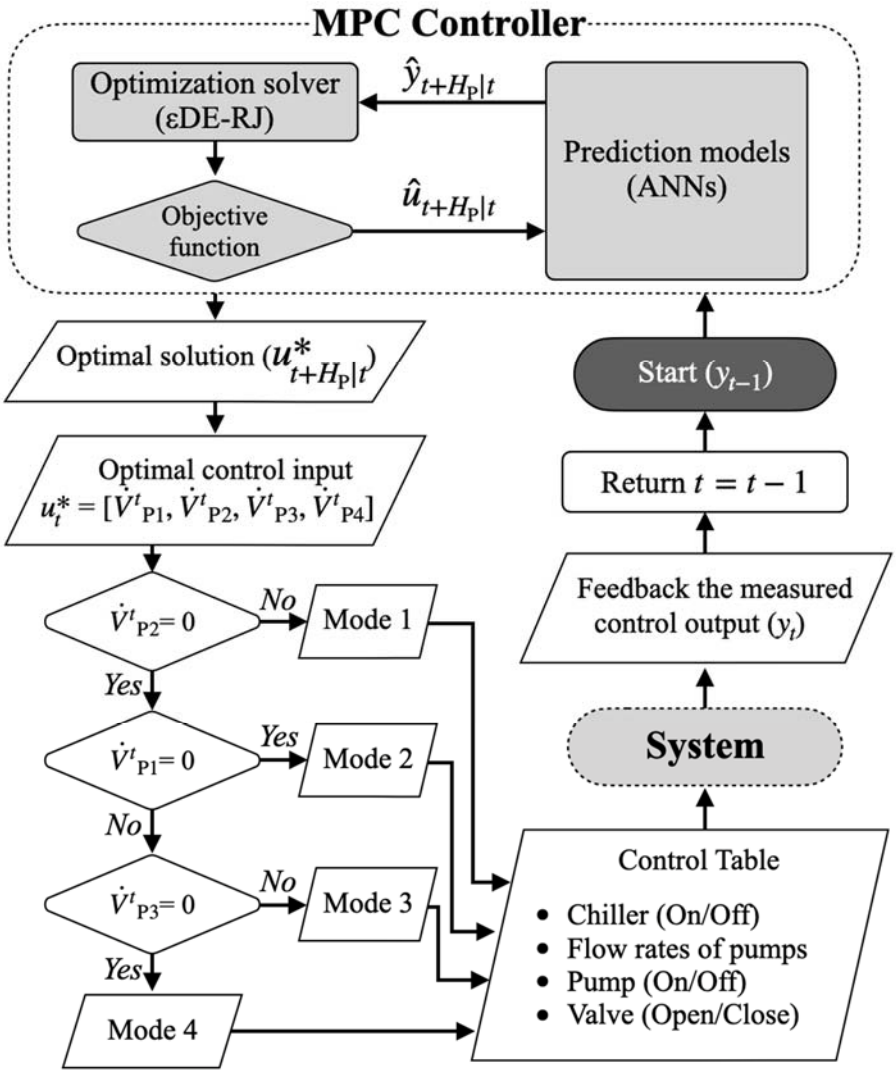

Fig. 5-13. Flowchart of AI-based MPC implementation by identifying the operation mode based on the optimization results.

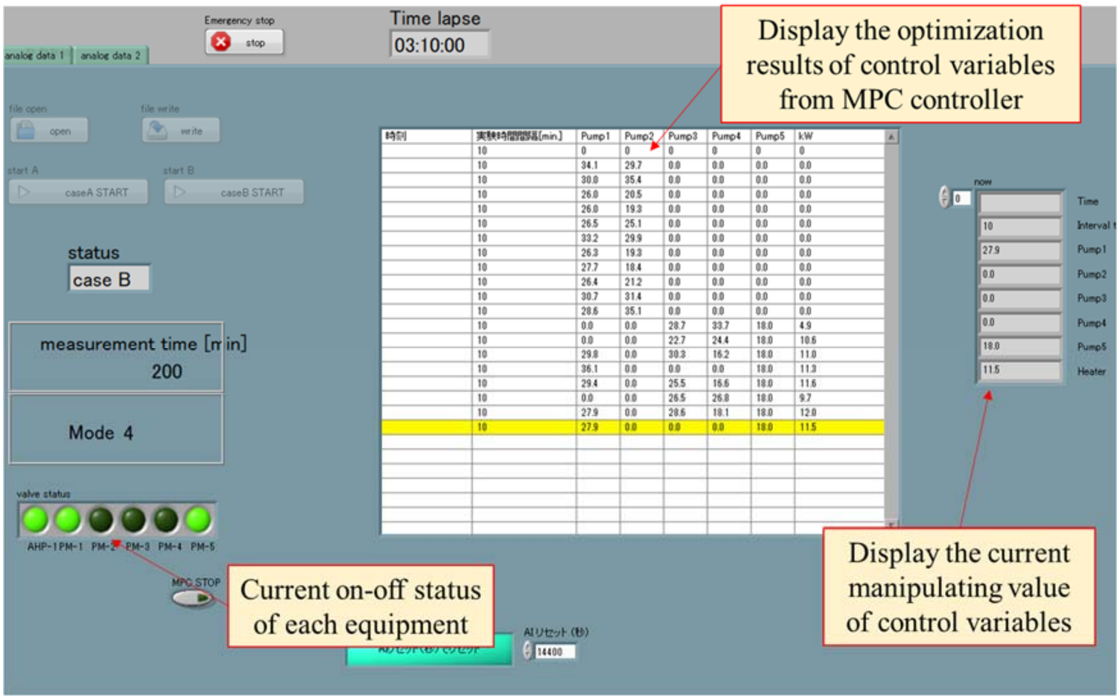

Time lapse 03:10:00

status case B

measurement time [min] 200

Mode 4

AIリセット (秒) 14400

Display the optimization results of control variables from MPC controller

時刻	実験時間間隔[min.]	Pump1	Pump2	Pump3	Pump4	Pump5	kW
	10	0	0	0	0	0	0
	10	34.1	29.7	0.0	0.0	0.0	0.0
	10	30.0	35.4	0.0	0.0	0.0	0.0
	10	26.0	20.5	0.0	0.0	0.0	0.0
	10	26.0	19.3	0.0	0.0	0.0	0.0
	10	26.5	25.1	0.0	0.0	0.0	0.0
	10	33.2	29.9	0.0	0.0	0.0	0.0
	10	26.3	19.3	0.0	0.0	0.0	0.0
	10	27.7	18.4	0.0	0.0	0.0	0.0
	10	26.4	21.2	0.0	0.0	0.0	0.0
	10	30.7	31.4	0.0	0.0	0.0	0.0
	10	28.6	35.1	0.0	0.0	0.0	0.0
	10	0.0	0.0	28.7	33.7	18.0	4.9
	10	0.0	0.0	22.7	24.4	18.0	10.6
	10	29.8	0.0	30.3	16.2	18.0	11.0
	10	36.1	0.0	0.0	0.0	18.0	11.3
	10	29.4	0.0	25.5	16.6	18.0	11.6
	10	0.0	0.0	26.5	26.8	18.0	9.7
	10	27.9	0.0	28.6	18.1	18.0	12.0
	10	27.9	0.0	0.0	0.0	18.0	11.5

Time:
Interval t: 10
Pump1: 27.9
Pump2: 0.0
Pump3: 0.0
Pump4: 0.0
Pump5: 18.0
Heater: 11.5

Display the current manipulating value of control variables

Current on-off status of each equipment

Fig. 5-14. Control panel of MPC controller programmed used in LabVIEW environment.

Chapter 6. Experimental analysis of AI-based MPC under different cooling load conditions

Chapter 6.
Experimental analysis of AI-based MPC under different cooling load conditions

6.1. Experimental condition

An accelerated experiment that shortens the day from 24 hours to 4 hours was conducted. One of the strong advantages of the accelerated experiment is that we can operate the system plenty more within the limited period. Also, the behavior of the system during different operation mode can be captured within a short time duration. However, the accelerated experiment has drawbacks that the long-term behavior of the system cannot be observed and further the real time scale of the appropriate prediction horizon and control timestep cannot be examined.

The experiment was started from the TES charging operation assuming the starting point of unoccupied hours at night. As stated in Chapter 5, the air-conditioning space was simulated by the water tank and the cooling demand was be given by an electric immersion heater installed inside the water tank. Considering the maximum output of the heat generation of the electric heater is 12 kW, three representative patterns of cooling load schedules where the thermal load continues as high, medium, and low level during the day were tested. Detailed three cooling load profiles are described in the Fig. 6-1. When the cooling demand is emerged, the operation mode of the system is switched from the TES charging operation to a cooling operation.

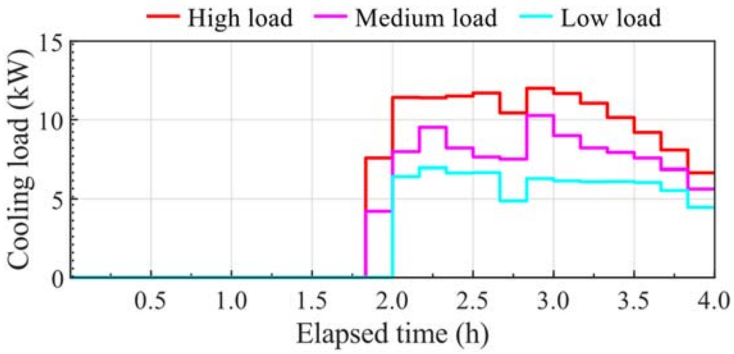

Fig. 6-1. Three representative cooling load schedules assumed and tested in the experiment.

The RBC strategy that prioritize the TES priority operation was also collected from the experimental system to be compared with the MPC strategy. The case of RBC commences the TES discharging operation as soon as the cooling mode commences. Also, the TES was charged during the non-cooling operation hours at a nominal flow rate of 36.3 L/min to lower the mean tank temperature to 6 °C. The discharging operation was conducted until the mean tank temperature increased to 11 °C. The flow rate of the pump for the TES discharging operation (P-3 and P-4) was manipulated by the PID controllers to send the chilled water at 7 °C to the secondary side, and maintain the tank temperature at 26 °C detailed conditions for PID controllers in RBC strategy can be found in Table 5-3. The results from the RBC case were compared with those of the MPC strategy in each three different cooling loads schedules. In the MPC strategy, a plan of electricity price is assumed as shown in Fig. 6-2. The cooling demand and electricity prices, which this study assumed to be known in advance.

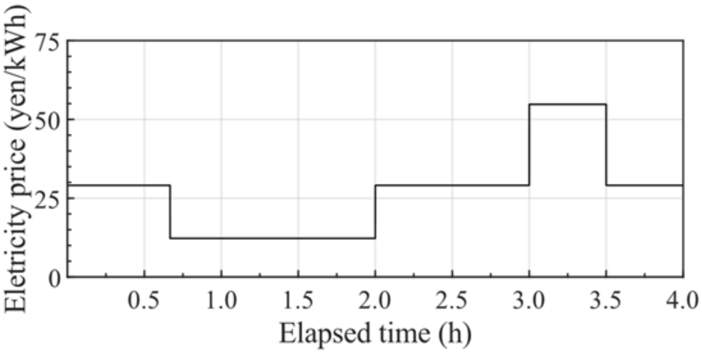

Fig. 6-2. Time-variant electricity prices assumed in the experiment.

6.2. Implementation of MPC strategy

6.2.1. ANN prediction models

Five ANN models with different prediction targets were constructed. The prediction targets are the water tank temperature, TES tank temperatures (top, middle, and bottom layers), chiller inlet/outlet temperatures, and power consumption of the chiller and the pumps. Equations. (6-1)–(6-5) show the input parameters required to predict each prediction target. The input parameters were selected empirically, considering the influence between the prediction targets. The flow rates of pumps on the primary side are included as input parameters in every ANN because the behavior of the prediction target can be captured by varying the control variables. Especially, in the prediction of the water tank temperature, the input parameter of the outlet and indoor temperature was considered since the water tank is installed inside the room therefore the tank temperature varied depending on the outdoor and indoor temperature condition.

$$\hat{y}(T^{t}_{tank}) = ANN\left(T^{t-1}_{out}, T^{t-1}_{env}, E^{t}_{heater}, T^{t-1}_{tank}, \dot{V}^{t-1}_{P5}, \dot{V}^{t}_{P}\right) \tag{6-1}$$

$$\hat{y}(T^{t}_{TES}) = ANN\left(T^{t-1}_{env}, T^{t}_{tank}, T^{t-1}_{TES}, \dot{V}^{t}_{P}\right) \tag{6-2}$$

$$\hat{y}(T^{t}_{chiller}) = ANN\left(T^{t}_{out}, T^{t}_{tank}, T^{t}_{TES}, T^{t-1}_{chiller}, \dot{V}^{t}_{P}\right) \tag{6-3}$$

$$\hat{y}(E^{t}_{chiller}) = ANN\left(T^{t}_{out}, T^{t}_{tank}, T^{t}_{TES}, T^{t}_{chiller}, \dot{V}^{t}_{P}\right) \tag{6-4}$$

$$\hat{y}(E^{t}_{P}) = ANN\left(\dot{V}^{t}_{P}\right) \tag{6-5}$$

where

$$T_{TES} = \left[T_{TES,top}, T_{TES,mid}, T_{TES,bot}\right] \tag{6-6}$$

$$T_{chiller} = \left[T_{chiller,in}, T_{chiller,out}\right] \tag{6-7}$$

$$E_{P} = \left[E_{P1}, E_{P2}, E_{P3}, E_{P4}\right] \tag{6-8}$$

$$\dot{V}_{P} = \left[\dot{V}_{P1}, \dot{V}_{P2}, \dot{V}_{P3}, \dot{V}_{P4}\right] \tag{6-9}$$

In the MPC framework, ANNs are needed to predict the future output of the system ($\hat{y}_{t+H_P}$) in the prediction horizon of $[t, t+H_P]$. The output of the system at the first timestep ($\hat{y}_t$) was obtained based on the feedbacked measured value at the current timestep ($t-1$). For the prediction within the left prediction horizon, the output was consecutively forecasted based on the predicted value from the ANNs. The predicted outdoor temperature (T_{out}) was obtained from the Japanese national weather service. This study assumed the cooling demand (E_{heater}) to be known in advance.

ANNs were trained using 1,886 data points collected under different operating modes, with varying flow rates and cooling load conditions. The training data was collected during the period from December of 2020 to July of 2021. The activation functions of the hidden layer and output layer are the sigmoid and linear functions, respectively. The loss function is the mean square error (MSE), and the training optimization algorithm is the Levenberg–Marquart algorithm [84,85]. The epoch was set to 1,000 based on batch training.

The training dataset was randomly divided into three groups for the purpose of training, validation, and evaluation process. Therefore, 70% of the entire dataset was used for training the neural network, 15% for verification to prevent excessive training such as overfitting, and 15% for evaluating the trained ANNs. Evaluation results of trained ANNs using a 15% separated dataset are described in Fig. 6-3 and Fig. 6-4. Each ANNs showed high accuracy with the R^2 value greater than 0.9, and the RMSE value less than 0.6 °C and 0.1 kW for the prediction of temperatures and power consumption, respectively.

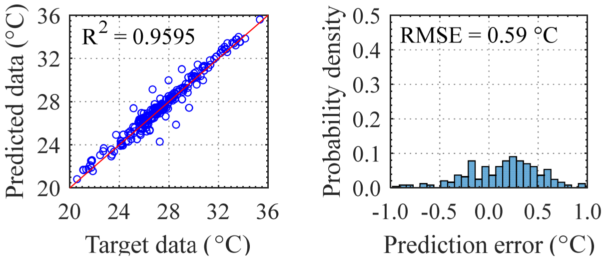

(a) ANN for water tank temperature ($n_{hl} = 2, n_{hn} = 20$)

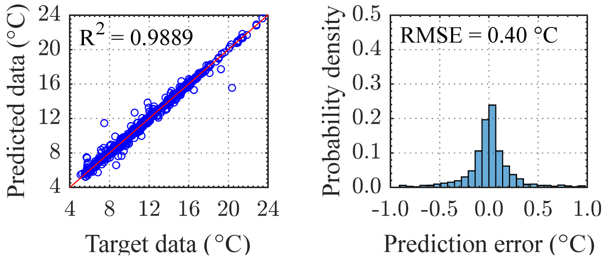

(b) ANN for TES temperatures ($n_{hl} = 2, n_{hn} = 20$)

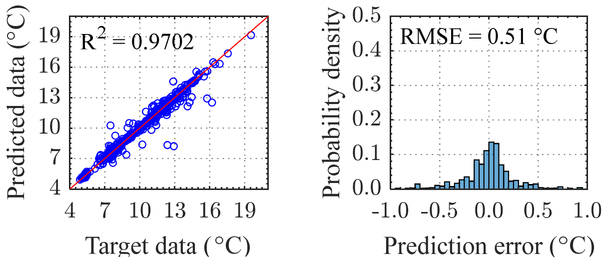

(c) ANN for chiller temperatures ($n_{hl} = 2, n_{hn} = 30$)

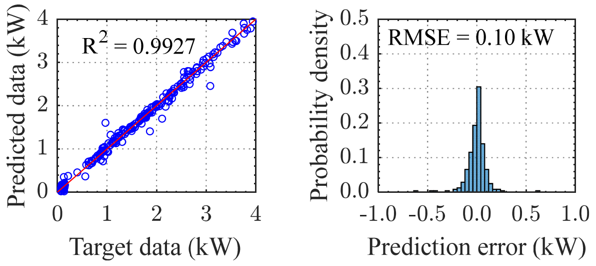

(d) ANN for chiller power consumption ($n_{hl} = 2, n_{hn} = 20$)

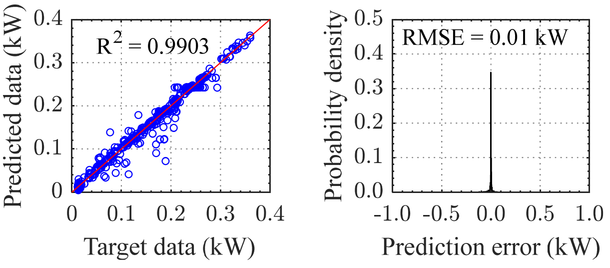

(e) ANN for pumps' power consumption ($n_{hl} = 2, n_{hn} = 20$)

Fig. 6-3. Evaluation results of trained ANNs for time series prediction evaluation using the separate datasets (n_{hl} is the number of hidden layers and n_{hn} is the number of hidden neurons).

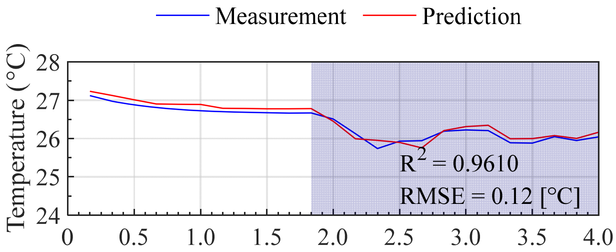

(A) ANN for water tank temperature ($n_{hl} = 2, n_{hn} = 20$)

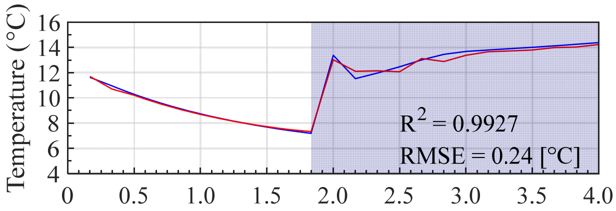

(a) Top

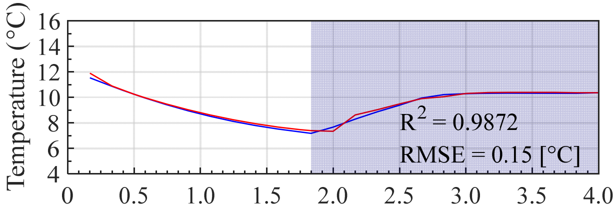

(b) Middle

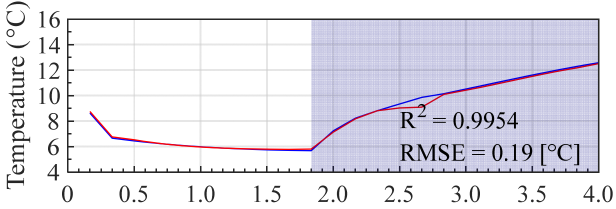

(c) Bottom

(B) ANN for TES temperatures ($n_{hl} = 2, n_{hn} = 20$)

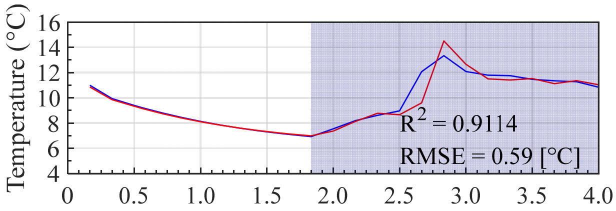

(a) Inlet

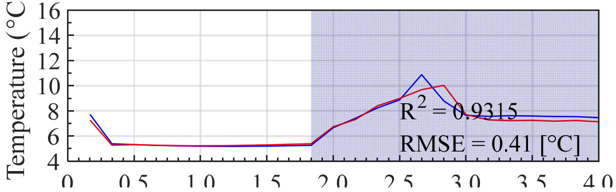

(b) Outlet

(C) ANN for chiller temperatures ($n_{hl} = 2, n_{hn} = 30$)

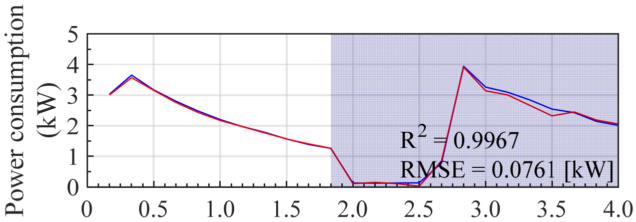

(D) ANN for chiller power consumption ($n_{hl} = 2, n_{hn} = 20$)

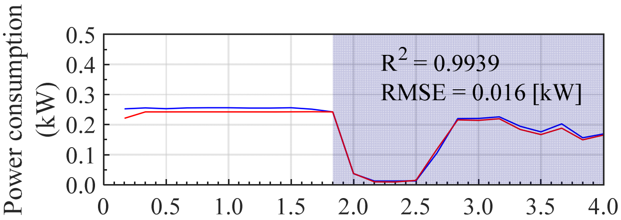

(a) Pump 1

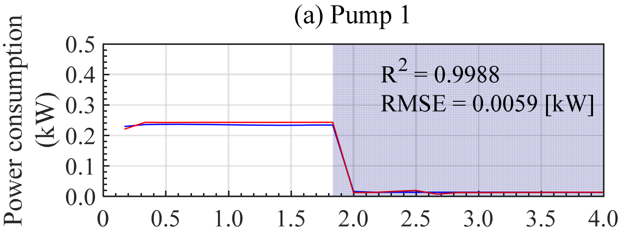

(b) Pump 2

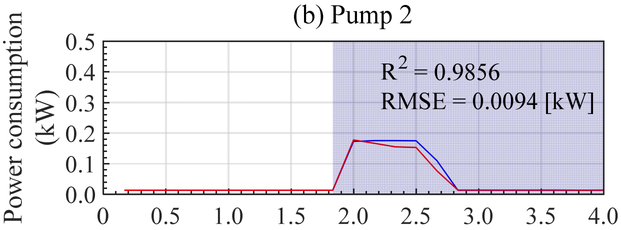

(c) Pump 3

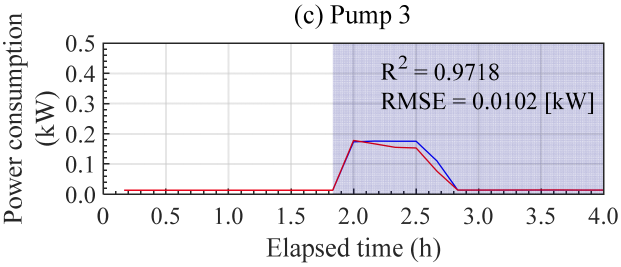

(d) Pump 4

(E) ANN for pumps' power consumption ($n_{hl} = 2, n_{hn} = 20$)

Fig. 6-4. Evaluation results of trained ANNs using the separate datasets (n_{hl} is the number of hidden layers and n_{hn} is the number of hidden neurons).

6.2.2. Optimization problem

The objective function of the MPC scheme is to minimize the total operating cost considering the variation of electricity prices with time (P) in Fig. 6-2, by manipulating the flow rates of pumps on the primary side (Equations. (6-10)–(6-11)).

$$min(J_s) = \sum_{i=t}^{t+H_P} \left\{ \left(E_{chiller}^{i} + \sum_{n=1}^{4} E_{Pn}^{i} \right) \cdot P^{i} \right\} \tag{6-10}$$

$$J_s = f\left(\dot{V}_{P1}, \dot{V}_{P2}, \dot{V}_{P3}, \dot{V}_{P4}\right) \tag{6-11}$$

The constraints were to maintain the water tank temperature at the cooling setpoint temperature of 26 °C during the cooling mode (Equation. (6-12)) and to determine the flow rate of the pump within the operational range (Equations. (6-13)–(6-20)).

$$T_{tank} = 26 \ \ ^{\circ}\text{C during cooling operation} \tag{6-12}$$

If cooling demand is zero ($E_{heater} = 0$)

$$\dot{V}_{P1} = \{x \mid x = 0, \text{or } 25 \le x \le 36.3\} \ \ [\text{L/min}] \tag{6-13}$$

$$\dot{V}_{P2} = \{x \mid x = 0, \text{or } 16.2 \le x \le 36.3\} \ \ [\text{L/min}] \tag{6-14}$$

$$\dot{V}_{P3} = 0 \ \ [\text{L/min}] \tag{6-15}$$

$$\dot{V}_{P4} = 0 \ \ [\text{L/min}] \tag{6-16}$$

else ($E_{heater} > 0$)

$$\dot{V}_{P1} = \{x \mid x = 0, \text{or } 25 \le x \le 36.3\} \ \ [\text{L/min}] \tag{6-17}$$

$$\dot{V}_{P2} = 0 \ \ [\text{L/min}] \tag{6-18}$$

$$\dot{V}_{P3} = \{x \mid x = 0, \text{or } 16.2 \le x \le 36.3\} \ \ [\text{L/min}] \tag{6-19}$$

$$\dot{V}_{P1} = \{x \mid x = 0, \text{or } 16.2 \le x \le 36.3\} \ \ [\text{L/min}] \tag{6-20}$$

Also, when the experimental system was operated as in cooling mode, it is necessary to restrict the flow rate of the inflowing chilled water to the secondary side because of the size of the header.

However, if the optimization solver finds the optimal solution of the pumps flow rate as in operation mode 3, i.e., the parallel cooling operation both with TES discharging and chiller operation, the sum of inflowing flow rate to the secondary side exceeds the design maximum flow rate of 46 L/min for the header pipe. Therefore, the constraint described in Equation. (6-21) was also considered.

If $E_{heater} > 0,\ \dot{V}_{P1} > 0$, and $\dot{V}_{P3} \& \dot{V}_{P4} > 0$

$$\dot{V}_{P1} + \dot{V}_{P4} \leq 46\ \text{L/min} \tag{6-21}$$

The mean temperature of the TES tank was restricted to 6 °C during the charging operation and 11 °C during the discharging operation (Equation (6-22)).

$$f(\bar{T}_{TES}) = \begin{cases} stop\ charging & (\bar{T}_{TES} \leq 6\,°C) \\ stop\ discharging & (\bar{T}_{TES} \geq 11\,°C) \end{cases} \tag{6-22}$$

In the MPC scheme, the prediction horizon (H_P) was set as 24 h (corresponds to 4 h in experimental scale), and control input was assigned at 1 h (10 min in experimental scale) intervals. For the optimization calculation, the εDE-RJ [35] was utilized, and a total of 300 iterative calculations per control timestep with 10 populations and 30 generations were performed.

6.3. Results and discussion

6.3.1. High cooling load schedule

6.3.1.1 Heat removal

Table 6-1 shows the results of the cumulative heat removal on the secondary side in each case during the cooling operation. There was a difference of 7.38% between RBC and MPC cases when the high cooling demand schedule was tested. Such differences are considered reasonable while comparing the operational strategies of the cooling operations of each case.

Table 6-1. Comparison of the cumulative heat removlas in the secondary side when high cooling demands was tested in each case of RBC and MPC.

	Case	
	RBC	MPC
Cumulative heat removals (kWh)	20.82	22.48

6.3.1.2 Water tank temperature

Fig. 6-5 shows the control results of water tank temperature in each RBC and MPC case when the high cooling load pattern was tested. For the high pattern of cooling demand schedules, it was difficult for RBC strategy to maintain the water tank temperature at the setpoint temperature of 26 °C. On the other hand, in the case of the MPC strategy, the MSE with respect to the error between the cooling setpoint temperature was 0.05 °C.

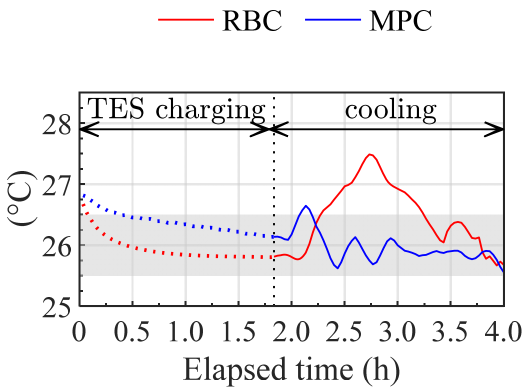

Fig. 6-5. Control results of the water tank temperature when high cooling demands was tested in each case.

6.3.1.3 Energy used in water loops

Fig. 6-6 shows the energy used in each water loop on the primary side. In the RBC case, since the TES discharging operation starts as a cooling operation, the average temperature in the heat storage tank increases, and the cooling efficiency decreases as time elapses. Therefore, in the case of the high cooling load pattern, the temperature in the water tank rises steadily. Even after switching to cooling operation from the TES discharging operation to the chiller operation (at the time of 2.5 h), it took time for the chiller to stably supply 7 °C cold water to the secondary side, so the temperature inside the water tank deviated significantly from the set temperature. On the other hand, in the MPC strategy, it can be confirmed that the cooling operation is stable while switching between the chasing operation and the cooling operation from the chiller.

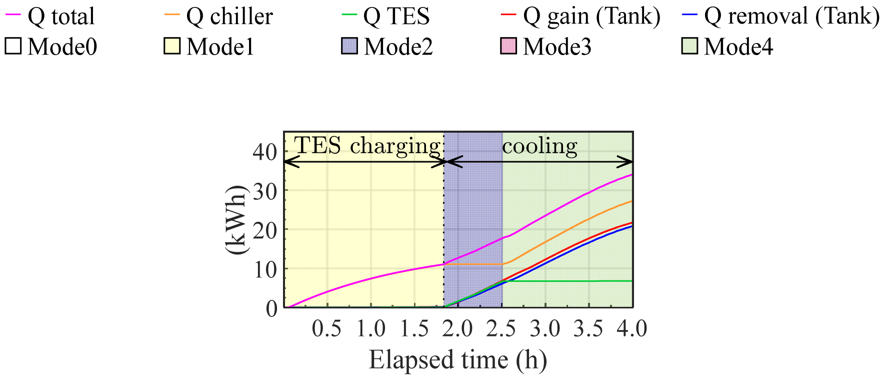

(a) Cummulative energy (RBC)

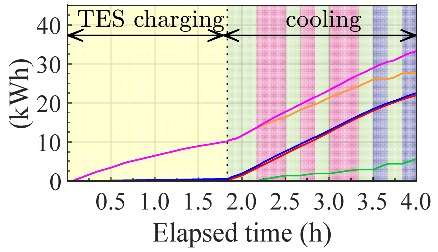

(b) Cumulative energy (MPC)

Fig. 6-6. Operation modes and cumulative energy used in each water loop of each case when high cooling demands was tested.

*Note that Mode 0 is stop status, Mode 1 is TES charging operation, Mode 2 is cooling operation with TES discharging, Mode 3 is cooling operation with TES discharging and chiller operation, and Mode 4 is cooling operation with chiller operation.

6.3.1.4 SOC of the TES

Fig. 6-7 shows the state of charge (SOC) of the TES tank in each case. The SOC which is an index to evaluate a fully charged state as 1 and a fully discharged state as 0, can be calculated based on the following Equation. (6-23).

$$SOC = \frac{\bar{T}_{TES,max} - \bar{T}^{t}{}_{TES}}{\bar{T}_{TES,max} - \bar{T}_{TES,min}} \tag{6-23}$$

Where the $\bar{T}_{TES,max}$ is the maximum setpoint temperature to fully discharge assumed as 11 °C, the $\bar{T}_{TES,min}$ is the minimum setpoint temperature to fully charge assumed as 6 °C, and the $\bar{T}^{t}{}_{TES}$ is the average of top, middle, and bottom layer of the TES tank at the current timestep.

In the RBC case, the TES discharging operation was operated as soon as the cooling operation started. The SOC was about 0.9 when the charging operation finished, however, as soon as the TES discharging operation started, the SOC decreased to about 0.6. Then the discharging operation was continued for about 40 minutes. In the MPC case, the TES tank was charged until the SOC was about 0.8. During the cooling operation, in the MPC case, the SOC decreased slowly by changing the operation modes rather than insisting only on discharging operation and let SOC decreases rapidly. At the last 30 minutes in the experiment, MPC strategy operated the system with the operation mode 2 of TES discharging operation where the electricity is assumed as high.

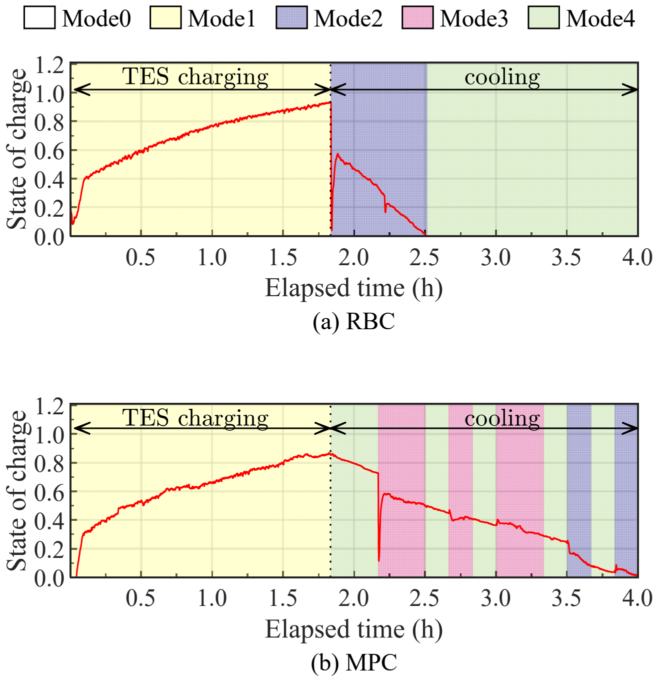

Fig. 6-7. Operation modes and state of charge of TES tank of each case when high cooling demands was tested.

*Note that Mode 0 is stop status, Mode 1 is TES charging operation, Mode 2 is cooling operation with TES discharging, Mode 3 is cooling operation with TES discharging and chiller operation, and Mode 4 is cooling operation with chiller operation.

6.3.1.5 Operation cost

Fig. 6-8 shows the results of the cumulative cost of each case. In MPC, the chiller was operated mainly with operation mode 3 where the electricity price was high, and the TES discharging operation was performed in the duration where the electricity price was low. However, while the operating cost for the TES charging operation of RBC strategy was higher than MPC strategy, the temperature control of the water tank was not stable, so it can be said that the operation of MPC was more effective for the temperature regulation for the secondary side.

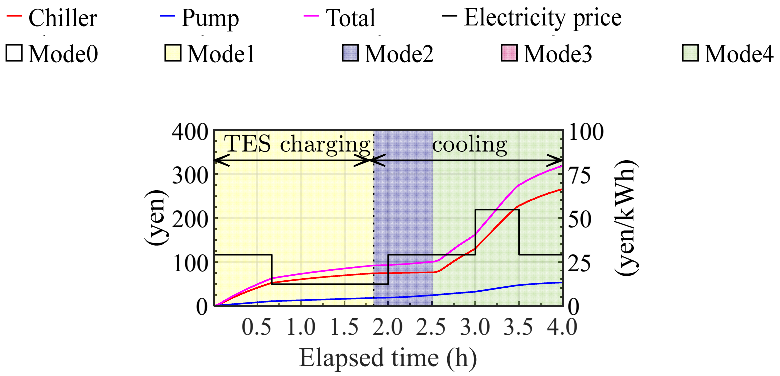

(a) Cumulative cost (RBC)

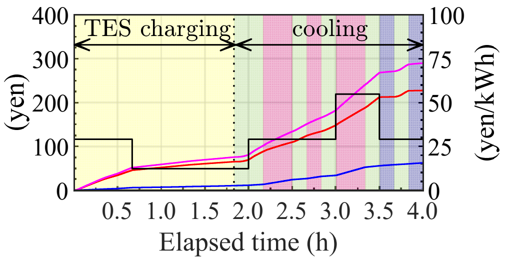

(b) Cumulative cost (MPC)

Fig. 6-8. Operation modes and cumulative costs of each case used in each equipment of the experimental system when high cooling demands was tested.

*Note that Mode 0 is stop status, Mode 1 is TES charging operation, Mode 2 is cooling operation with TES discharging, Mode 3 is cooling operation with TES discharging and chiller operation, and Mode 4 is cooling operation with chiller operation.

As a result, the total operating cost was reduced by 9.06% compared to RBC by using MPC (see Fig. 6-9). The degree of reduction in operating costs was greater in heat storage operation than in cooling operation.

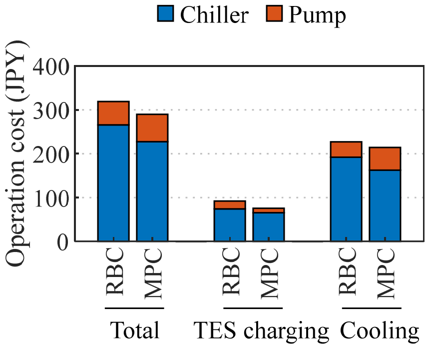

Fig. 6-9. Cumulative costs of the chiller and pumps of each case when high cooling demands was tested.

6.3.2. Medium cooling load schedule

6.3.2.1 Heat removal

Table 6-2 shows the results of the cumulative heat removal on the secondary side in each case during the cooling operation. There was a difference of 5.9% between RBC and MPC casees when the medium cooling demand schedule was tested. Such differences are considered reasonable while comparing the operational strategies of the cooling operations of each case.

Table 6-2. Comparison of the cumulative heat removlas in the secondary side when medium cooling demands was tested in each case of RBC and MPC.

	Case	
	RBC	MPC
Cumulative heat removals (kWh)	16.57	17.62

6.3.2.2 Water tank temperature

In the case of the medium cooling load pattern, the temperature inside the water tank was controlled within the range of ± 0.5 °C between the cooling setpoint temperature of 26 °C in both RBC and MPC cases (see Fig. 6-10).

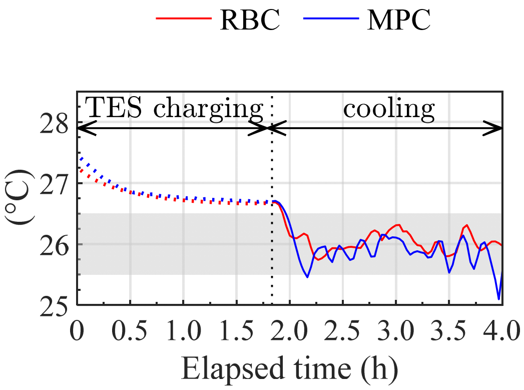

Fig. 6-10. Control results of the water tank temperature when medium cooling demands was tested in each case.

6.3.2.3 Energy used in water loops

Fig. 6-11 shows the energy used in each water loop on the primary side when the medium cooling load schedule was tested. Even in the medium cooling load pattern, the operation schedule of the MPC strategy was mainly with the operation mode of mode 3 and mode 4. However, when the electricity is assumed as high, the MPC tried to operate the system with the operation mode of TES discharging operation (mode 2). In RBC, the TES discharging operation was completed 2.6 h after the start of the experiment, and it was almost the same as when it was operated in the high cooling load pattern. However, the temperature of the water tank was controlled more stably in the medium cooling load schedule than the high cooling load schedule.

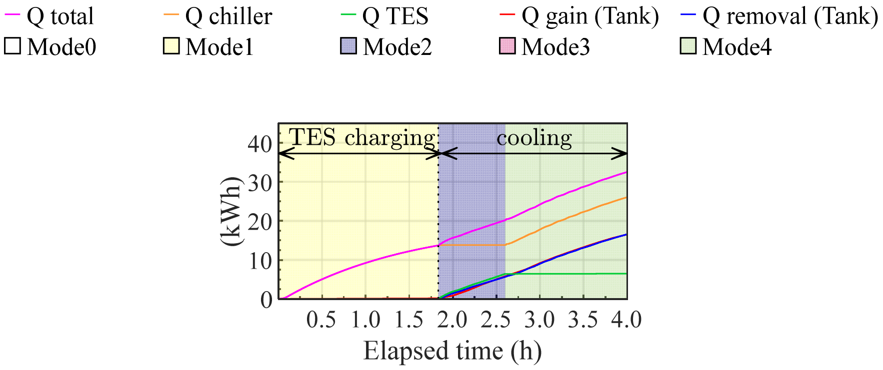

(a) Cummulative energy (RBC)

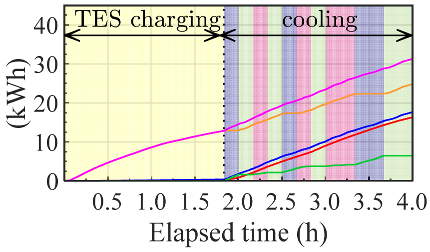

(b) Cumulative energy (MPC)

Fig. 6-11. Operation modes and cumulative energy used in each water loop of each case when medium cooling demands was tested.

*Note that Mode 0 is stop status, Mode 1 is TES charging operation, Mode 2 is cooling operation with TES discharging, Mode 3 is cooling operation with TES discharging and chiller operation, and Mode 4 is cooling operation with chiller operation.

6.3.2.4 SOC of the TES

Fig. 6-12 shows the SOC of the TES tank in each case when the medium cooling load schedule was tested. In the RBC case, the SOC was about 0.82 when the charging operation finished, however, as soon as the TES discharging operation started, the SOC decreased to about 0.4. Then the discharging operation was continued for about 45 minutes. In the MPC case, the TES tank was charged until the SOC was about 0.8. During the cooling operation, in the MPC case, the SOC decreased slowly by changing the operation modes rather than insisting only on discharging operation and let SOC decreases rapidly.

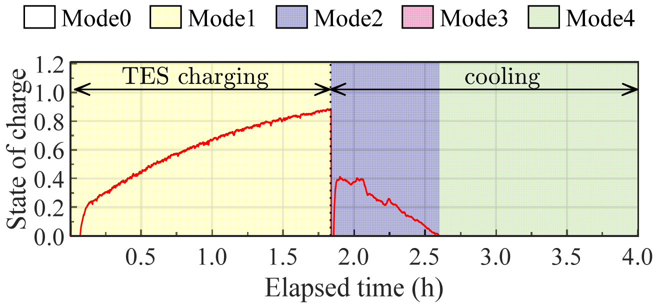

(a) RBC

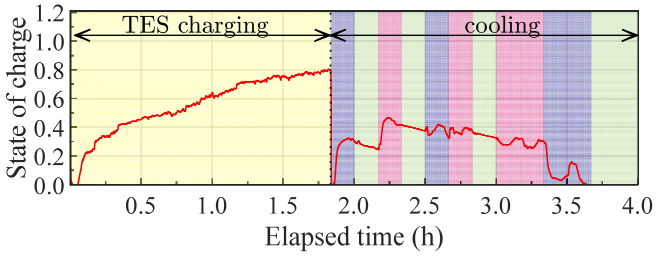

(b) MPC

Fig. 6-12. Operation modes and state of charge of TES tank of each case when medium cooling demands was tested.

*Note that Mode 0 is stop status, Mode 1 is TES charging operation, Mode 2 is cooling operation with TES discharging, Mode 3 is cooling operation with TES discharging and chiller operation, and Mode 4 is cooling operation with chiller operation.

6.3.2.5 Operation cost

As a result, in the medium cooling load pattern, in the case of the MPC strategy, there were plans to operate the chiller when the electricity price is high and to discharge the TES tank when the electricity price is low (see Fig. 6-13). However, as a result, the MPC reduced the total operating cost by 9.29% compared to RBC (see and Fig. 6-14). Similar to the high cooling load pattern, MPC employed the TES charging operation further less than the RBC strategy to reduce operating costs more than in the cooling operation.

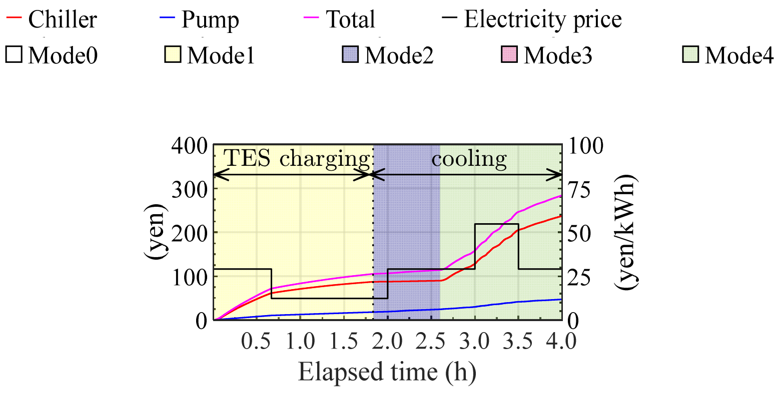

(a) Cumulative cost (RBC)

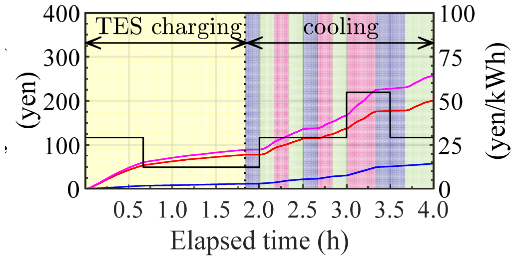

(b) Cumulative cost (MPC)

Fig. 6-13. Operation modes and cumulative costs of each case used in each equipment of the experimental system when medium cooling demands was tested.

*Note that Mode 0 is stop status, Mode 1 is TES charging operation, Mode 2 is cooling operation with TES discharging, Mode 3 is cooling operation with TES discharging and chiller operation, and Mode 4 is cooling operation with chiller operation.

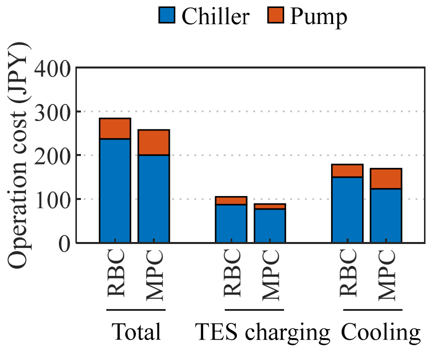

Fig. 6-14. Cumulative costs of the chiller and pumps of each case when medium cooling demands was tested.

6.3.3. Low cooling load schedule

6.3.3.1 Heat removal

Table 6-3 shows the results of the cumulative heat removal on the secondary side in each case during the cooling operation. There was a difference of 0.49% between RBC and MPC casees when the medium cooling demand schedule was tested. Such differences are considered reasonable while comparing the operational strategies of the cooling operations of each case.

Table 6-3. Comparison of the cumulative heat removlas in the secondary side when low cooling demands was tested in each case of RBC and MPC.

	Case	
	RBC	MPC
Cumulative heat removals (kWh)	14.01	14.08

6.3.3.2 Water tank temperature

In the case of the low cooling load pattern, because the cooling demand was assumed as low during the daytime, the water tank temperature in both RBC and MPC strategy was regulated in the region slightly lower than the setpoint temperature of 26 °C (see Fig. 6-15). However, in both cases, the water tank temperature was well maintained within ± 0.5 °C of the cooling setpoint temperature.

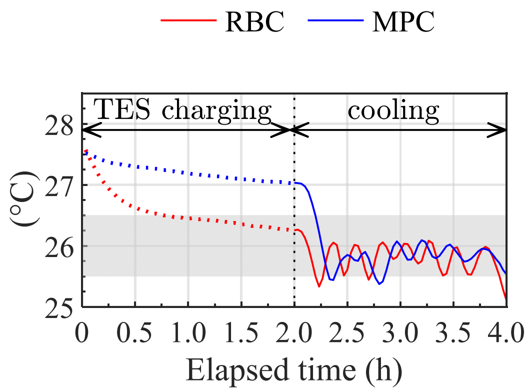

Fig. 6-15. Control results of the water tank temperature when low cooling demands was tested in each case.

6.3.3.3 Energy used in water loops

Fig. 6-16 shows the results of the energy used in each water loop on the primary side when the low cooling load schedule was tested. In the case of RBC, the time from the start of the TES discharging operation exceeded 1 hour, and it took about 30 minutes longer than the result of the high cooling load or medium cooling load patterns. In the case of MPC strategy, the cooling operation only by the TES discharging operation (Mode 3) was most frequently occurred rather than using the chiller to cool down the water tank.

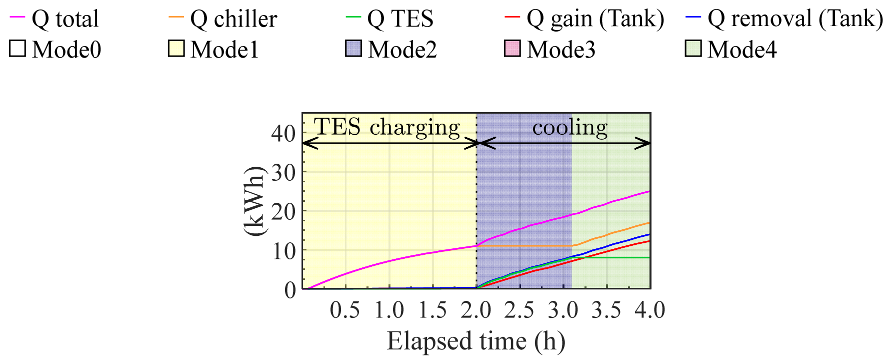

(a) Cummulative energy (RBC)

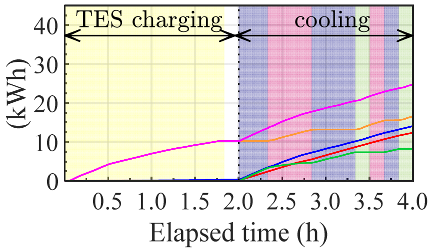

(b) Cumulative energy (MPC)

Fig. 6-16. Operation modes and cumulative energy used in each water loop of each case when low cooling demands was tested.

*Note that Mode 0 is stop status, Mode 1 is TES charging operation, Mode 2 is cooling operation with TES discharging, Mode 3 is cooling operation with TES discharging and chiller operation, and Mode 4 is cooling operation with chiller operation.

6.3.3.4 SOC of the TES

Fig. 6-17 shows the SOC of the TES tank in each case when the low cooling load schedule was tested. In the RBC case, the SOC was about 0.9 when the charging operation finished, however, as soon as the TES discharging operation started, the SOC decreased to about 0.6. Then the discharging operation was continued for about 1 hour. In the MPC case, the TES tank was charged until the SOC was about 0.85 and stopped the charging operation at the last control time step. It is inferred that since the cooling demand assumed to be known in advance is low during the daytime, the MPC would try not to fully charge the TES tank. Therefore, the SOC in the MPC strategy increased up to 0.85 and naturally decreased to about 0.7. During the cooling operation, in the MPC case, the SOC decreased slowly by changing the operation modes rather than insisting only on discharging operation and let SOC decreases rapidly.

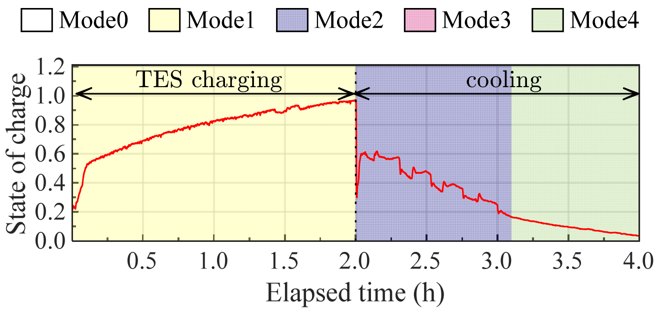

(a) RBC

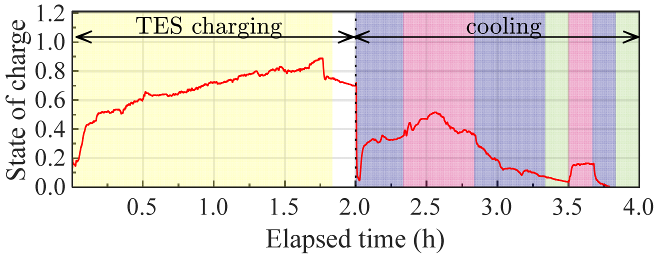

(b) MPC

Fig. 6-17. Operation modes and state of charge of TES tank of each case when low cooling demands was tested.

*Note that Mode 0 is stop status, Mode 1 is TES charging operation, Mode 2 is cooling operation with TES discharging, Mode 3 is cooling operation with TES discharging and chiller operation, and Mode 4 is cooling operation with chiller operation.

6.3.3.5 Operation cost

Fig. 6-18 shows the cumulative operating cost of each case when the low cooling demand schedule was tested. The MPC strategy discharged the TES tank generally when the electricity prices were assumed as high. Ultimately, MPC reduced total operating costs by 14.56% over RBC as shown in Fig. 6-19. However, the operating cost of the MPC strategy in cooling operation was similar to that of the RBC strategy. It is inferred that since the MPC didn't charge the TES tank as much as the RBC strategy, it would try to reduce the operating cost more in the charging operation rather than in the cooling operation.

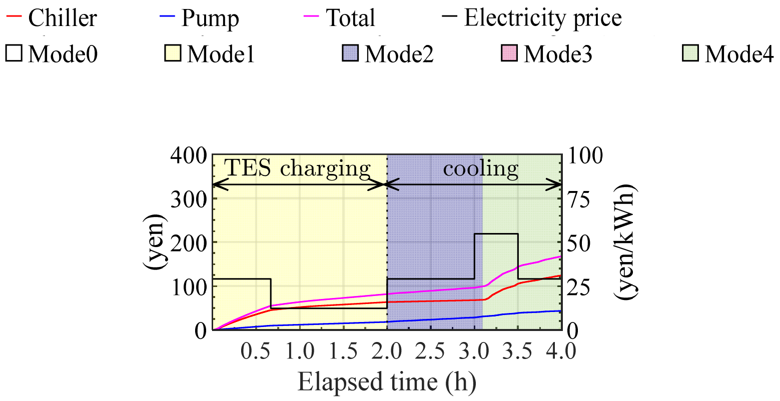

(a) Cumulative cost (RBC)

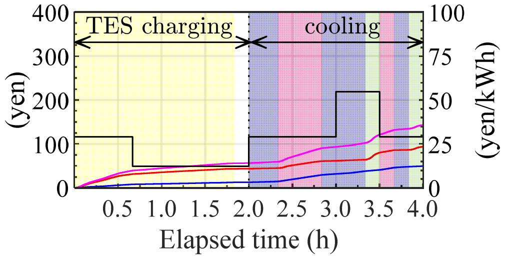

(b) Cumulative cost (MPC)

Fig. 6-18. Operation modes and cumulative costs of each case used in each equipment of the experimental system when low cooling demands was tested.

*Note that Mode 0 is stop status, Mode 1 is TES charging operation, Mode 2 is cooling operation with TES discharging, Mode 3 is cooling operation with TES discharging and chiller operation, and Mode 4 is cooling operation with chiller operation.

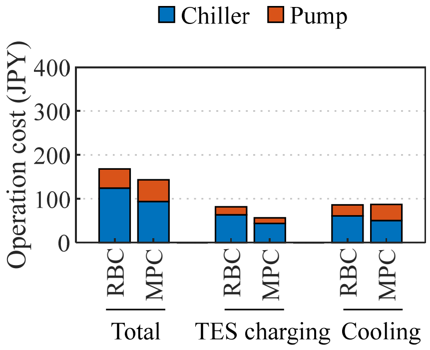

Fig. 6-19. Cumulative costs of the chiller and pumps of each case when low cooling demands was tested.

6.4. Conclusion

In this study, the MPC strategy was developed using AI techniques and applied to an experimental setup that mimics a building energy system with TES. Experiments were conducted to verify the practicality of the developed AI-based MPC strategy. The MPC results were compared by the RBC strategy that prioritizes the TES. For the experiment to validate the developed AI-based MPC strategy, three different patterns of cooling load schedules (i.e., high, medium, and low cooling load schedules during the daytime) were assumed and tested. As a result, this control method reduced the total operating cost by 9.06–14.56% compared to the RBC. In addition, different operation plan results were obtained depending on the load pattern. Therefore, it is considered that energy-efficient real-time optimal control can be realized by using the AI-based MPC proposed in this study.

Chapter 7. Experimental analysis of AI-based MPC compared to different RBC strategies

Chapter 7.
Experimental analysis of AI-based MPC compared to different RBC strategies

7.1. Experimental condition

The effectiveness of the above MPC strategy was verified by comparing it with a rule-based control (RBC) which was also measured using the same experimental setup described in Chapter 5 (see also Fig. 5-2). This study defined the RBC strategy to prioritize the TES operation based on PID controllers. The TES was charged during the non-cooling operation hours at a nominal flow rate of 36.3 L/min to lower the mean tank temperature to 6 °C. The discharging operation was conducted until the mean tank temperature increased to 11 °C. The flow rate of the pump for the TES discharging operation (P-3 and P-4) was manipulated by the PID controllers to send the chilled water at 7 °C to the secondary side, and maintain the tank temperature at 26 °C detailed conditions for PID controllers in RBC strategy can be found in Table 5-3.

Also, an accelerated experiment that shortens the day from 24 hours to 4 hours was conducted. The experiment was started from the charging operation where the chiller sends to charge the TES tank assuming that the time of the occupancy during a day ends at night. The representative cooling load generated from the electric immersion heater is illustrated in Fig. 7-1. The cooling setpoint temperature of the water tank during the cooling operation was set as 26 °C.

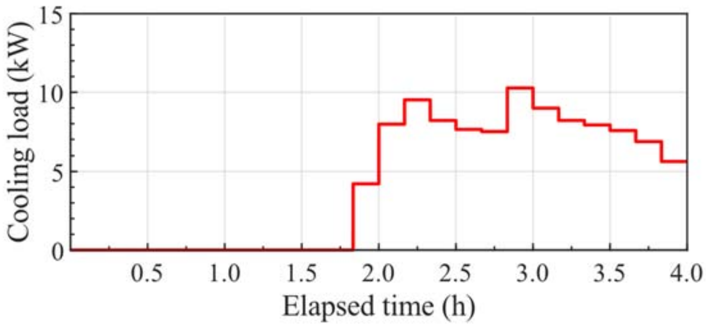

Fig. 7-1. Representative cooling load assumed to be known in advance in the experiment.

Two RBC cases were collected from the experimental system that differed in the cooling operation with TES discharging priority. The case of RBC-1 commences the TES discharging operation as soon as the cooling mode commences. However, the RBC-2 case begins the chiller cooling operation by itself, and the TES begins discharging when the electricity price is highest during the occupied hours. The results from the two RBC cases were compared with those of the MPC strategy. In the MPC strategy, a plan of electricity price is assumed as shown in Fig. 7-2. The cooling demand and electricity prices, that this study assumed to be known in advance.

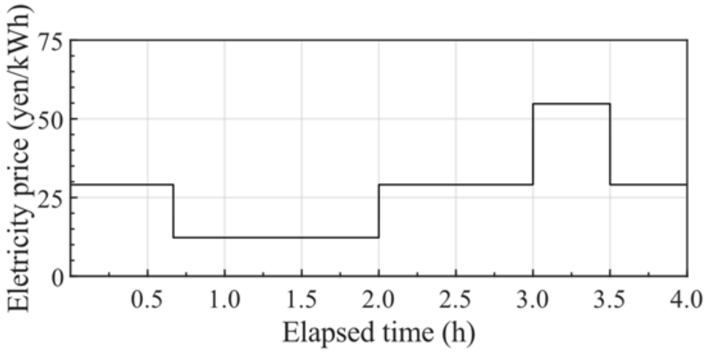

Fig. 7-2. Time-variant electricity prices assumed to be known in advance in the experiment.

7.2. Implementation of MPC strategy

7.2.1. ANN prediction models

Five ANN models with different prediction targets were constructed. The prediction targets are the water tank temperature, TES tank temperatures (top, middle, and bottom layers), chiller inlet/outlet temperatures, and power consumption of the chiller and the pumps. Equations (7-1)–(7-5) show the input parameters required to predict each prediction target. The input parameters were selected empirically, considering the influence between the prediction targets. The flow rates of pumps on the primary side are included as input parameters in every ANN because the behavior of the prediction target can be captured by varying the control variables.

$$\hat{y}(T_{tank}^{t}) = ANN\left(T_{out}^{t-1}, T_{env}^{t-1}, E_{heater}^{t}, T_{tank}^{t-1}, \dot{V}_{P5}^{t-1}, \dot{V}_{P}^{t}\right) \quad (7\text{-}1)$$

$$\hat{y}(T_{TES}^{t}) = ANN\left(T_{env}^{t-1}, T_{tank}^{t}, T_{TES}^{t-1}, \dot{V}_{P}^{t}\right) \quad (7\text{-}2)$$

$$\hat{y}(T_{chiller}^{t}) = ANN\left(T_{out}^{t}, T_{tank}^{t}, T_{TES}^{t}, T_{chiller}^{t-1}, \dot{V}_{P}^{t}\right) \quad (7\text{-}3)$$

$$\hat{y}(E_{chiller}^{t}) = ANN\left(T_{out}^{t}, T_{tank}^{t}, T_{TES}^{t}, T_{chiller}^{t}, \dot{V}_{P}^{t}\right) \quad (7\text{-}4)$$

$$\hat{y}(E_P^t) = ANN(\dot{V}_P^t) \quad (7\text{-}5)$$

where

$$T_{TES} = [T_{TES,top}, T_{TES,mid}, T_{TES,bot}] \quad (7\text{-}6)$$

$$T_{chiller} = [T_{chiller,in}, T_{chiller,out}] \quad (7\text{-}7)$$

$$E_P = [E_{P1}, E_{P2}, E_{P3}, E_{P4}] \quad (7\text{-}8)$$

$$\dot{V}_P = [\dot{V}_{P1}, \dot{V}_{P2}, \dot{V}_{P3}, \dot{V}_{P4}] \quad (7\text{-}9)$$

In the MPC framework, ANNs are needed to predict the future output of the system ($\hat{y}_{t+H_P}$) in the prediction horizon of $[t, t + H_P]$. The output of the system at the first timestep ($\hat{y}_t$) was obtained based on the feedbacked measured value at the current timestep ($t - 1$). For the prediction within the left prediction horizon, the output was consecutively forecasted based on the predicted value from the ANNs. The predicted outdoor temperature (T_{out}) was obtained from the Japanese national weather service. This study assumed the cooling demand (E_{heater}) to be known in advance.

ANNs were trained using 2,445 data points collected under different operating modes, with varying flow rates and cooling load conditions. The activation functions of the hidden layer and output layer are the sigmoid and linear functions, respectively. The loss function is the mean square error (MSE), and the training optimization algorithm is the Levenberg–Marquart algorithm [84,85]. The epoch was set to 1,000 based on batch training.

The training dataset was randomly divided into three groups for the purpose of training, validation, and evaluation process. Therefore, 70% of the entire dataset was used for training the neural network, 15% for verification to prevent excessive training such as overfitting, and 15% for evaluating the trained ANNs. Evaluation results of trained ANNs using a 15% separated dataset are described in Fig. 7-3. Each ANNs showed high accuracy with the R^2 value greater than 0.9, and the RMSE value less than 0.5 °C and 0.1 kW for the prediction of temperatures and power consumption, respectively.

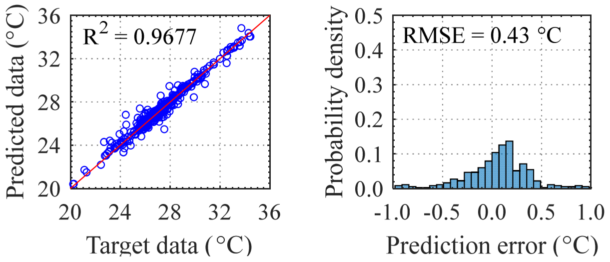

(a) ANN for water tank temperature ($n_{hl} = 2, n_{hn} = 20$)

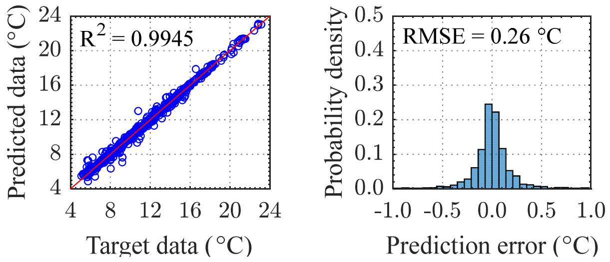

(b) ANN for TES temperatures ($n_{hl} = 2, n_{hn} = 20$)

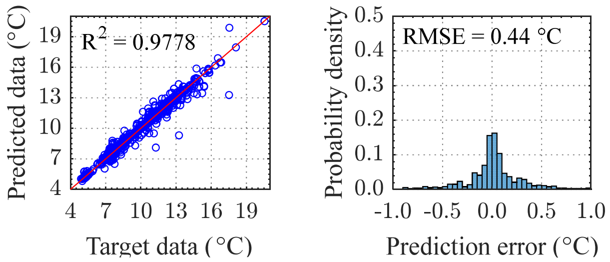

(c) ANN for chiller temperatures ($n_{hl} = 2, n_{hn} = 30$)

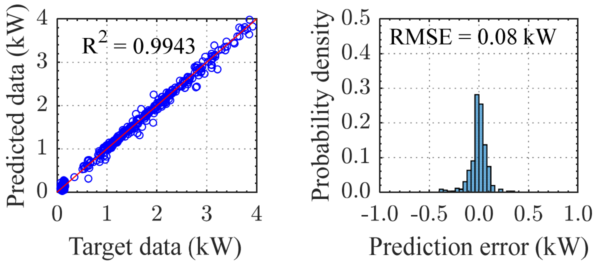

(d) ANN for chiller power consumption ($n_{hl} = 2, n_{hn} = 20$)

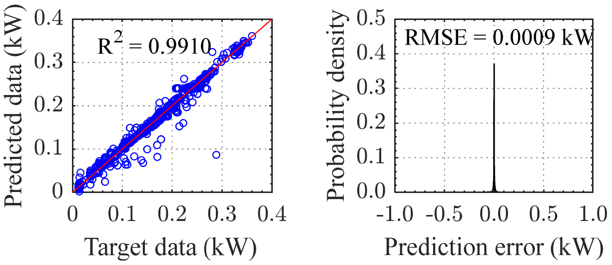

(e) ANN for pumps' power consumption ($n_{hl} = 2, n_{hn} = 20$)

Fig. 7-3. Evaluation results of trained ANNs using the separate datasets (n_{hl} is the number of hidden layers and n_{hn} is the number of hidden neurons).

7.2.2. Optimization problem

The objective function of the MPC scheme is to minimize the total operating cost considering the variation of electricity prices with time (P) in Fig. 7-2, by manipulating the flow rates of pumps on the primary side (Equations. (7-10)–(7-11)).

$$min(J_s) = \sum_{i=t}^{t+H_P} \left\{ \left(E_{chiller}^{i} + \sum_{n=1}^{4} E_{Pn}^{i} \right) \cdot P^{i} \right\} \tag{7-10}$$

$$J_s = f\left(\dot{V}_{P1}, \dot{V}_{P2}, \dot{V}_{P3}, \dot{V}_{P4}\right) \tag{7-11}$$

The constraints were to maintain the water tank temperature at the cooling setpoint temperature of 26 °C during the cooling mode (Equation. (7-12)) and to determine the flow rate of the pump within the operational range (Equations. (7-13)–(7-20)).

$$T_{tank} = 26 \ \ \text{°C during cooling operation} \tag{7-12}$$

If cooling demand is zero ($E_{heater} = 0$)

$$\dot{V}_{P1} = \{x \mid x = 0, \text{or } 25 \leq x \leq 36.3\} \ \ [\text{L/min}] \tag{7-13}$$

$$\dot{V}_{P2} = \{x \mid x = 0, \text{or } 16.2 \leq x \leq 36.3\} \ \ [\text{L/min}] \tag{7-14}$$

$$\dot{V}_{P3} = 0 \ \ [\text{L/min}] \tag{7-15}$$

$$\dot{V}_{P4} = 0 \ \ [\text{L/min}] \tag{7-16}$$

else ($E_{heater} > 0$)

$$\dot{V}_{P1} = \{x \mid x = 0, \text{or } 25 \leq x \leq 36.3\} \ \ [\text{L/min}] \tag{7-17}$$

$$\dot{V}_{P2} = 0 \ \ [\text{L/min}] \tag{7-18}$$

$$\dot{V}_{P3} = \{x \mid x = 0, \text{or } 16.2 \leq x \leq 36.3\} \ \ [\text{L/min}] \tag{7-19}$$

$$\dot{V}_{P1} = \{x \mid x = 0, \text{or } 16.2 \leq x \leq 36.3\} \ \ [\text{L/min}] \tag{7-20}$$

Also, when the experimental system was operated as in cooling mode, it is necessary to restrict the flow rate of the inflowing chilled water to the secondary side because of the size of the header.

However, if the optimization solver finds the optimal solution of the pumps flow rate as in operation mode 3, i.e., the parallel cooling operation both with TES discharging and chiller operation, the sum of inflowing flow rate to the secondary side exceeds the design maximum flow rate of 46 L/min for the header pipe. Therefore, the constraint described in Equation. (7-21) was also considered.

If $E_{heater} > 0,\ \dot{V}_{P1} > 0$, and $\dot{V}_{P3} \& \dot{V}_{P4} > 0$

$$\dot{V}_{P1} + \dot{V}_{P4} \leq 46 \ \text{L/min} \tag{7-21}$$

The mean temperature of the TES tank was restricted to 6 °C during the charging operation and 11 °C during the discharging operation (Equation (7-22)).

$$f(\bar{T}_{TES}) = \begin{cases} stop\ charging & (\bar{T}_{TES} \leq 6\,°C) \\ stop\ discharging & (\bar{T}_{TES} \geq 11\,°C) \end{cases} \tag{7-22}$$

In the MPC scheme, the prediction horizon (H_P) was set as 24 h (corresponds to 4 h in experimental scale), and control input was assigned at 1 h (10 min in experimental scale) intervals. For the optimization calculation, the εDE-RJ [35] was utilized, and a total of 300 iterative calculations per control timestep with 10 populations and 30 generations were performed.

7.3. COP correction based on COP-PLR curve

The chiller efficiency depends on the energy consumed and the cooling delivered and is affected by the ambient temperature under part-load conditions as shown in Fig. 7-4. Therefore, to properly evaluate the results under different operating conditions, the correlation between the chiller's COP and the part load ratio (PLR) at different outdoor temperatures was analyzed.

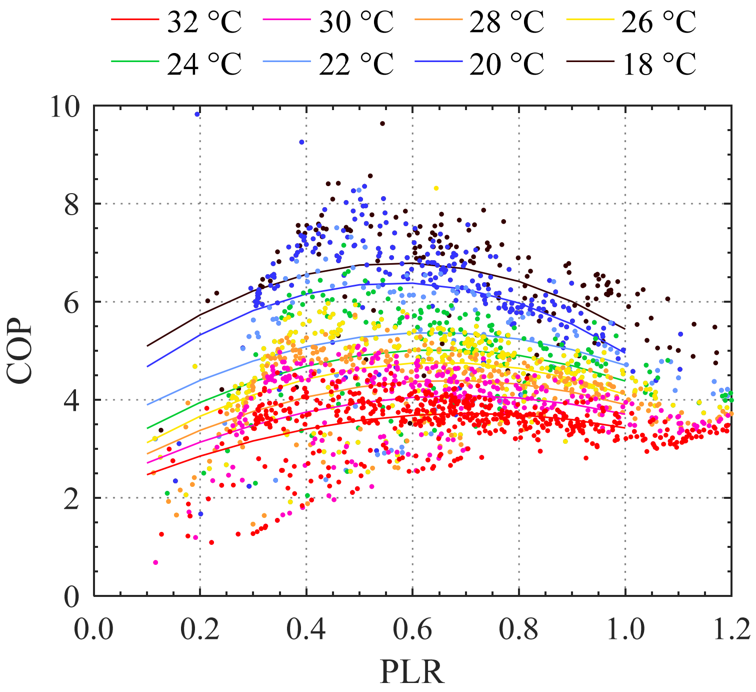

Fig. 7-4. COP-PLR curve of the air-source heat pump chiller in the experimental system at different outdoor temperatures.

Using the regression equation obtained through correlation analysis, the COP of the chiller was corrected to the value estimated to have been consumed when the chiller was operated at an outdoor reference temperature of 28°C. When the measured outdoor temperature during the experiment was included in the range between 18 °C and 32 °C, the measured COP was corrected based on interpolation using Equation. (7-23).

When $T_b < T_{out} < T_a$,

$$COP'_{exp} = COP_a + (COP_b - COP_a)\frac{T_a - T_{out}}{T_a - T_b} \tag{7-23}$$

When the measured outdoor temperature was higher than 32°C, the measured COP was corrected based on the extrapolation using Equation. (7-24).

When$T_b < T_a < T_{out}$,

$$COP'_{exp} = \frac{COP_b(T_a - T_{out}) + COP_a(T_{out} - T_b)}{T_a - T_b} \tag{7-24}$$

Also, if the measure outdoor temperature was less than 18 °C, the measured COP was corrected based on the extrapolation using Equation. (7-25).

When$T_{out} < T_b < T_a$,,

$$COP'_{exp} = \frac{COP_b(T_a - T_{out}) + COP_a(T_{out} - T_b)}{T_a - T_b} \tag{7-25}$$

The equation of correlation analysis between chiller's COP and PLR at the reference outdoor temperature of 28 °C is shown in Equation. (7-26).

$$COP_{std\ (28\,°C)} = -4.6\,PLR^2 + 6.2\,PLR + 2.3 \tag{7-26}$$

Then, the rate (ε) between the corrected COP and the COP at the reference temperature of 28 °C can be obtained using Equation. (7-27). Using the rate of ε, the electricity consumption of the chiller was adjusted based on the corrected COP and standard COP using Equation. (7-28).

$$\varepsilon = \frac{COP'_{exp}}{COP_{std\ (28\,°C)}} \tag{7-27}$$

$$E_{exp\rightarrow std} = \varepsilon\, E_{exp} = \frac{COP'_{exp}}{COP_{std\ (28\,°C)}} E_{exp} \tag{7-28}$$

7.4. Results and discussion

7.4.1. Heat removal

Table 7-1 shows the results of the cumulative heat removal on the secondary side in each case during the cooling operation. There was a difference of 0.64% between MPC and RBC-1, and 3.14% between MPC and RBC-2. Such differences are considered reasonable while comparing the operational strategies of the cooling operations of each case.

Table 7-1. Comparison of the cumulative heat removlas in the secondary side in each case of RBC-1, RBC-2, and MPC case.

	Case		
	RBC-1	RBC-2	MPC
Cumulative heat removals (kWh)	18.63	18.16	18.75

7.4.2. Water tank temperature

Fig. 7-5 shows the water tank temperature variations in the MPC and the two RBC strategies. In every case, the water tank was maintained between 25.5–26.5 °C. The MSE value between the water tank temperature and cooling setpoint temperature during the cooling operation was 0.19 °C for RBC-1, 0.17 °C for RBC-2, and 0.08 °C for MPC.

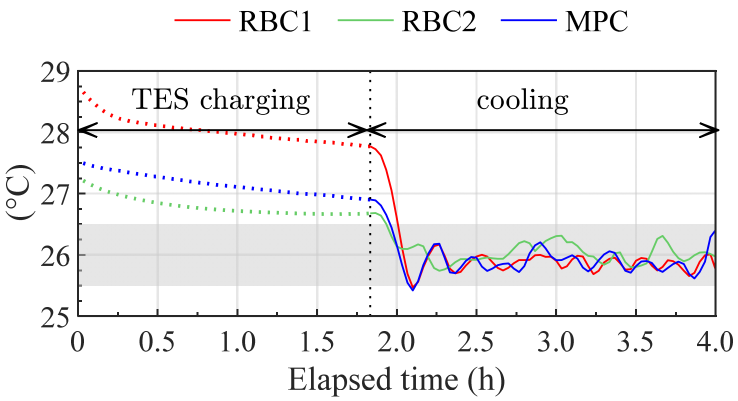

Fig. 7-5. Control results of the water tank temperature in each case.

7.4.3. Energy used in water loops

Fig. 7-6 compares the operational strategy of each case. The RBC strategy prioritizes a TES operation; however, RBC-1 commenced the discharging operation (Mode 2) as soon as the cooling operation began. RBC-2 first operated the chiller to manage the cooling load (Mode 4) and discharged the TES tank (Mode 2) when the electricity price was the highest. On the other hand, the MPC strategy estimated the system behavior for the next 24 steps at each 10 min interval and freely switched the operation modes with the best choice at the moment.

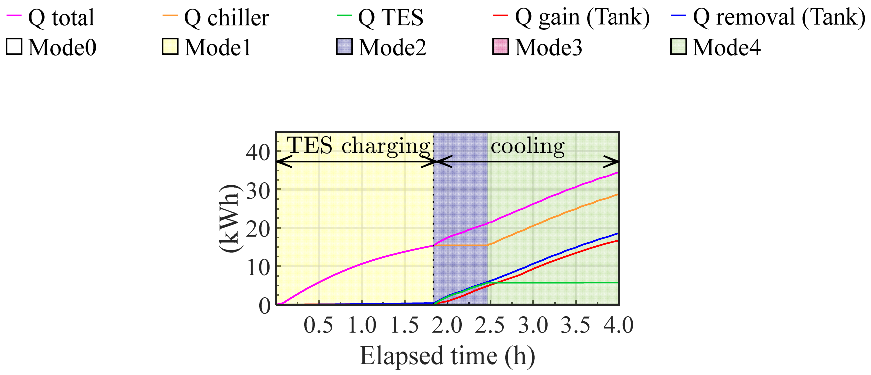

(a) Cummulative energy (RBC1)

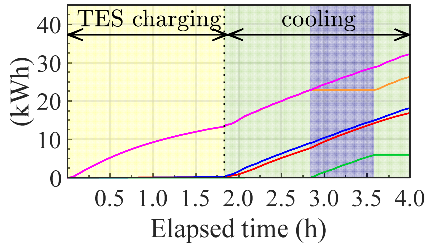

(b) Cummulative energy (RBC2)

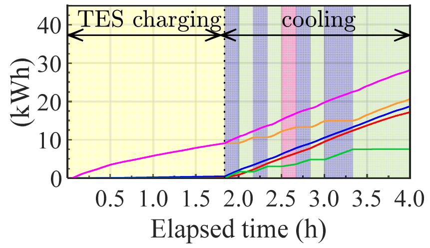

(c) Cumulative energy (MPC)

Fig. 7-6. Operation modes and cumulative energy used in each water loop of each case.

*Note that Mode 0 is stop status, Mode 1 is TES charging operation, Mode 2 is cooling operation with TES discharging, Mode 3 is cooling operation with TES discharging and chiller operation, and Mode 4 is cooling operation with chiller operation.

7.4.4. SOC of the TES

Fig. 7-7 shows the SOC of the TES tank in each case. In the RBC-1 case, the TES discharging operation was operated as soon as the cooling operation started. The SOC was about 0.85 when the charging operation finished, however, as soon as the TES discharging operation started, the SOC decreased to about 0.4. Then the discharging operation was continued for about 35 minutes. In the RBC-2 case, the TES discharging operation was commenced when the electricity price is highest during the day. When the TES charging operation was finished, the SOC was about 0.85, however, it decreased naturally to about 0.6 and the TES discharging operation was continued about 0.7 hours more than the RBC-1 case. In the MPC case, the TES tank was charged until the SOC was about 0.85. During the cooling operation, in the MPC case, the SOC decreased slowly by changing the operation modes rather than insisting only on discharging operation and let SOC decreases rapidly.

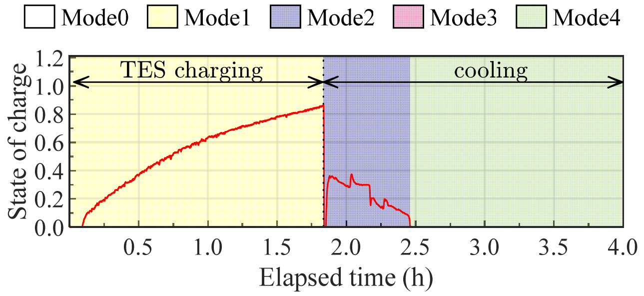

(a) RBC1

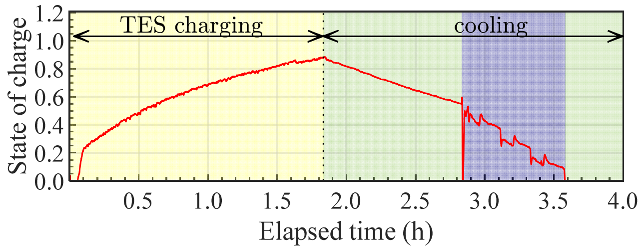

(b) RBC2

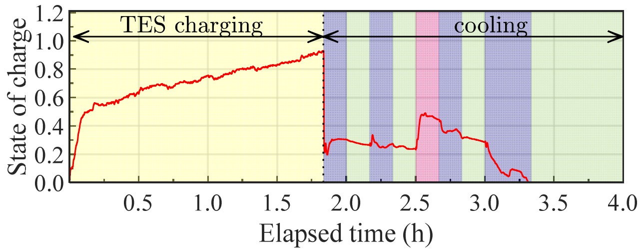

(c) MPC

Fig. 7-7. Operation modes and state of charge of TES tank of each case.

*Note that Mode 0 is stop status, Mode 1 is TES charging operation, Mode 2 is cooling operation with TES discharging, Mode 3 is cooling operation with TES discharging and chiller operation, and Mode 4 is cooling operation with chiller operation.

7.4.5. Operation cost

In the RBC-1 case, the TES discharging operation took priority as soon as the cooling operation started, which means that the TES discharging operated in such a way that it cannot further save operating costs. However, RBC-2 gave priority to the TES discharging operation when the electricity price is the highest during the day; therefore, RBC-2 could save the operating cost by 14.1% compared to RBC-1 (Fig. 7-8).

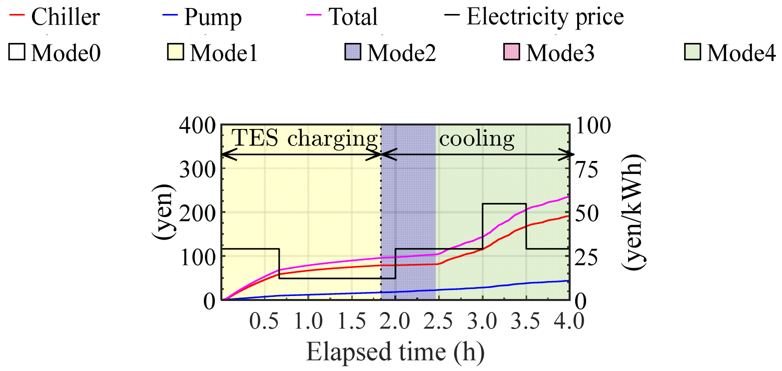

(a) Cumulative cost (RBC1)

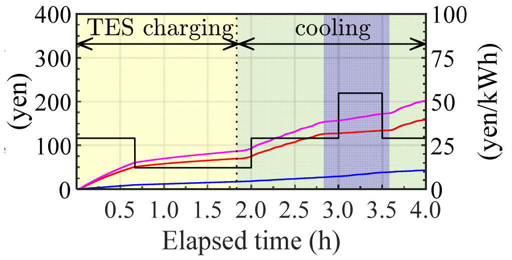

(b) Cumulative cost (RBC2)

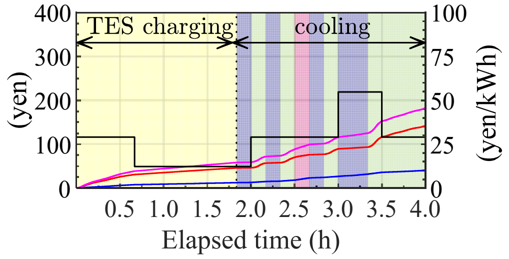

(c) Cumulative cost (MPC)

Fig. 7-8. Operation modes and cumulative costs of each case used in each equipment of the experimental system.

*Note that Mode 0 is stop status, Mode 1 is TES charging operation, Mode 2 is cooling operation with TES discharging, Mode 3 is cooling operation with TES discharging and chiller operation, and Mode 4 is cooling operation with chiller operation.

However, MPC could reduce the operating cost further than both RBC strategies by optimally manipulating the flow rates of the pump on the primary side based on the prediction of system behavior from ANNs (by 22.5% compared to RBC-1 and 9.7% compared to RBC-2, see in Fig. 7-9). Savings in operating costs in the MPC case were further better during the TES charging operation compared to the two RBC strategies. However, during the cooling operation, MPC was able to reduce the cost by as much as 11% compared to RBC-1. However, compared to RBC-2, MPC showed larger costs of about 7.5%.

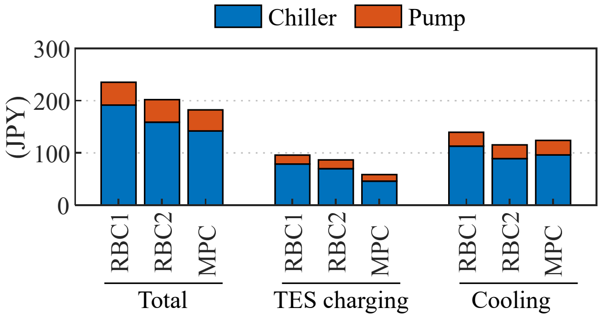

Fig. 7-9. Cumulative costs of the chiller and pumps of each case.

7.5. Conclusion

In this study, the MPC strategy was developed using AI techniques and applied to an experimental setup that mimics a TES building energy system. Experiments were conducted to verify the practicality of the AI-based MPC strategy. The MPC results were compared to two RBC strategies that prioritize TES operation and discharge the TES either when the cooling operation commences, or when the electricity price is the highest. The AI-based MPC could reduce operating costs by 9.7–22.5% compared to the RBC strategies.

Chapter 8. Conclusion and further research

Chapter 8. Conclusion and further research

In the present thesis, a model predictive control (MPC) strategy using artificial intelligence (AI) was proposed to secure the practicality and applicability. Also, a developed AI-based MPC strategy was investigated and analyzed based on both simulation and experimental results. The research flow and the achievements obtained from this thesis is summarized in Fig. 8-1. Through the present study, the proposed AI-based MPC strategy was verified as efficient in real-time optimal control.

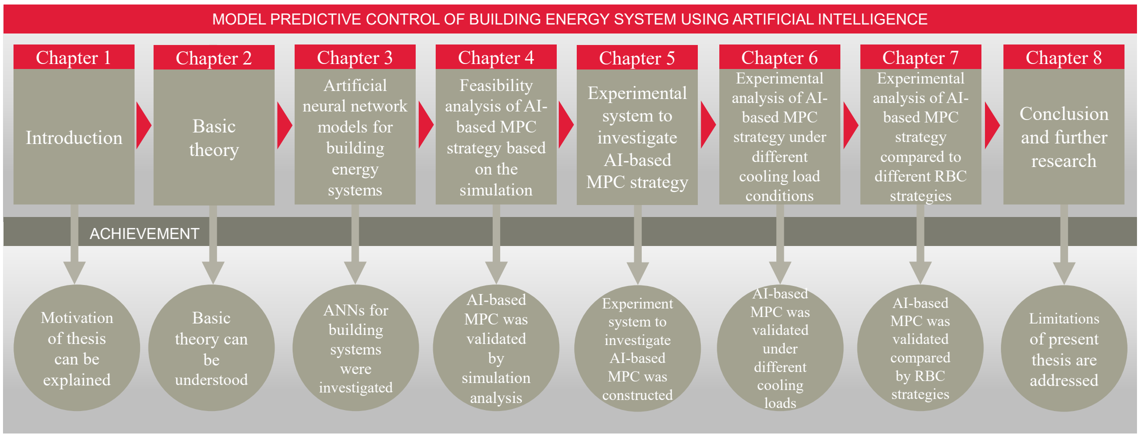

Fig. 8-1. Summary of research flow and achievements.

In Chapter 3, the practicality of the ANN prediction models in building energy systems was investigated. The ANN prediction models of the stratified chilled water TES system and the borehole heat exchangers (BHE) for a ground source heat pump (GSHP) system were constructed based on a case study to determine the optimal input parameters for the training dataset. It was observed that a highly accurate ANN that results in marked reductions in the computational cost can be constructed by combining the appropriate input data parameters. The primary results of the study can be summarized as follows:

- In the case of the TES system, the amount of heat remaining during the current and previous time steps (Q_{TES}^{t-1} and Q_{TES}^{t}) as well as information regarding temperature stratification during the previous time step ($T_1^{t-1}, T_2^{t-1}, \cdots, T_{19}^{t-1}$, and T_{20}^{t-1}) are valid to predict a sending temperature to the secondary side.
- In the case of the BHE, the outlet temperature during the two-steps-prior time step and that during the previous time step (T_{out}^{t-1} and T_{out}^{t-2}) as well as the rate of heat extraction during the current time step and that during the previous time step (q_{BHE}^{t} and q_{BHE}^{t-1}) must be included as

the input parameters to predict the outlet temperature of the BHE.

- Furthermore, the constructed ANN model, which represents the plant system, can be used with the MPC algorithm since its computational load is significantly lower.

In Chapter 4, the feasibility analysis of AI-based MPC strategy with the choice of a virtual office building and target energy systems including TES was conducted based on the simulation. The ANN was utilized to predict the future behavior of the systems and the epsilon constrained differential evolution with random jumping (εDE-RJ) was implemented as an optimization problem solver to minimize operating costs. The primary results of the study can be summarized as follows:

- The MPC reduced the operating costs of the building energy system by 3.4% compared to the RBC during the four-day simulation period, although a sudden increase in occupancy load was conducted intentionally. There was a 1.5% saving in cost when the outdoor temperature was at its highest and this value was 7.2% when outdoor conditions were not extreme.
- The MPC considered an average of 497 s, on a personal laptop (64-bit Windows 10, i7-8700 CPU (3.20 GHz), 8 GB RAM), to find optimal control variables for a prediction horizon 24 h in the future. At first execution, the calculation time was approximately 600 s including the loading time. Furthermore, the constructed ANN model, which represents the plant system, can be used with the MPC algorithm since its computational load is significantly lower.

Although the results from Chapter 4 showed the AI-based MPC strategy was effective, the verification of MPC strategy based on the experimental analysis is necessary considering the following points. First, the training data obtained from the simulation analysis is quantitatively and qualitatively better than actual operational data since experimental data usually includes a noise. Also, in the simulation-based analysis, the system physics such as mechanical characteristics of equipment when the operation starts and stops the driving, the heat loss that occurs when the heat is transferred from the primary side to the secondary side, and the control time delay or the fluctuation that occurs when the heat is supplied from the primary side to the secondary side for the temperature regulation cannot be carefully considered. Therefore, the downscaled mock-up system was devised in order to validate the developed AI-based MPC strategy via experimental analysis. The experimental system for the cooling operation includes a chiller, TES, heat exchangers, and variable-speed pumps. The air-conditioning space was replaced with a water tank, and the cooling load was assigned by an electric immersion heater (in Chapter 5).

In Chapter 6, the developed AI-based MPC strategy was implemented to this experimental system and compared with the RBC strategies that prioritize the TES operation with proportional integral differential (PID) controller under three different patterns of cooling load schedules where the load continues as high, medium, and low during the day. As a result, the proposed AI-based MPC strategy reduced the total operating cost by 9.06–14.56% compared to the RBC strategy. In addition, in the MPC strategy, different operation schedules were observed depending on the scale of the daily cooling load pattern.

In Chapter 7,the effectiveness of the above MPC strategy was further verified by comparing it with two different RBC strategies. Two RBC cases were collected from the experimental system that differed in the cooling operation with TES discharging priority. The case of RBC-1 commences the TES discharging operation as soon as the cooling mode commences. While the RBC-2 case begins the chiller cooling operation by itself, and the TES begins discharging when the electricity price is highest during the occupied hours. Based on the comparative analysis between the MPC strategy and two RBC strategies, the potential of cost savings of AI-based MPC strategy was further verified to reduce the operating costs by 9.7–22.5% compared to the RBC strategies.

Even the simulation and experimental results showed the AI-based MPC strategy showed a high efficiency and optimality in the operation of building energy system with TES to save the operating costs by 3.4–22.5%, the present study has a limitation in the following point of view:

- In the experimental system, the capacity of the heat source equipment was scaled down, the air-conditioning space was simulated by the water tank, and the cooling demand was assigned by the electric immersion heater installed inside the water tank. Therefore, the experimental analysis of the proposed AI-based MPC strategy is required to be verified in actual full-scale buildings with multi-zone conditioning.
- An accelerated experiment that shortens the day from 24 hours to 4 hours was conducted. In designing of the MPC controller, it is important to set the parameter of prediction time horizon and the control time horizon carefully. However, such a design parameter of the prediction horizon and the control time horizon was not investigated in this study since the experiment was conducted with an accelerated scale.
- When the developed AI-based MPC was implemented by the experimental system, the centralized MPC was adopted as shown in the figure below. Firstly, the setpoint of the flow rate which was obtained by the optimizer was assigned to the internal PID controller of the inverter, then the frequency of the inverter was controlled to operate the system with the optimized supplying flow rate. One of the key advantages of this kind of MPC implementation is that it is relatively easy to introduce the MPC controller to the existing system because it can promote the optimal operation by simply linking the main PC with the system. However, since the control signal must go through two stages, it can be relatively unreasonable. If the control process is needed to be more simplified, the direct control of the frequency of the inverter can

also be adopted by modeling the relationship between the flow rate of each water loop and the frequency of the inverter.

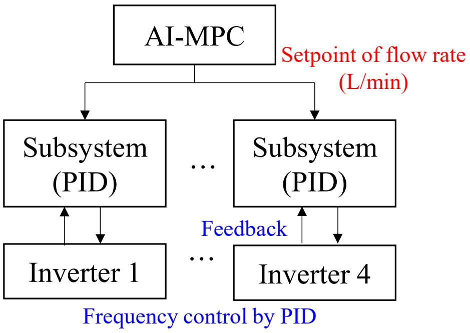

Fig. 8-2. Centralized MPC adopted for the experimental implementation.

- The developed AI-based MPC can be expected to be utilized to solve various control problems. For instance, the control problem to determine the optimal setpoint for producing the chilled water from the heat source, to regulate the multi-zone not only the single zone, to simply decide the best operation mode of the TES system at the moment, and so on. However, this study only tested the developed method to determine the optimal flow rates in each water loop to regulate the single zone temperature and thus the additional verification in a various condition can be further studied.
- Further, in the present thesis, the AI-based MPC strategy was compared only with the RBC strategies that prioritize the TES operation. It is necessary to compare the proposed AI-based MPC strategy with various operation strategies such as an advanced operation strategies based on the experience of building operators.
- Moreover, future disturbances that affect the implementation of the MPC strategy for building energy management such as occupant-behavior-related disturbances, and time-variant electricity pricing disturbances were not considered and assumed as known in advance in this study.

Appendix

Appendix 1. Results of model evaluation after training runs for all cases of stratified chilled water TES system.

Case	Inputs	Number of hidden layers	Number of hidden neurons	R^2	RMSE (°C)	CVRMSE (%)
TES 1	3	1	10	0.9973	0.2294	2.37
			20	0.9971	0.2337	2.41
			30	0.9966	0.2560	2.63
		2	10–10	0.9987	0.1545	1.59
			20–20	0.9999	0.0348	0.35
			30–30	0.9994	0.0997	1.02
TES 2	4	1	10	0.9997	0.0673	0.69
			20	0.9988	0.1488	1.53
			30	0.9992	0.1181	1.21
		2	10–10	0.9999	0.0341	0.35
			20–20	0.9999	0.0386	0.39
			30–30	0.9999	0.0243	0.25
TES 3	21	1	10	0.9997	0.0629	0.64
			20	0.9990	0.1338	1.37
			30	0.9998	0.0531	0.54
		2	10–10	0.9999	0.0264	0.27
			20–20	0.9999	0.0265	0.27
			30–30	0.9999	0.0284	0.29
TES 4	4	1	10	0.9997	0.0741	0.76
			20	0.9993	0.1125	1.16
			30	0.9998	0.0471	0.48
		2	10–10	0.9999	0.0318	0.32
			20–20	0.9999	0.0205	0.21
			30–30	0.9996	0.0870	0.89
TES 5	5	1	10	0.9997	0.0651	0.67
			20	0.9998	0.0532	0.54
			30	0.9998	0.0473	0.48
		2	10–10	0.9999	0.0277	0.28
			20–20	0.9999	0.0238	0.24
			30–30	0.9999	0.0250	0.25
TES 6	22	1	10	0.9987	0.1545	1.59
			20	0.9999	0.0348	0.35
			30	0.9994	0.0997	1.02
		2	10–10	0.9999	0.0234	0.24
			20–20	0.9999	0.0224	0.23
			30–30	0.9999	0.0204	0.21

Appendix 2. Results of model evaluation after training runs for all cases of BHE for GSHP system.

Case	Inputs	Number of hidden layers	Number of hidden neurons	R2	RMSE (°C)	CVRMSE (%)
BHE 1	4	1	10	0.9999	0.0071	0.05
			20	0.9999	0.0054	0.04
			30	0.9999	0.0054	0.04
		2	10–10	0.9999	0.0054	0.04
			20–20	0.9999	0.0054	0.04
			30–30	0.9999	0.0053	0.04
BHE 2	2	1	10	0.9917	0.0934	0.78
			20	0.9914	0.0939	0.78
			30	0.9912	0.0931	0.77
		2	10–10	0.9916	0.0935	0.78
			20–20	0.9916	0.0930	0.77
			30–30	0.9912	0.0905	0.75
BHE 3	3	1	10	0.9937	0.0811	0.67
			20	0.9935	0.0814	0.68
			30	0.9934	0.0817	0.68
		2	10–10	0.9939	0.0781	0.65
			20–20	0.9936	0.0801	0.66
			30–30	0.9933	0.0817	0.68
BHE 4	3	1	10	0.9952	0.0700	0.58
			20	0.9950	0.0708	0.59
			30	0.9944	0.0730	0.60
		2	10–10	0.9952	0.0717	0.59
			20–20	0.9953	0.0703	0.58
			30–30	0.9953	0.0693	0.57
BHE 5	3	1	10	0.9980	0.0429	0.35
			20	0.9983	0.0410	0.34
			30	0.9985	0.0384	0.32
		2	10–10	0.9985	0.0386	0.32
			20–20	0.9986	0.0368	0.30
			30–30	0.9983	0.0408	0.34
BHE 6	4	1	10	0.9988	0.0341	0.28
			20	0.9990	0.0327	0.27
			30	0.9988	0.0329	0.27
		2	10–10	0.9989	0.3242	0.27
			20–20	0.9993	0.0261	0.21
			30–30	0.9992	0.0290	0.24

BHE 7	2	1	10	0.9534	0.2181	1.82
			20	0.9521	0.2262	1.88
			30	0.9466	0.2323	1.94
		2	10–10	0.9495	0.2316	1.93
			20–20	0.9502	0.2245	1.87
			30–30	0.9485	0.2300	1.91
BHE 8	4	1	10	0.9999	0.0067	0.05
			20	0.9999	0.0070	0.05
			30	0.9999	0.0064	0.05
		2	10–10	0.9999	0.0065	0.05
			20–20	0.9999	0.0063	0.05
			30–30	0.9999	0.0063	0.05

Appendix 3. Front panel of the LabVIEW environment to display the system status of the experimental system for the measurement and control.

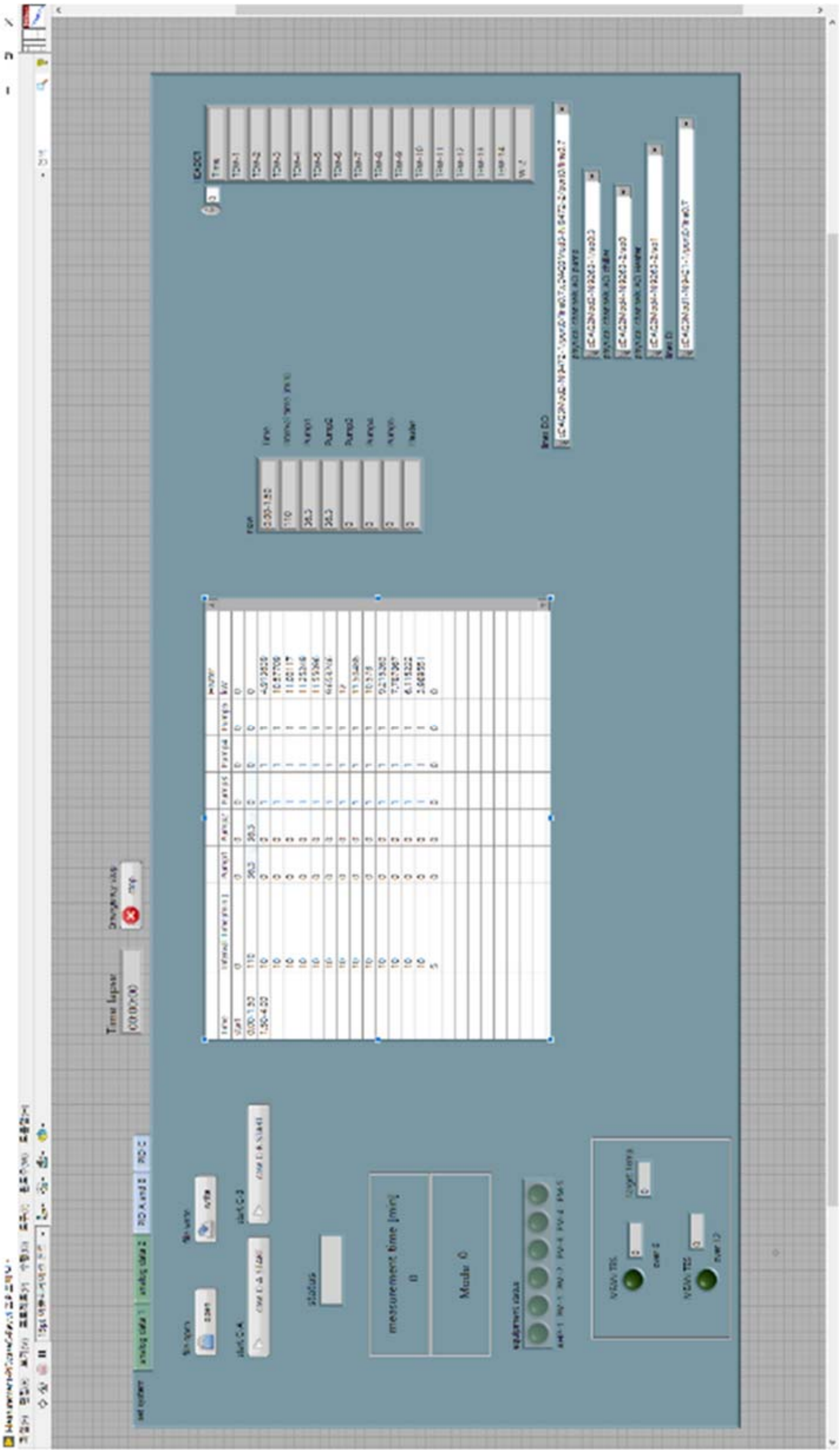

Appendix 4. Front panel of the LabVIEW environment for monitoring the temperatures from the experimental system.

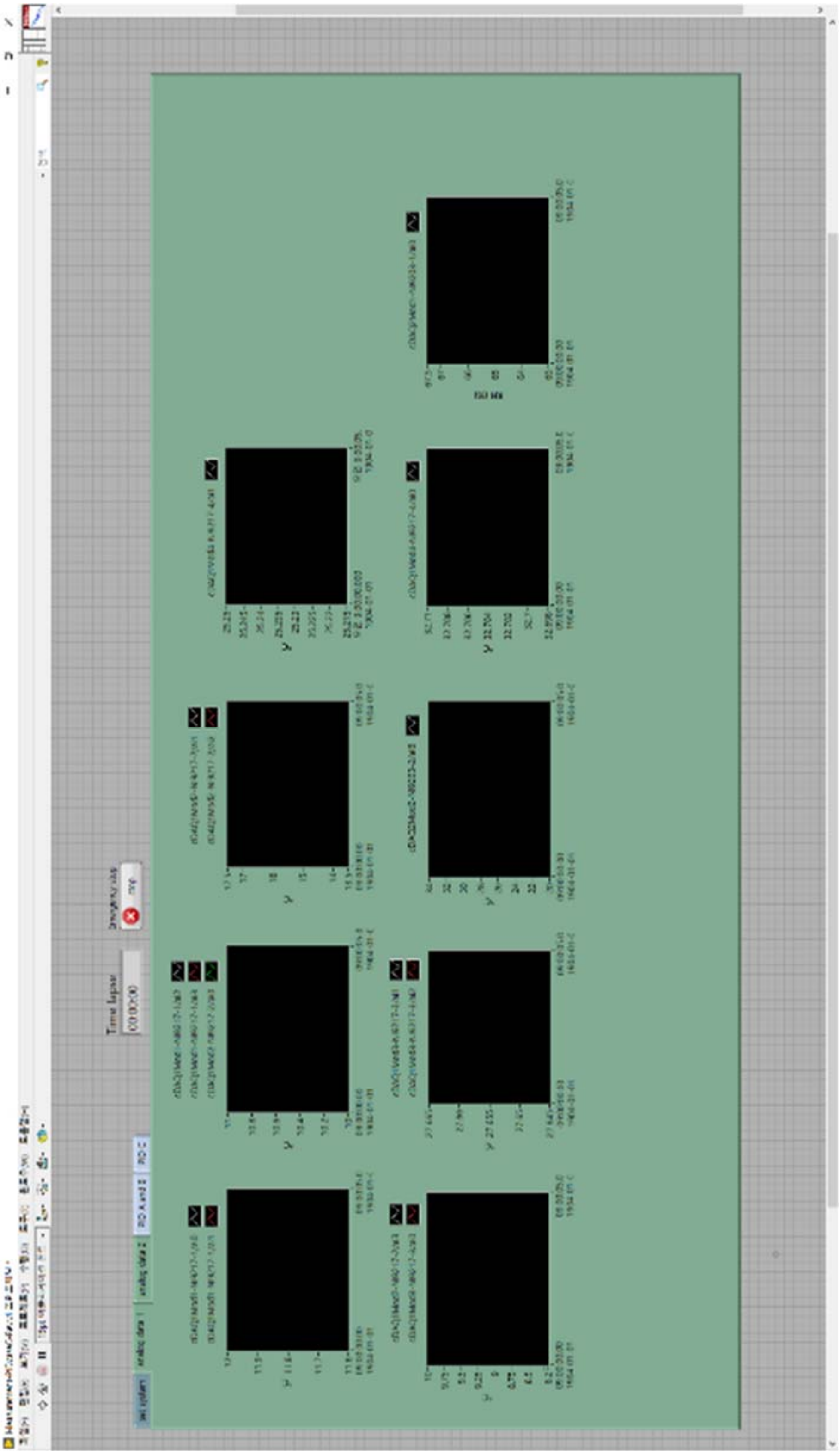

Appendix 5. Front panel of the LabVIEW environment for monitoring the flow rates and power consumption from the experimental system.

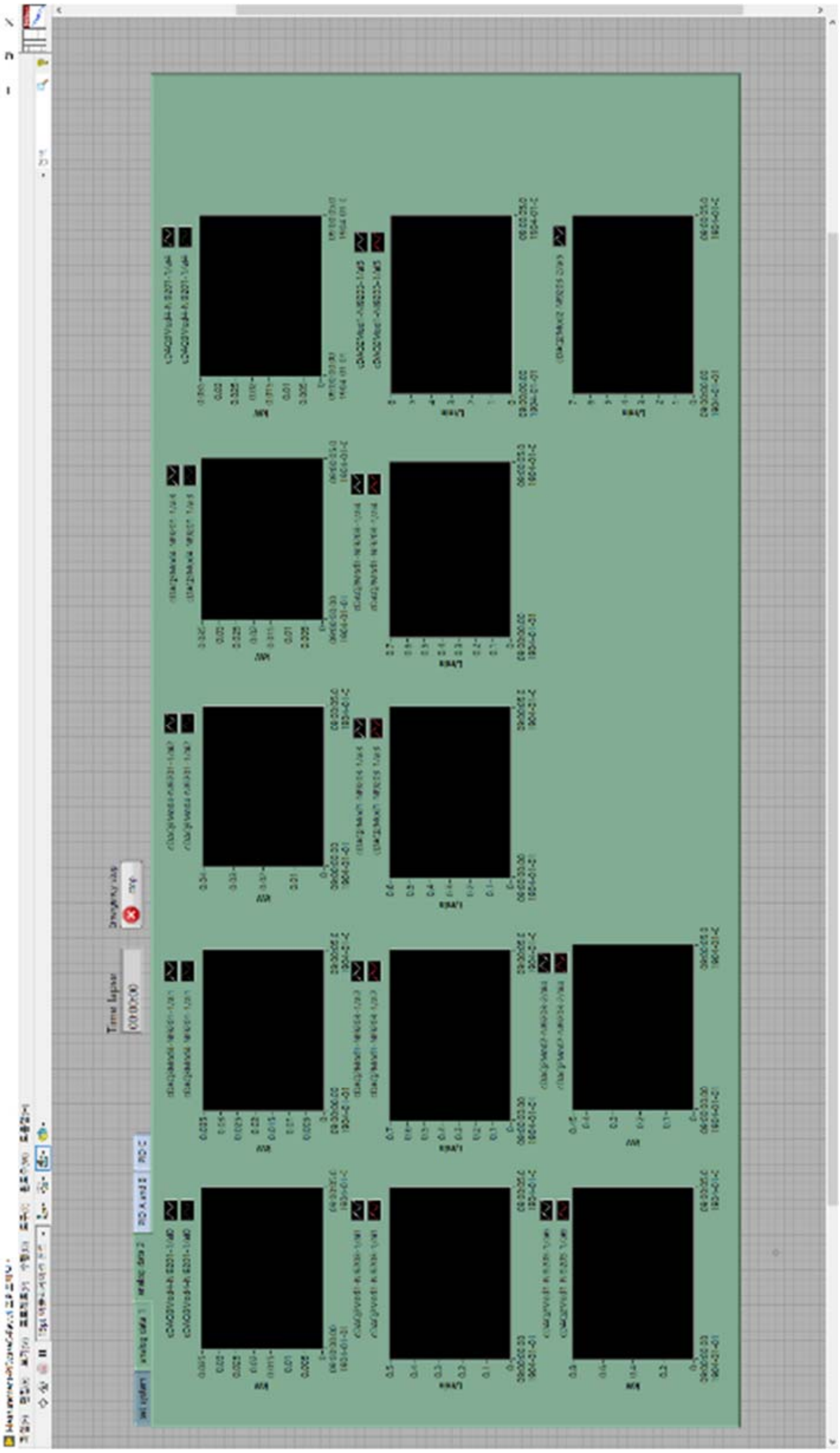

Appendix 6. Front panel of the LabVIEW environment to display the PID controller to control the pumps (P-3, P-4 in Fig. 5-2) for TES discharging operation.

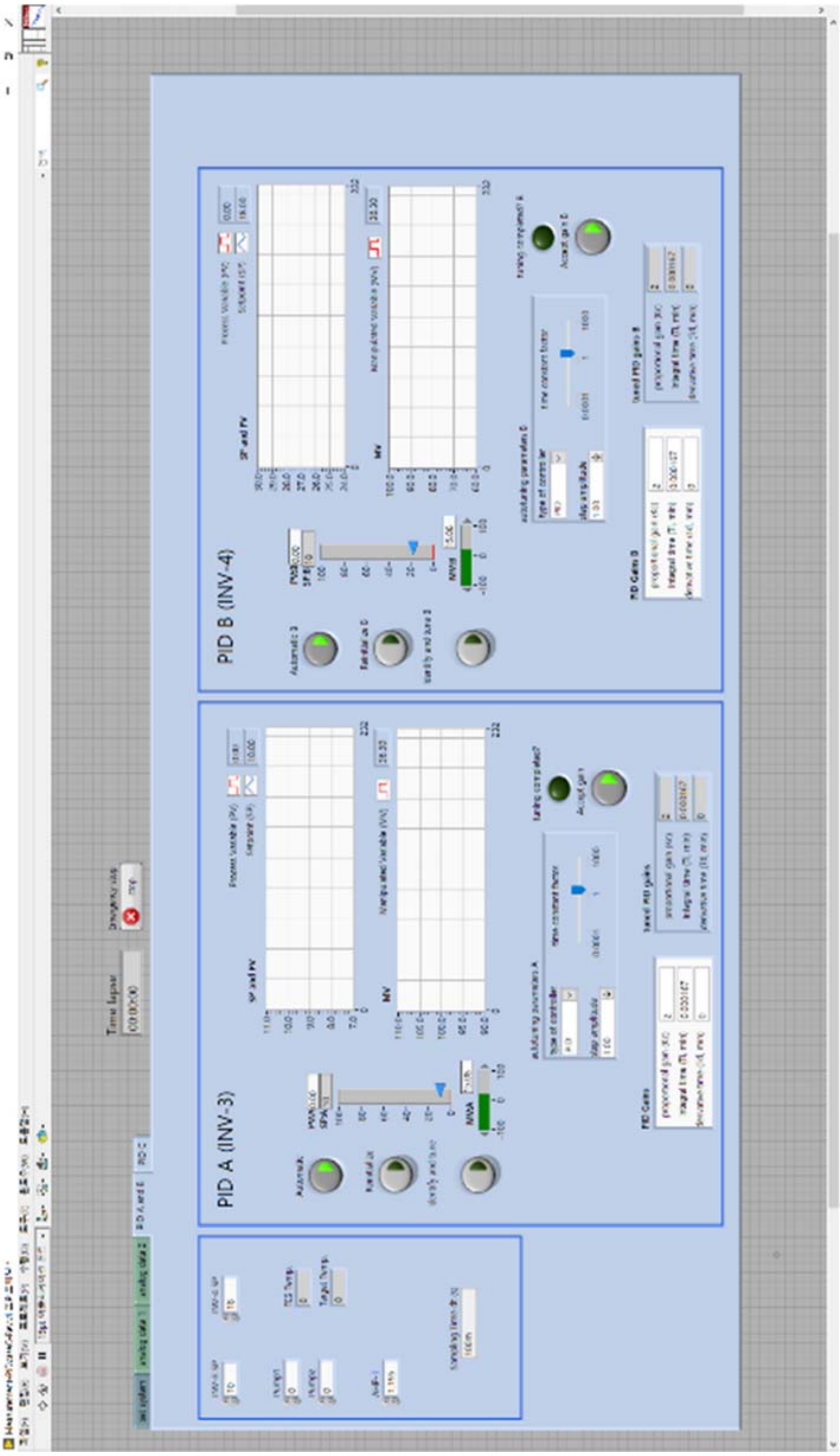

Appendix 7. Front panel of the LabVIEW environment to display the PID controller to control the pump (P-1 in Fig. 5-2) for cooling operation of the chiller.

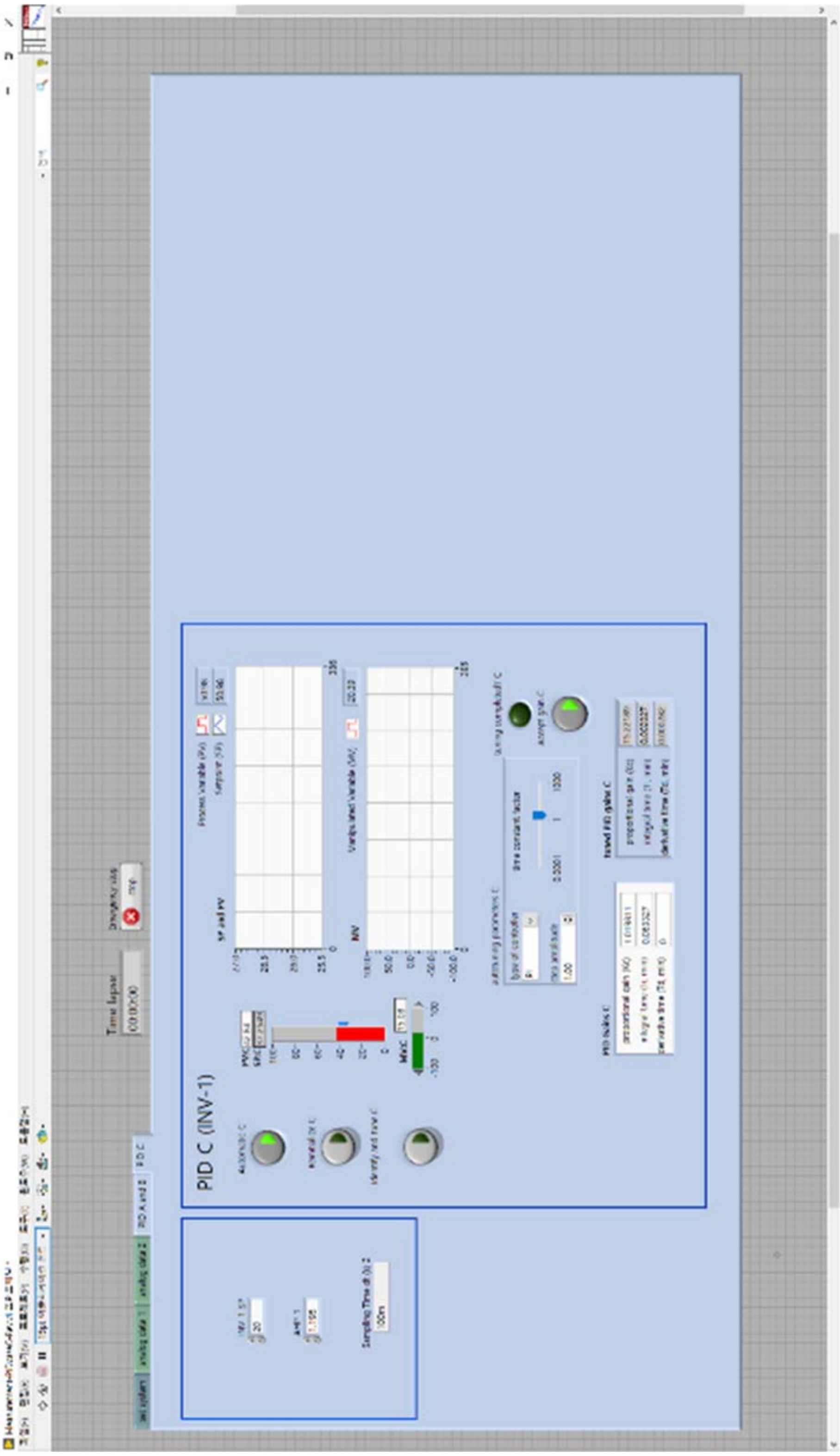

Appendix 8. Block diagram of the LabVIEW environment to initialize the status of the experimental system and get ready to measure all data.

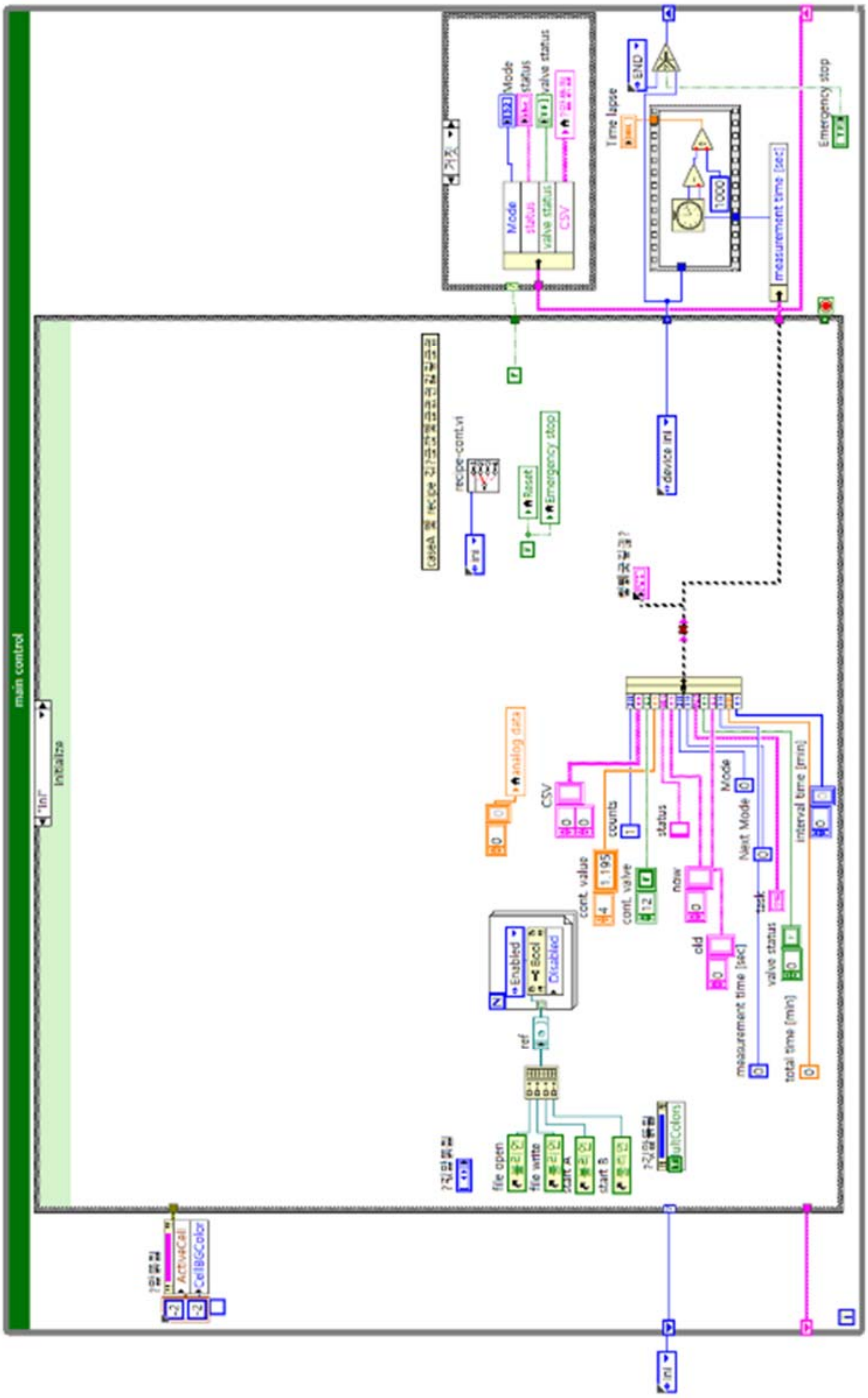

Appendix 9. Block diagram of the LabVIEW environment to initialize the status of the experimental system (all the equipment to be off and 2-way valves to be closed).

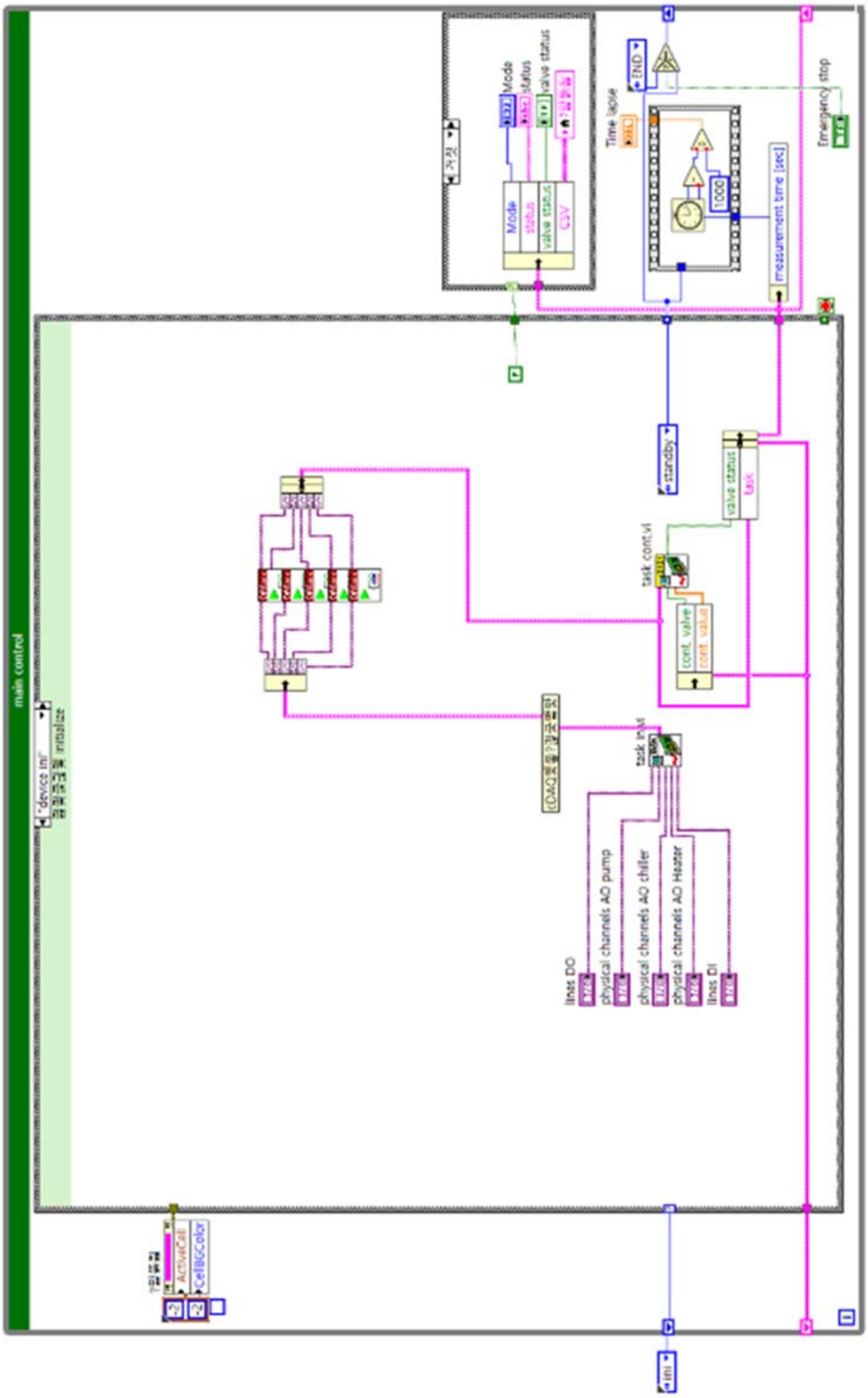

Appendix 10. Block diagram of the LabVIEW environment to initialize the status of the experimental system.

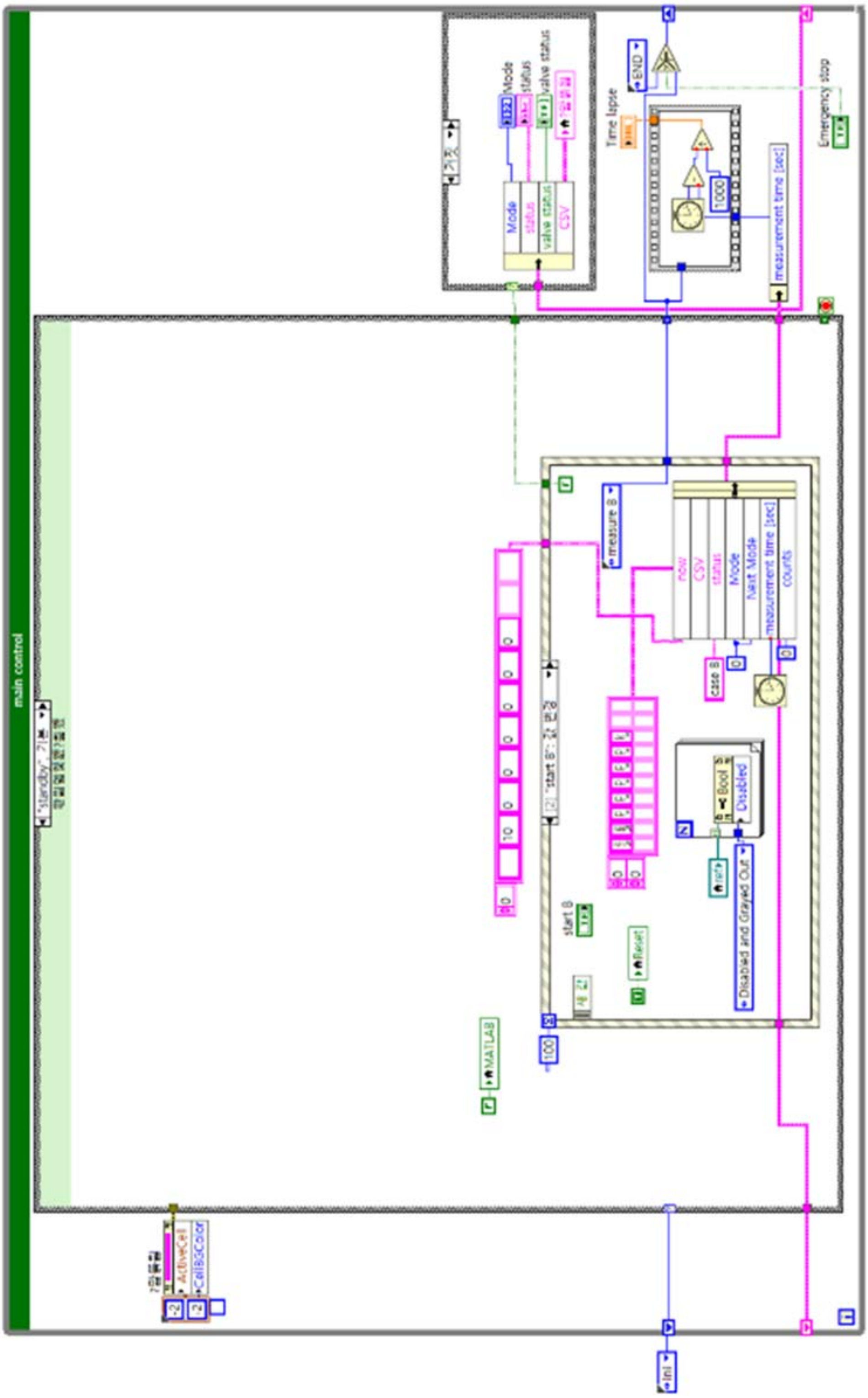

Appendix 11. Block diagram of the LabVIEW environment to manually measure and control the status of the experimental system.

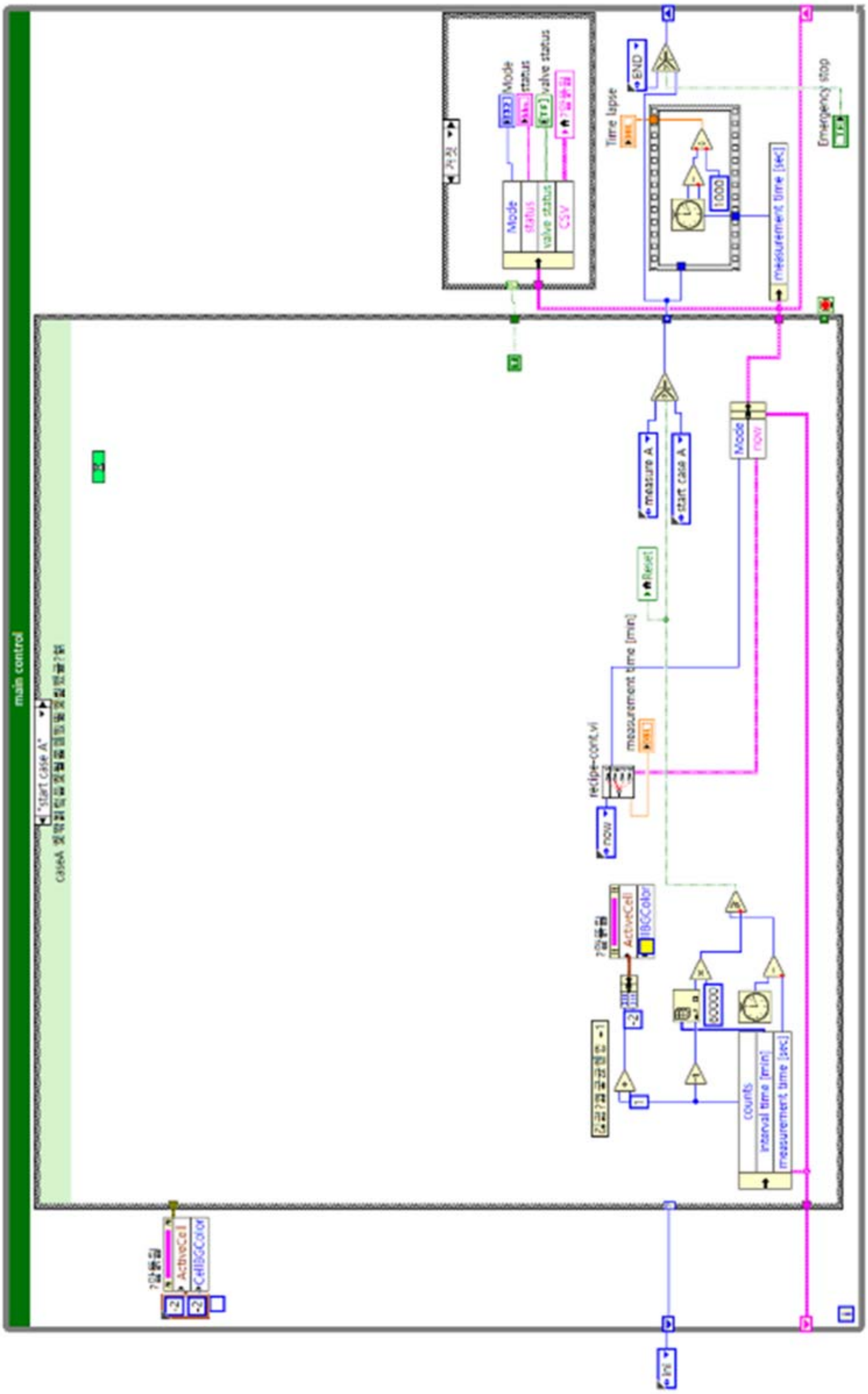

Appendix 12. Block diagram of the LabVIEW environment to interconnect the MATLAB to obtain the optimization results from MPC and automatically measure and control the status of the experimental system.

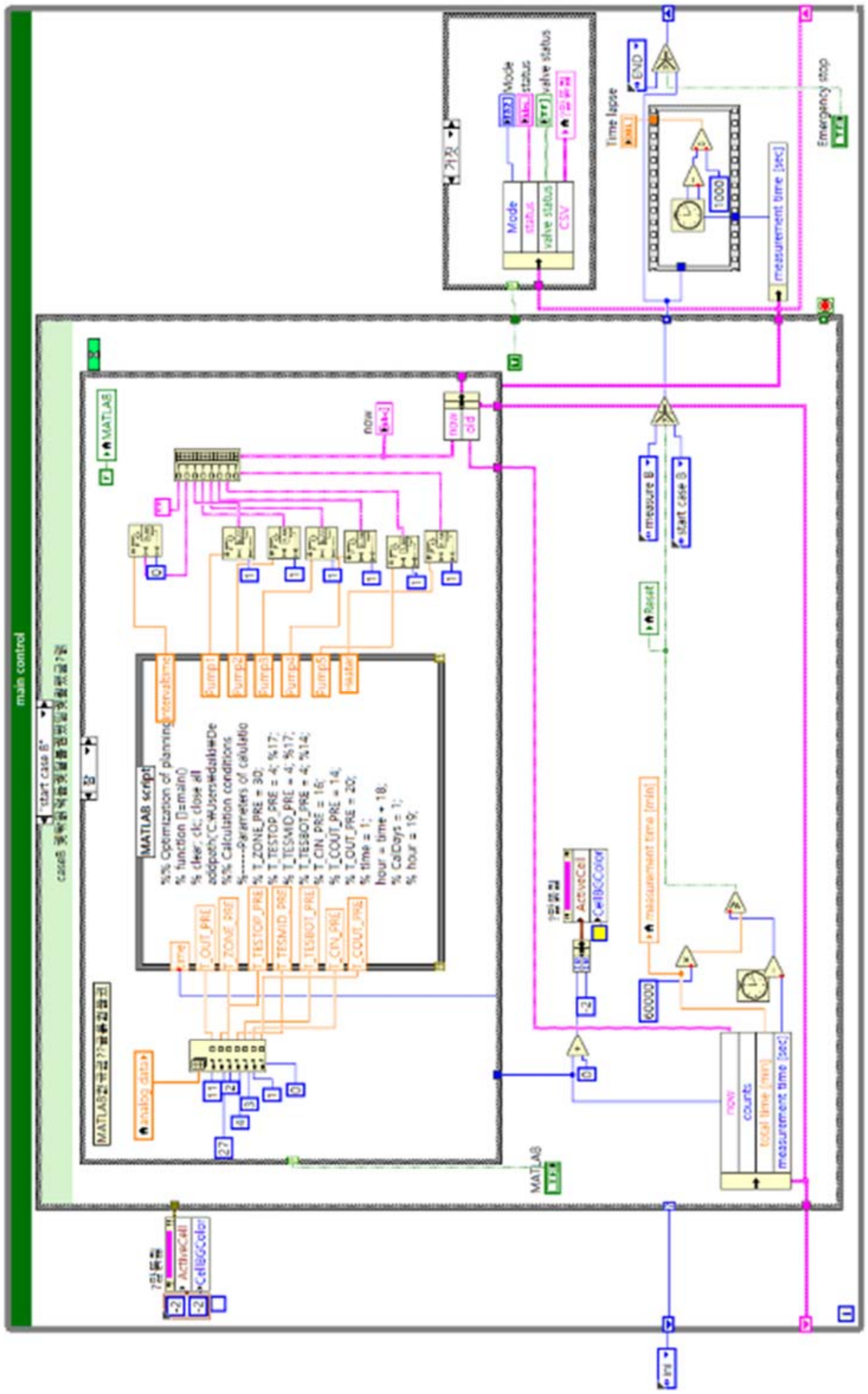

```
%% Optimization of planning
% function []=main()
% clear; clc; close all
addpath('C:₩Users₩dalki₩De
%% Calculation conditions
%------Parameters of calulatio
% T_ZONE_PRE = 30;
% T_TESTOP_PRE = 4; %17;
% T_TESMID_PRE = 4; %17;
% T_TESBOT_PRE = 4; %14;
% T_CIN_PRE = 16;
% T_COUT_PRE = 14;
% T_OUT_PRE = 20;
% time = 1;
hour = time + 18;
% CalDays = 1;
% hour = 19;
```

Appendix 13. Block diagram of the LabVIEW environment to consecutively measure the status of the experimental system.

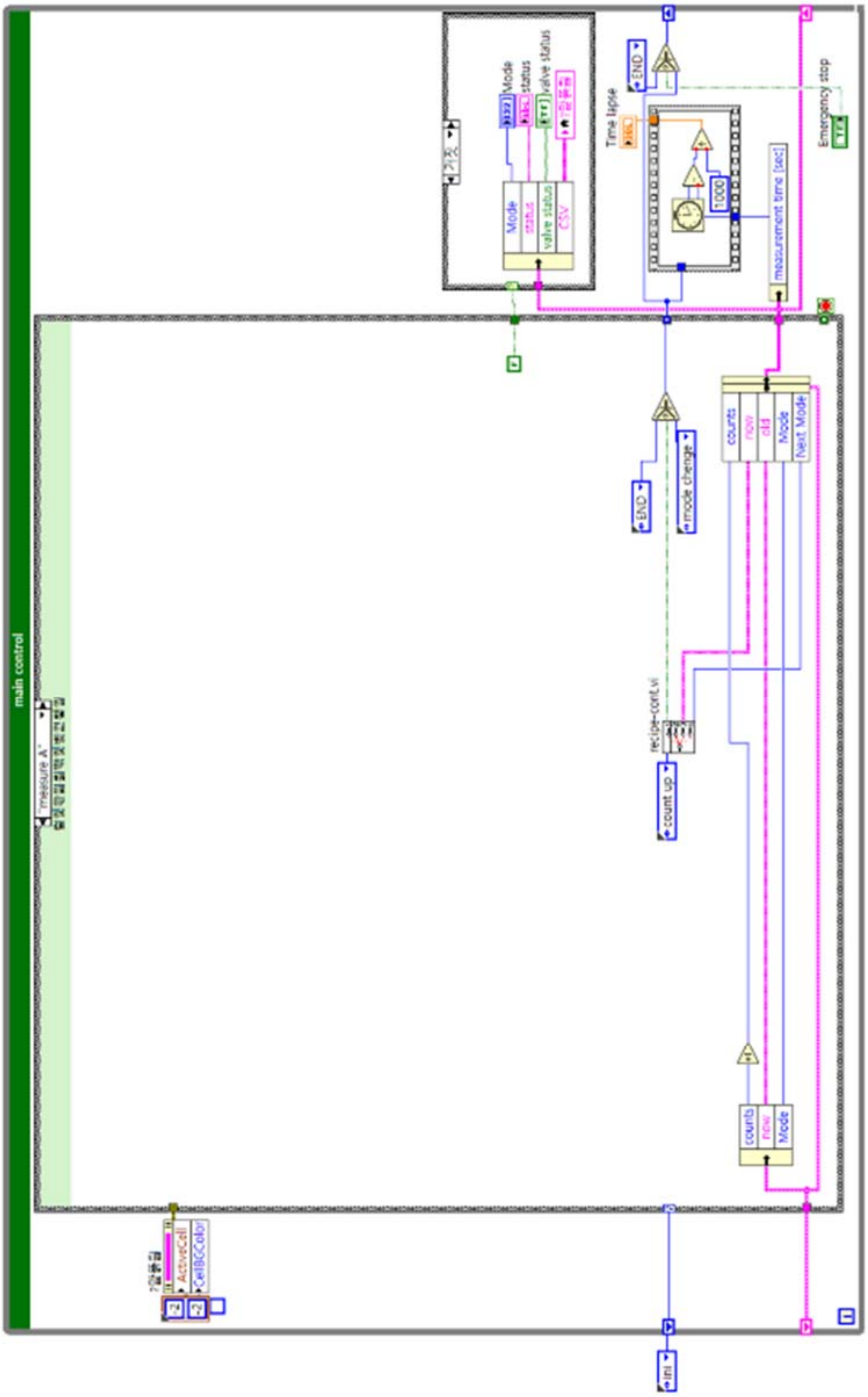

Appendix 14. Block diagram of the LabVIEW environment to consecutively measure the status of the experimental system when it was operated by MPC controller.

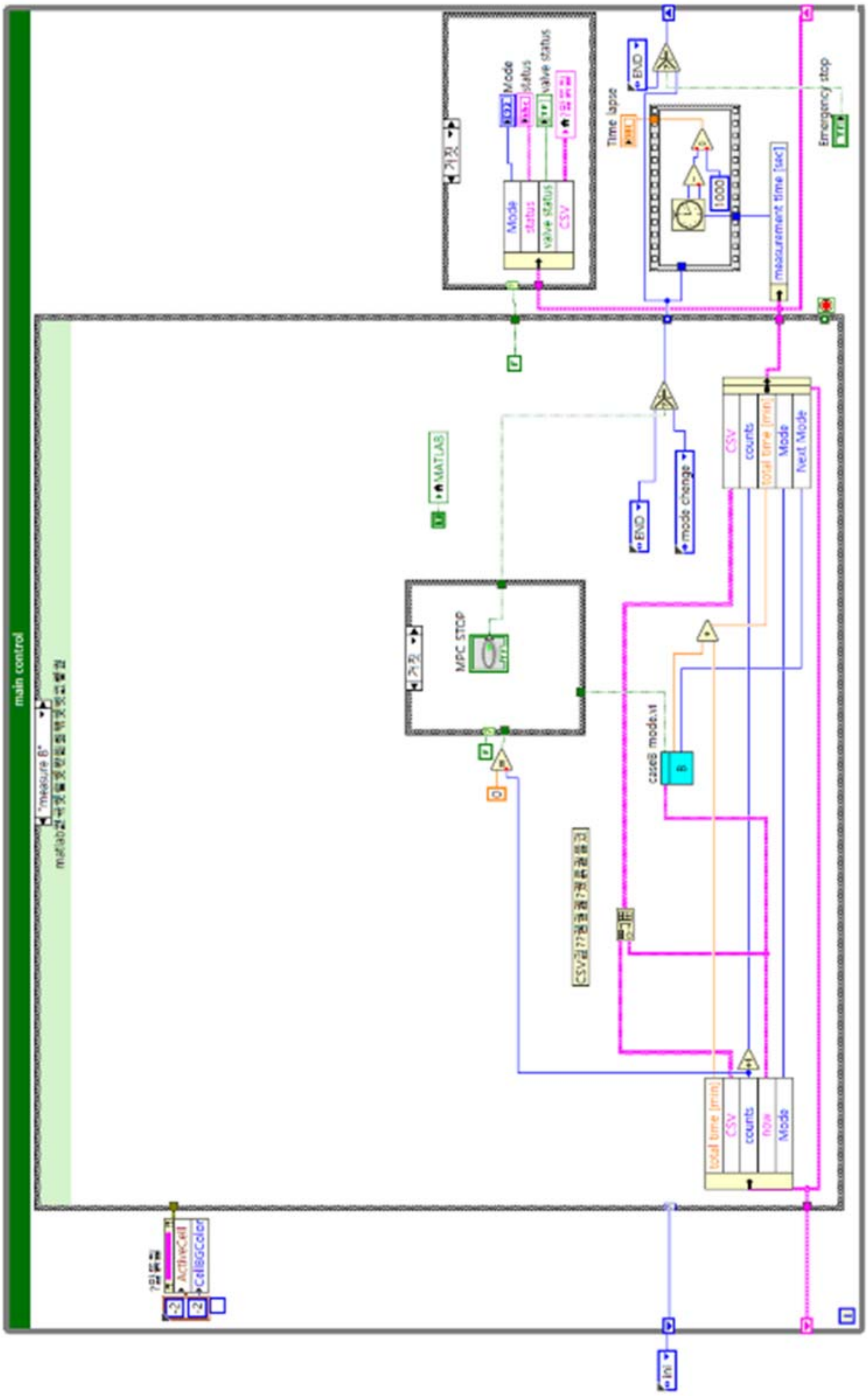

Appendix 15. Block diagram of the LabVIEW environment to automatically control the on-off status and open-close status of the equipment and switch the operation of the experimental system.

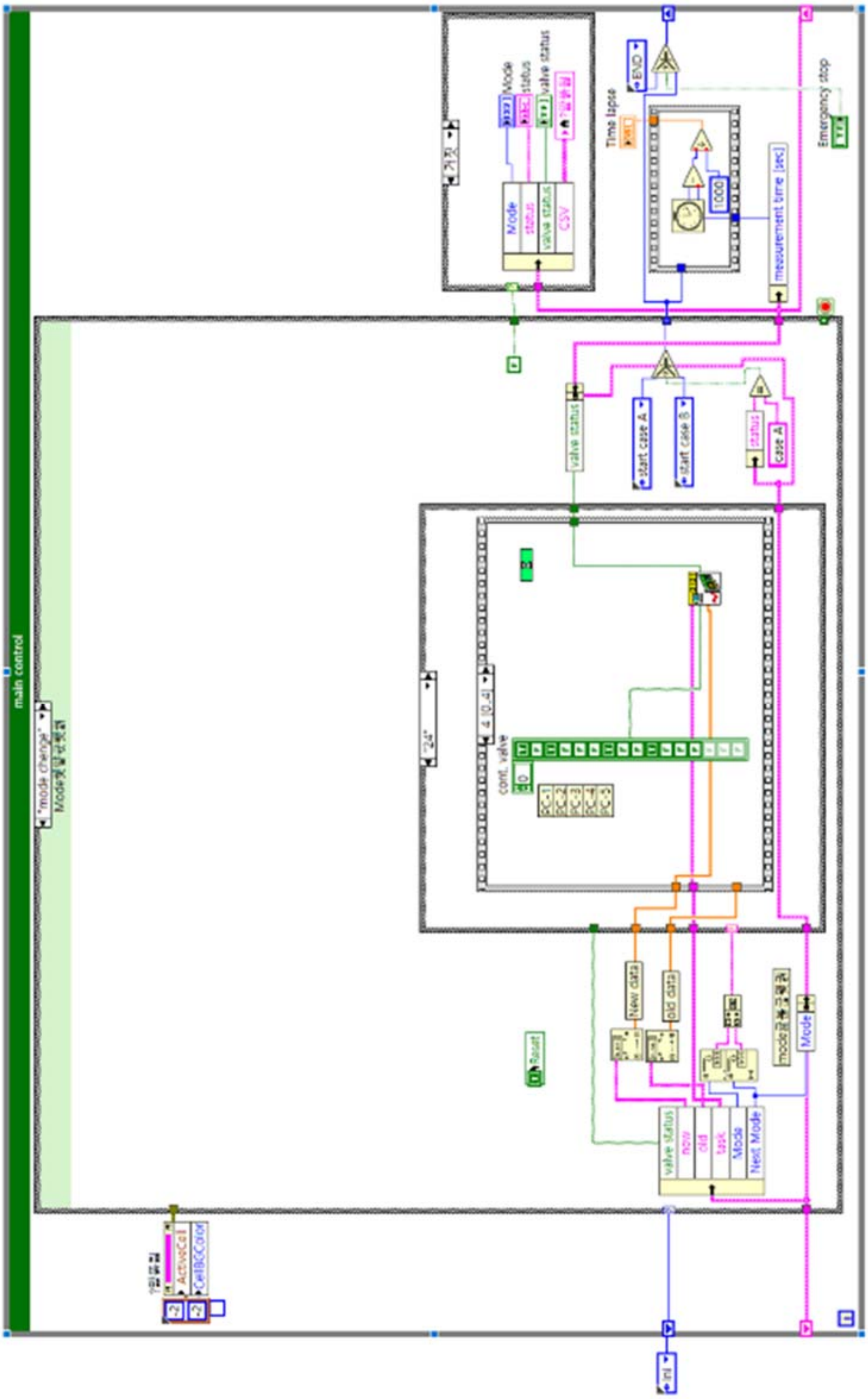

Appendix 16. Block diagram of the LabVIEW environment to stop the operation of the experimental system.

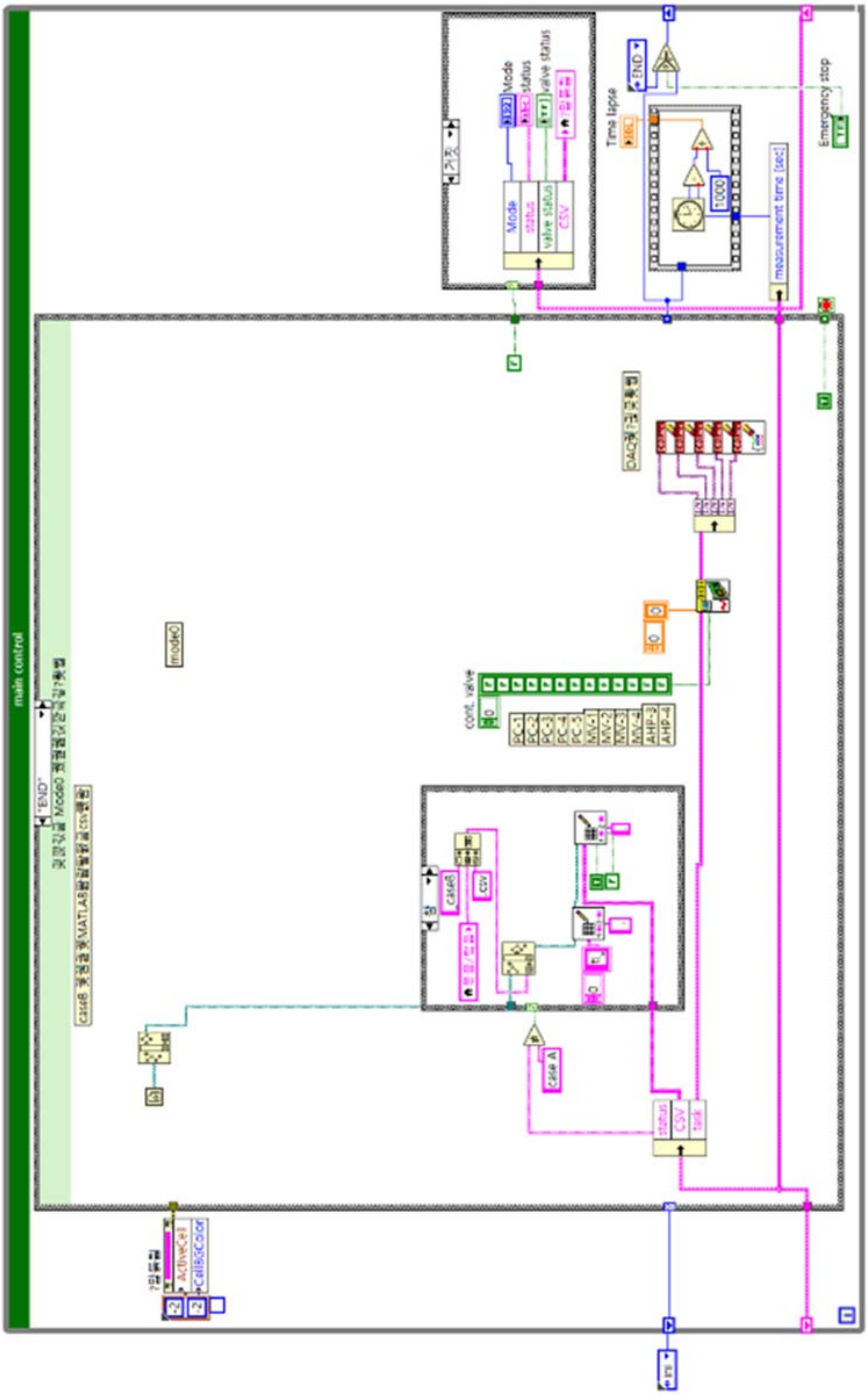

Appendix 17. Block diagram of the LabVIEW environment to connect the DAQ system and LabVIEW software.

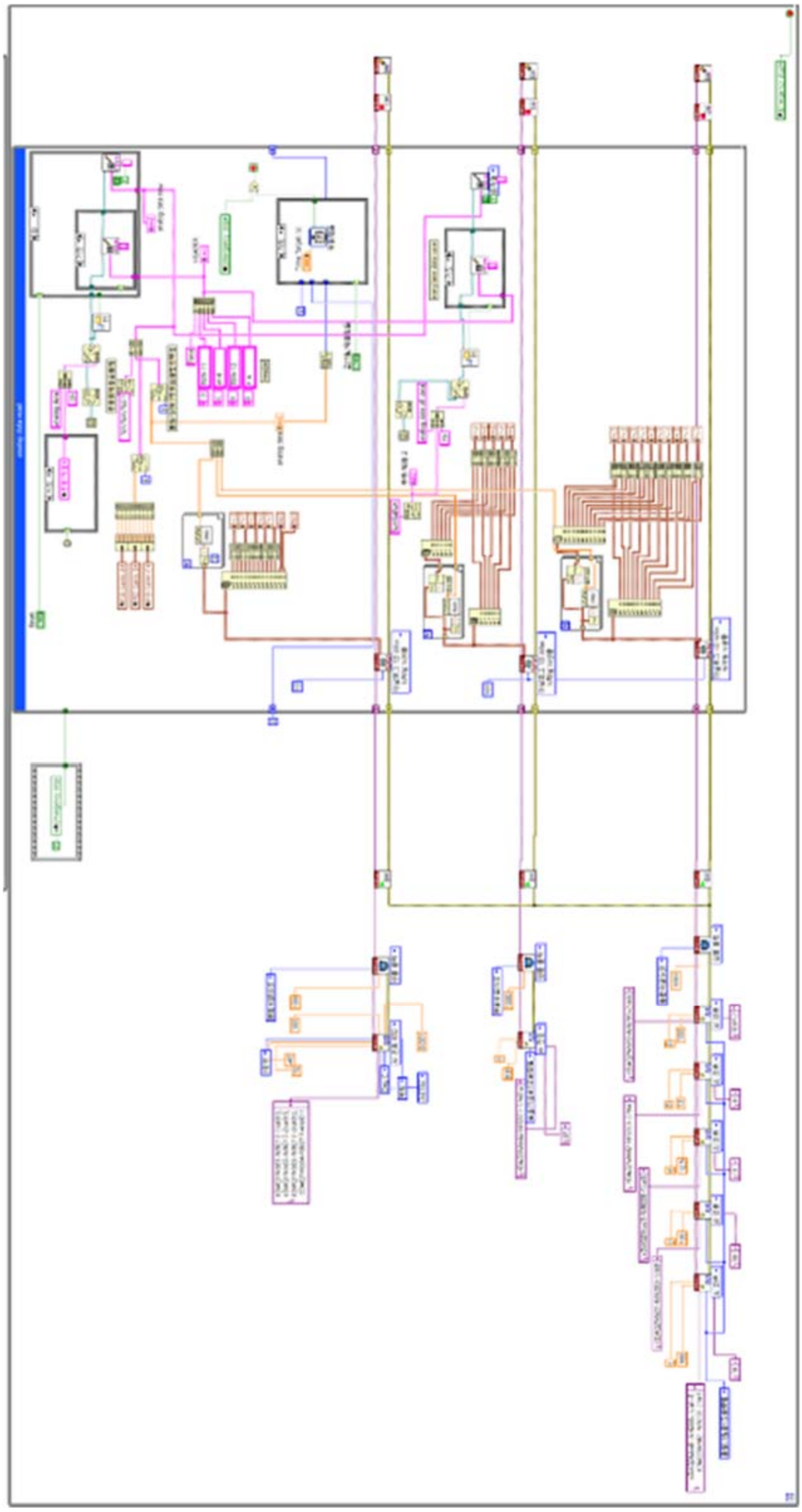

Appendix 18. Block diagram of the LabVIEW environment to program PID controllers to control the pumps (P-3, P-4 in Fig. 5-2) for TES discharging operation.

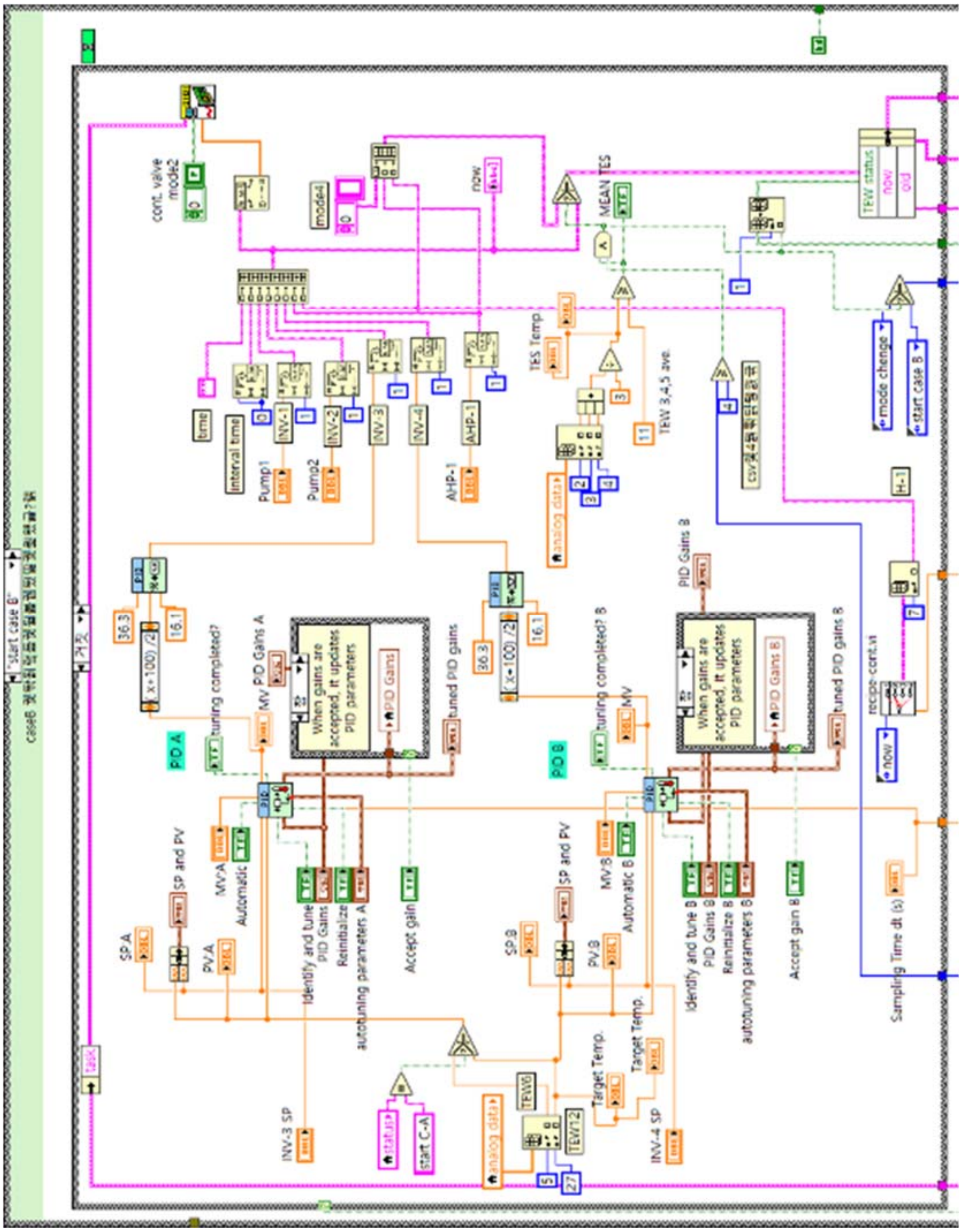

Appendix 19. Block diagram of the LabVIEW environment to program PID controllers to control the pump (P-1 in Fig. 5-2) for cooling operation of the chiller.

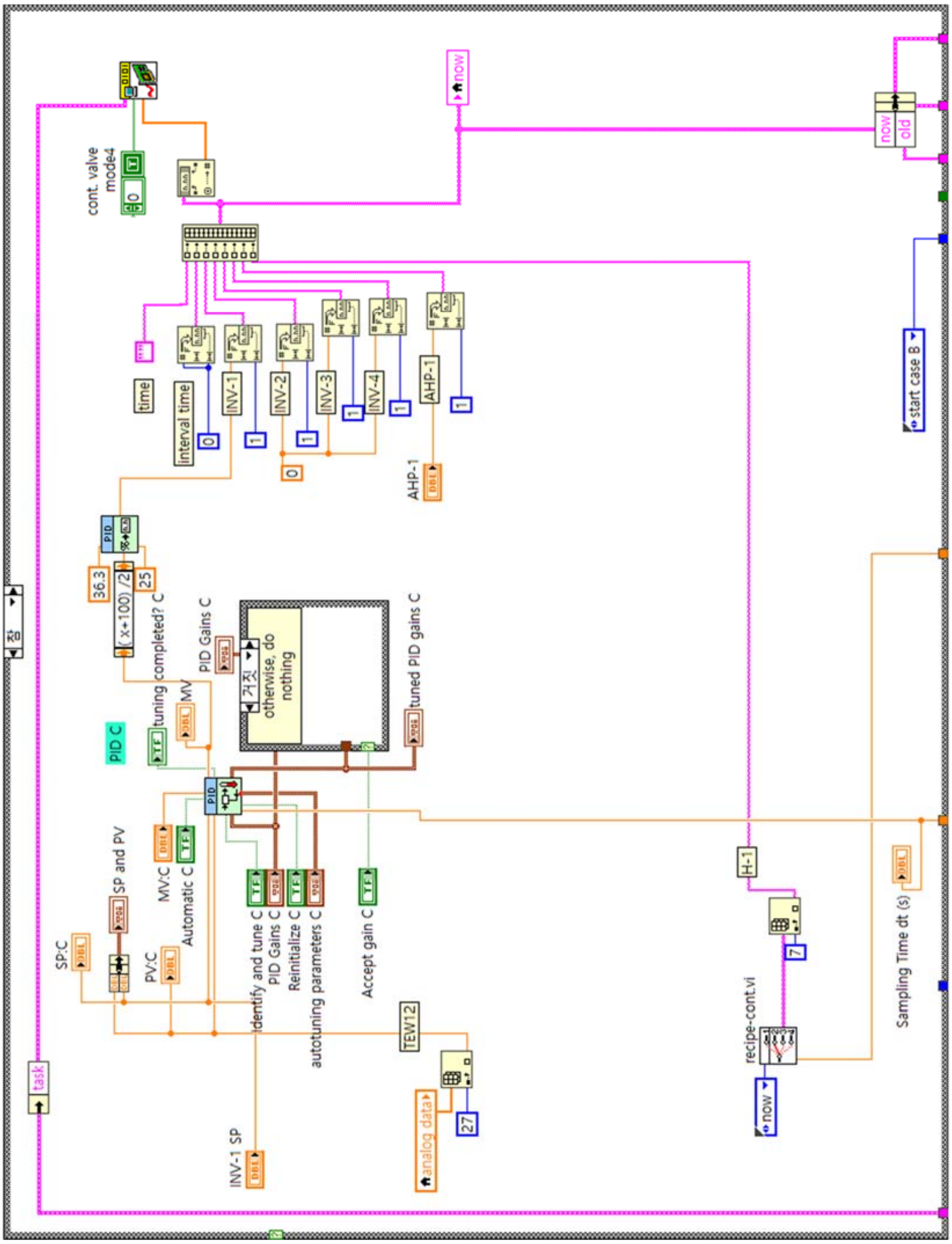

Reference

[1] International Energy Agency (IEA), Technology Roadmap: Energy-Efficient Buildings: Heating and Cooling Equipment, (2012).

[2] L. Pérez-Lombard, J. Ortiz, C. Pout, A review on buildings energy consumption information, Energy Build. 40 (2008) 394–398. https://doi.org/10.1016/j.enbuild.2007.03.007.

[3] Energy Information Administration (EIA), Commercial Buildings Energy Consumption Survey (CBECS) User's Guide to the 2012 CBECS Public Use Microdata File, 2016 (2016). https://www.eia.gov/consumption/commercial/data/2012/index.cfm?view=microdata.

[4] Z. Yu, G. Huang, F. Haghighat, H. Li, G. Zhang, Control strategies for integration of thermal energy storage into buildings: State-of-the-art review, Energy Build. 106 (2015) 203–215. https://doi.org/10.1016/j.enbuild.2015.05.038.

[5] J. Drgoňa, J. Arroyo, I. Cupeiro Figueroa, D. Blum, K. Arendt, D. Kim, E.P. Ollé, J. Oravec, M. Wetter, D.L. Vrabie, L. Helsen, All you need to know about model predictive control for buildings, Annu. Rev. Control. 50 (2020) 190–232. https://doi.org/10.1016/j.arcontrol.2020.09.001.

[6] A. Afram, F. Janabi-Sharifi, Theory and applications of HVAC control systems - A review of model predictive control (MPC), Build. Environ. 72 (2014) 343–355. https://doi.org/10.1016/j.buildenv.2013.11.016.

[7] M. Killian, M. Kozek, Ten questions concerning model predictive control for energy efficient buildings, Build. Environ. 105 (2016) 403–412. https://doi.org/10.1016/j.buildenv.2016.05.034.

[8] G.A. Benndorf, D. Wystrcil, N. Réhault, Energy performance optimization in buildings: A review on semantic interoperability, fault detection, and predictive control, Appl. Phys. Rev. 5 (2018). https://doi.org/10.1063/1.5053110.

[9] R. Kwadzogah, M. Zhou, S. Li, Model predictive control for HVAC systems - A review, in: 2013 IEEE Int. Conf. Autom. Sci. Eng., IEEE, 2013: pp. 442–447. https://doi.org/10.1109/CoASE.2013.6654072.

[10] P. Rockett, E.A. Hathway, Model-predictive control for non-domestic buildings: a critical review and prospects, Build. Res. Inf. 45 (2017) 556–571. https://doi.org/10.1080/09613218.2016.1139885.

[11] D. Mariano-Hernández, L. Hernández-Callejo, A. Zorita-Lamadrid, O. Duque-Pérez, F. Santos García, A review of strategies for building energy management system: Model predictive control, demand side management, optimization, and fault detect & diagnosis, J. Build. Eng. 33 (2021) 101692. https://doi.org/10.1016/j.jobe.2020.101692.

[12] D. Westphalen, S. Koszalinski, Energy Consumption Characteristics of Commercial Building HVAC Systems. Volume II: Thermal Distribution, Auxiliary Equipment, and Ventilation, 1999. https://doi.org/DE-AC01-96CE23798.

[13] W. Goetzler, R. Shandross, J. Young, O. Petritchenko, D. Ringo, S. McClive, Energy Savings Potential and RD&D Opportunities for Commercial Building HVAC Systems U.S. DOE, Burlington, MA (United States), 2017. https://www.energy.gov/sites/prod/files/2017/12/f46/bto-DOE-Comm-HVAC-Report-12-21-17.pdf.

[14] G. Serale, M. Fiorentini, A. Capozzoli, D. Bernardini, A. Bemporad, Model Predictive Control (MPC) for enhancing building and HVAC system energy efficiency: Problem formulation, applications and opportunities, Energies. 11 (2018) 631. https://doi.org/10.3390/en11030631.

[15] J. Cigler, S. Prívara, Z. Váňa, E. Žáčeková, L. Ferkl, Optimization of predicted mean vote index within model predictive control framework: Computationally tractable solution, Energy Build. 52 (2012) 39–49. https://doi.org/10.1016/j.enbuild.2012.05.022.

[16] P.M. Ferreira, A.E. Ruano, S. Silva, E.Z.E. Conceição, Neural networks based predictive control for thermal comfort and energy savings in public buildings, Energy Build. 55 (2012) 238–251. https://doi.org/10.1016/j.enbuild.2012.08.002.

[17] J. Široký, F. Oldewurtel, J. Cigler, S. Prívara, Experimental analysis of model predictive control for an energy efficient building heating system, Appl. Energy. 88 (2011) 3079–3087. https://doi.org/10.1016/j.apenergy.2011.03.009.

[18] J. Rehrl, M. Horn, Temperature control for HVAC systems based on exact linearization and model predictive control, Proc. IEEE Int. Conf. Control Appl. (2011) 1119–1124. https://doi.org/10.1109/CCA.2011.6044437.

[19] Y. Ma, F. Borrelli, B. Hencey, A. Packard, S. Bortoff, Model predictive control of thermal energy storage in building cooling systems, Proc. IEEE Conf. Decis. Control. (2009) 392–397. https://doi.org/10.1109/CDC.2009.5400677.

[20] Y. Ma, A. Kelman, A. Daly, F. Borrelli, Predictive Control for Energy Efficient Buildings with Thermal Storage, IEEE Control Syst. 32 (2012) 44–64. http://ieeexplore.ieee.org/lpdocs/epic03/wrapper.htm?arnumber=6153586.

[21] M. Fiorentini, J. Wall, Z. Ma, J.H. Braslavsky, P. Cooper, Hybrid model predictive control of a residential HVAC system with on-site thermal energy generation and storage, Appl. Energy. 187 (2017) 465–479. https://doi.org/10.1016/j.apenergy.2016.11.041.

[22] J. Richalet, A. Rault, J.L. Testud, J. Papon, Model predictive heuristic control, Automatica. 14 (1978) 413–428. https://doi.org/10.1016/0005-1098(78)90001-8.

[23] ASHRAE, ASHRAE Handbook-fundamentals, American Society of Heating, Refrigerating, Air-Conditioning, Engineers, Atlanta, 2009.

[24] J. Ma, J. Qin, T. Salsbury, P. Xu, Demand reduction in building energy systems based on economic model predictive control, Chem. Eng. Sci. 67 (2012) 92–100. https://doi.org/10.1016/j.ces.2011.07.052.

[25] J.A. Candanedo, A.K. Athienitis, Predictive control of radiant floor heating and solar-source heat pump operation in a solar house, HVAC R Res. 17 (2011) 235–256. https://doi.org/10.1080/10789669.2011.568319.

[26] G.P. Henze, D.E. Kalz, S. Liu, C. Felsmann, Experimental analysis of model-based predictive optimal control for active and passive building thermal storage inventory, HVAC R Res. 11 (2005) 189–213. https://doi.org/10.1080/10789669.2005.10391134.

[27] J.A. Candanedo, V.R. Dehkordi, M. Stylianou, Model-based predictive control of an ice storage device in a building cooling system, Appl. Energy. 111 (2013) 1032–1045. https://doi.org/10.1016/j.apenergy.2013.05.081.

[28] C.R. Touretzky, M. Baldea, A hierarchical scheduling and control strategy for thermal energy storage systems, Energy Build. 110 (2016) 94–107. https://doi.org/10.1016/j.enbuild.2015.09.049.

[29] Peter S. Curtiss, Examples of Neural Networks Used for Building System Control and Energy Management, in: Proc. Am. Soc. Heating, Refrig. Air-Conditioning Eng. Annu. Meet., Boston, MA, USA, 28 June-2 July, 1997: pp. 909–913.

[30] A. Afram, F. Janabi-Sharifi, A.S. Fung, K. Raahemifar, Artificial neural network (ANN) based model predictive control (MPC) and optimization of HVAC systems: A state of the art review and case study of a residential HVAC system, Energy Build. 141 (2017) 96–113. https://doi.org/10.1016/j.enbuild.2017.02.012.

[31] R. Ooka, S. Ikeda, A review on optimization techniques for active thermal energy storage control, Energy Build. 106 (2015) 225–233. https://doi.org/10.1016/j.enbuild.2015.07.031.

[32] T. Wakui, H. Kawayoshi, R. Yokoyama, H. Aki, Operation management of residential energy-supplying networks based on optimization approaches, Appl. Energy. 183 (2016) 340–357. https://doi.org/10.1016/j.apenergy.2016.08.171.

[33] A. Kelman, F. Borrelli, Bilinear model predictive control of a HVAC system using sequential quadratic programming, in: Proc. 18th World Congr. Int. Fed. Autom. Control, IFAC, 2011: pp. 9869–9874. https://doi.org/10.3182/20110828-6-IT-1002.03811.

[34] S. Ikeda, W. Choi, R. Ooka, Optimization method for multiple heat source operation including ground source heat pump considering dynamic variation in ground temperature, Appl. Energy. 193 (2017) 466–478. https://doi.org/10.1016/j.apenergy.2017.02.047.

[35] S. Ikeda, R. Ooka, Application of differential evolution-based constrained optimization methods to district energy optimization and comparison with dynamic programming, Appl. Energy. 254 (2019) 113670. https://doi.org/10.1016/j.apenergy.2019.113670.

[36] E.F. Camacho, C. Bordons, Model Predictive control, 2nd ed., Springer London, London, 2007. https://doi.org/10.1007/978-0-85729-398-5.

[37] B. Kouvaritakis, Model Predictive Control: Classical, Robust, and Stochastic [Bookshelf], 2016. https://doi.org/10.1109/mcs.2016.2602738.

[38] X. Li, J. Wen, Review of building energy modeling for control and operation, Renew. Sustain. Energy Rev. 37 (2014) 517–537. https://doi.org/10.1016/j.rser.2014.05.056.

[39] S.R. Mohandes, X. Zhang, A. Mahdiyar, A comprehensive review on the application of artificial neural networks in building energy analysis, Neurocomputing. 340 (2019) 55–75. https://doi.org/10.1016/j.neucom.2019.02.040.

[40] B. Yegnanarayana, Artificial neural networks, PHI Learning Pvt. Ltd., 1995.

[41] Kenji Suzuki, Artificial Neural Networks - Methodological Advances and Biomedical Applications, InTech, 2011. https://doi.org/10.5772/644.

[42] G. Mustafaraj, G. Lowry, J. Chen, Prediction of room temperature and relative humidity by autoregressive linear and nonlinear neural network models for an open office, Energy Build. 43 (2011) 1452–1460. https://doi.org/10.1016/j.enbuild.2011.02.007.

[43] R. König, Predictive Techniques and Methods for Decision Support in Situations with Poor Data Quality, University of Skövde, Sweden, 2009.

[44] V. Feoktistov, Differential Evolution, Springer, US, 2006.

[45] J. Pearl, Heuristics: intelligent search strategies for computer problem solving, United States, 1984.

[46] F. Glover, Future paths for integer programming and links to artificial intelligence, Comput. Oper. Res. 13 (1986) 533–549. https://doi.org/10.1016/0305-0548(86)90048-1.

[47] H.-P. Schwefel, Kybernetische evolution als strategie der experimentellen forschung in der strömungstechnik, Technical University of Berlin, 1965.

[48] I. Rechenberg, Cybernetic solution path of an experiment problem, 1965.

[49] L.J. Fogel, A.J. Owens, M.J. Walsh, Artificial intelligence through simulated evolution, John Wiley, Chichester, UK, 1966.

[50] H. Holland John, Adaptation in Natural and Artificial Systems, University of Michigan Press, Ann Arbor., 1975.

[51] J.R. Koza, Genetic Programming: On the Programming of Computers by Means of Natural Selection, The MIT Press: Massachusetts, 1992.

[52] R. Storn, P. Kenneth, Differential evolution – A simple and efficient adaptive scheme for global optimization for continuous space, 1995.

[53] M. Dorigo, Optimization, Learning and Natural Algorithms (in Italian), Politecnico di Milano, Milan, 1992.

[54] J. Kennedy, R. Eberhart, Particle swarm optimization, in: Proc. ICNN'95 - Int. Conf. Neural Networks, IEEE Press, n.d.: pp. 1942–1948. https://doi.org/10.1109/ICNN.1995.488968.

[55] P. Lucic, D. Teodorovic, Bee system: modeling combinatorial optimization transportation engineering problems by swarm intelligence, in: Prepr. TRISTAN IV Triennnial Symp. Transp. Anal., 2001: pp. 441–445.

[56] P. Lučić, D. Teodorović, Transportation modeling: An artificial life approach, Proc. Int. Conf. Tools with Artif. Intell. (2002) 216–223. https://doi.org/10.1109/TAI.2002.1180807.

[57] D. Karaboga, An idea on honey bee swarm for numerical optimization, n.d.

[58] S. Kirkpatrick, C.D. Gelatt, M.P. Vecchi, Optimization by Simulated Annealing, Science (80-.). 220 (1983) 671–680. https://doi.org/10.1126/science.220.4598.671.

[59] Z.W. Geem, J.H. Kim, G.V. Loganathan, A New Heuristic Optimization Algorithm: Harmony Search, Simulation. 76 (2001) 60–68. https://doi.org/10.1177/003754970107600201.

[60] J. Baxter, Local Optima Avoidance in Depot Location, J. Oper. Res. Soc. 32 (1981) 815–819. https://doi.org/10.1057/jors.1981.159.

[61] N. Mladenović, P. Hansen, Variable neighborhood search, Comput. Oper. Res. 24 (1997) 1097–1100. https://doi.org/10.1016/S0305-0548(97)00031-2.

[62] C. Voudouris, Guided Local Search — an Illustrative Example in Function Optimisation, BT Technol. J. 16 (1998) 46–50. https://doi.org/https://doi.org/10.1023/A:1009665513140.

[63] K. Price, R. Storn, Differential Evolution – A Simple and Efficient Heuristic for Global Optimization over Continuous Spaces, J. Glob. Optim. (1997) 341–359.

[64] Y. Haimes, On a bicriterion formulation of the problems of integrated system identification and system optimization, IEEE Trans. Syst. Man. Cybern. 1 (1971) 296–297.

[65] T. Takahama, S. Sakai, Constrained optimization by the ε constrained differential evolution with an archive and gradient-based mutation, 2010 IEEE World Congr. Comput. Intell. WCCI 2010 - 2010 IEEE Congr. Evol. Comput. CEC 2010. (2010) 1–9. https://doi.org/10.1109/CEC.2010.5586484.

[66] S. Ikeda, R. Ooka, Hybrid method of metaheuristics with machine learning for optimal operation of district energy systems, part 1 day-ahead optimization for district heating and cooling system including thermal energy storage (in Japanese), Soc. Heating, Air-Conditioning Sanit. Eng. Japan. 42 (2017) 11–20.

[67] S. Ikeda, Building and district energy optimization using metaheuristics and machine learning, The University of Tokyo, Japan, 2018.

[68] T. Kawamura, R. Ooka, S. Ikeda, Shape Optimization of a Detached House Considering Daylight Utilization Using Metaheuristics, in: 4th Int. Conf. Build. Energy Environ., Melbourne, Australia, 2018.

[69] T. Hilliard, L. Swan, Methodology to determine the impact of simplified building models on model-predictive-control morning start optimization performance, Sci. Technol. Built Environ. 24 (2018) 779–792. https://doi.org/10.1080/23744731.2017.1415088.

[70] P.H. Shaikh, N.B.M. Nor, P. Nallagownden, I. Elamvazuthi, T. Ibrahim, A review on optimized control systems for building energy and comfort management of smart sustainable buildings, Renew. Sustain. Energy Rev. 34 (2014) 409–429. https://doi.org/10.1016/j.rser.2014.03.027.

[71] S. Prívara, J. Cigler, Z. Váňa, F. Oldewurtel, C. Sagerschnig, E. Žáčeková, Building modeling as a crucial part for building predictive control, Energy Build. 56 (2013) 8–22. https://doi.org/10.1016/j.enbuild.2012.10.024.

[72] F. Amara, K. Agbossou, A. Cardenas, Y. Dubé, S. Kelouwani, Comparison and Simulation of Building Thermal Models for Effective Energy Management, Smart Grid Renew. Energy. 06 (2015) 95–112. https://doi.org/10.4236/sgre.2015.64009.

[73] H.B. Gunay, W. Shen, C. Yang, Blackbox modeling of central heating and cooling plant equipment performance, Sci. Technol. Built Environ. 24 (2018) 396–409. https://doi.org/10.1080/23744731.2017.1401417.

[74] John A Duffie, W.A. Beckman, Solar Engineering of Thermal Processes, Fourth Edi, Wiley, 2006.

[75] E.M. Kleinbach, W.A. Beckman, S.A. Klein, Performance study of one-dimensional models for stratified thermal storage tanks, Sol. Energy. 50 (1993) 155–166. https://doi.org/10.1016/0038-092X(93)90087-5.

[76] C. Runge, Ueber die numerische Auflösung von Differentialgleichungen, Math. Ann. 46 (1895) 167–178. https://doi.org/10.1007/BF01446807.

[77] W. Kutta, Beitrag zur näherungsweisen Integration totaler Differentialgleichungen, Z. Math. Und Phys. 46 (1901) 435–453.

[78] A.-C. and S.E. of J. Society of Heating, CASCADE III: Computer Aided Simulation for Cogeneration Assessment & Design, (2003).

[79] H.S. Carslaw, J.C. Jaeger, Conduction of Heat in Solids, Oxford University Press, 1959.

[80] L. Ingersioll, O.J. Zobel, I. A.C., Heat conduction with engineering, geological, and other applications, University of Wisconsins Press, 1954.

[81] G. Hagen, Ueber die Bewegung des Wassers in engen cylindrischen Röhren, Ann. Phys. 122(3) (1839) 423–442.

[82] J. Poiseuille, Recherches exprimentales sur le mouvement des liquides dans les tubes de petit diamtre, Comptes Rendus, Acad_emie Des Sci. (1841).

[83] W. Choi, R. Ooka, Effect of natural convection on thermal response test conducted in saturated porous formation: Comparison of gravel-backfilled and cement-grouted borehole heat exchangers, Renew. Energy. 96 (2016) 891–903. https://doi.org/10.1016/j.renene.2016.05.040.

[84] K. Levenberg, A method for the solution of certain non-linear problems in least squares, Q. Appl. Math. 2 (1944) 164–168. https://doi.org/10.1090/qam/10666.

[85] D.W. Marquardt, An Algorithm for Least-Squares Estimation of Nonlinear Parameters, J. Soc. Ind. Appl. Math. 11 (1963) 431–441. https://doi.org/https://doi.org/10.1137/0111030.

[86] G. Krauss, J.I. Kindangen, P. Depecker, Using artificial neural networks to predict interior velocity coefficients, Build. Environ. 32 (1997) 295–303. https://doi.org/10.1016/S0360-1323(96)00059-5.

[87] J.S. Haberl, D.E. Claridge, C. Culp, ASHRAE’s Guideline 14-2002 for Measurement of Energy and Demand Savings: How to Determine what was really saved by the retrofit, in: Proc. Fifth Int. Conf. Enhanc. Build. Oper., Pittsburgh, Pennsylvania, 2005.

[88] J. Heier, C. Bales, V. Martin, Combining thermal energy storage with buildings - A review, Renew. Sustain. Energy Rev. 42 (2015) 1305–1325. https://doi.org/10.1016/j.rser.2014.11.031.

[89] H. Akbari, O. Sezgen, Case Studies of Thermal Energy Storage (TES) Systems: Evaluation and Verification of System Performance, 1992.

[90] F. D'Ettorre, P. Conti, E. Schito, D. Testi, Model predictive control of a hybrid heat pump system and impact of the prediction horizon on cost-saving potential and optimal storage capacity, Appl. Therm. Eng. 148 (2019) 524–535. https://doi.org/10.1016/j.applthermaleng.2018.11.063.

[91] R. Halvgaard, P. Bacher, B. Perers, E. Andersen, S. Furbo, J.B. Jørgensen, N.K. Poulsen, H. Madsen, Model predictive control for a smart solar tank based on weather and consumption forecasts, Energy Procedia. 30 (2012) 270–278. https://doi.org/10.1016/j.egypro.2012.11.032.

[92] M. Aftab, C. Chen, C.-K.K. Chau, T. Rahwan, Automatic HVAC control with real-time occupancy recognition and simulation-guided model predictive control in low-cost embedded system, Energy Build. 154 (2017) 141–156. https://doi.org/10.1016/j.enbuild.2017.07.077.

[93] A. Mirakhorli, B. Dong, Occupancy behavior based model predictive control for building indoor climate—A critical review, Energy Build. 129 (2016) 499–513. https://doi.org/10.1016/j.enbuild.2016.07.036.

[94] S. Liu, G.P. Henze, Impact of modeling accuracy on predictive optimal control of active and passive building thermal storage inventory, in: 2004 Winter Meet. - Tech. Symp. Pap. Am. Soc. Heating, Refrig. Air-Conditioning Eng., 2004: pp. 155–167.

[95] R. Guglielmetti, D. Macumber, N. Long, Openstudio: An open source integrated analysis platform, Proc. Build. Simul. 2011. (2011) 442–449. https://www.nrel.gov/docs/fy12osti/51836.pdf.

[96] US DOE, EnergyPlus 8.5 Engineering Reference: The Reference to EnergyPlus Calculations, (2016). https://energyplus.net/sites/default/files/pdfs_v8.3.0/EngineeringReference.pdf.

[97] H. Akasaka, H. Nimiya, K. Soga, S. Matsumoto, K. Emura, N. Miki, E. Emura, K. Takemasa, Development of expended AMeDAS weather data for building energy calculation in Japan, ASHRAE Trans. 106 (2000) 455.

[98] T. Shibuya, B. Croxford, The effect of climate change on office building energy consumption in Japan, Energy Build. 117 (2016) 1–11. https://doi.org/10.1016/j.enbuild.2016.02.023.

[99] T. Ihara, Y. Kikegawa, K. Asahi, Y. Genchi, H. Kondo, Changes in year-round air temperature and annual energy consumption in office building areas by urban heat-island countermeasures and energy-saving measures, Appl. Energy. 85 (2008) 12–25. https://doi.org/10.1016/j.apenergy.2007.06.012.

[100] T. Miyazaki, A. Akisawa, T. Kashiwagi, Energy savings of office buildings by the use of semi-transparent solar cells for windows, Renew. Energy. 30 (2005) 281–304. https://doi.org/10.1016/j.renene.2004.05.010.

[101] L. Mba, P. Meukam, A. Kemajou, Application of artificial neural network for predicting hourly indoor air temperature and relative humidity in modern building in humid region, Energy Build. 121 (2016) 32–42. https://doi.org/10.1016/j.enbuild.2016.03.046.

[102] M. Wetter, Co-simulation of building energy and control systems with the Building Controls Virtual Test Bed, J. Build. Perform. Simul. 4 (2011) 185–203. https://doi.org/10.1080/19401493.2010.518631.

[103] C. Brooks, E.A. Lee, X. Liu, S. Neuendorffer, Y. Zhao, H. Zheng, Ptolemy II - Heterogeneous Concurrent Modeling and Design in Java, 2007. http://cobweb.cs.uga.edu/~maria/pads/papers/ptIIdesign1-intro.pdf.

[104] S. Ikeda, R. Ooka, Metaheuristic optimization methods for a comprehensive operating schedule of battery, thermal energy storage, and heat source in a building energy system, Appl. Energy. 151 (2015) 192–205. https://doi.org/10.1016/j.apenergy.2015.04.029.

[105] D. Lee, R. Ooka, S. Ikeda, W. Choi, Y. Kwak, Model predictive control of building energy systems with thermal energy storage in response to occupancy variations and time-variant electricity prices, Energy Build. 225 (2020) 110291. https://doi.org/10.1016/j.enbuild.2020.110291.

[106] I.W. Kirkman, P.A. Buksh, Data acquisition and control using National Instruments' '"LabVIEW"' software, Rev. Sci. Instrum. 63 (1992) 869–872. https://doi.org/10.1063/1.1142631.

Publications

Peer-reviewed journals

[1] D. Lee, R. Ooka, S. Ikeda, W. Choi, Artificial neural network prediction models of stratified thermal energy storage system and borehole heat exchanger for model predictive control, Sci. Technol. Built Environ. 25 (2019) 534–548. https://doi.org/10.1080/23744731.2018.1557464.

[2] M. Liu, T. Hino, R. Ooka, K. Wen, W. Choi, D. Lee, S. Ikeda, Development of distributed multiple heat source and multiple use heat pump system using renewable energy, J. Environ. Eng. AIJ. 85 (2020) 361–370. https://doi.org/10.3130/aije.85.361.

[3] D. Lee, R. Ooka, S. Ikeda, W. Choi, Y. Kwak, Model predictive control of building energy systems with thermal energy storage in response to occupancy variations and time-variant electricity prices, Energy Build. 225 (2020) 110–291. https://doi.org/10.1016/j.enbuild.2020.110291.

Conference proceeding papers (International)

[1] D. Lee, R. Ooka, S. Ikeda, W. Choi, Case study of ANN modeling of stratified thermal energy storage and ground source heat pump for model predictive control, 4th International Conference On Building Energy and Environment (COBEE), Melbourne, Australia, Feb 5-9, 2018.

[2] R. Ooka, D. Lee, S. Ikeda, W. Choi, Y. Kwak, Application of model predictive control to building energy systems with thermal energy storage, 2018 ASHRAE Annual Conference Papers, Houston, TX, 2018.

[3] D. Lee, R. Ooka, S. Ikeda, W. Choi, Y. Kwak, Model predictive control of building energy system including thermal energy storage, The Sustainable Built Environment (SBE) 19 Tokyo Conference, Tokyo, 2019.

[4] D. Lee, R. Ooka, S. Ikeda, W. Choi, Y. Kwak, Model predictive control of a building energy system including thermal energy storage, Building Simulation 2019, 16th IBPSA International Conference and Exhibition, Rome, Italy, 2019. https://doi.org/10.26868/25222708.2019.210664.

[5] Q. Guo, R. Ooka, W. Oh, W. Choi, D. Lee, Effect of insulation on indoor thermal comfort in a detached house with a floor heating system, The 13th REHVA World Congress CLIMA 2019, Bucharest, Romania, May 26-29, 2019. https://doi.org/10.1051/e3sconf/201911102049.

[6] M. Liu, R. Ooka, T. Hino, K. Wen, W. Choi, D. Lee, S. Ikeda, D. Palasz, Experimental performance analysis of a multiple-source and multiple-use heat pump system: winter field experiment and heating operation performance evaluation, The 13th REHVA World Congress

CLIMA 2019, Bucharest, Romania, May 26-29, 2019. https://doi.org/10.1051/e3sconf/201911101076.

[7] K. Wen, R. Ooka, T. Hino, M. Liu, D. Lee, W. Choi, S. Ikeda, D. Palasz, Experimental performance analysis of a multiple-source and multiple-use heat pump system: a predictive ANN model of sky-source heat pump, The 13th REHVA World Congress CLIMA 2019, Bucharest, Romania, May 26-29, 2019. https://doi.org/10.1051/e3sconf/201911105018.

[8] D. Lee, R. Ooka, Y. Matsuda, S. Ikeda, W. Choi, Experimental study of AI-based model predictive control strategy for thermal energy storage system, Enerstock 2021, Ljubljana, Slovenia, June 9-11, 2021.

[9] Y. Matsuda, R. Ooka, D. Lee, Building a predictive model for a heat source system with thermal energy storage using machine learning, Enerstock 2021, Ljubljana, Slovenia, June 9-11, 2021.

[10] D. Lee, R. Ooka, Y. Matsuda, S. Ikeda, W. Choi, Experimental Investigation of Model Predictive Control for Thermal Energy Storage System Using Artificial Intelligence, 29th Mediterranean Conference on Control and Automation, Bari, Puglia, Italy, June 22-25, 2021.

Conference proceeding papers (Domestic)

[1] D. Lee, R. Ooka, S. Ikeda, W. Choi, Development of optimization method for district heat-sharing network with thermal energy storage (Part 1) ANN model of stratified thermal storage based on physical model and measured data (in Japanese), in: Proceedings of AIJ annual conference at Hiroshima Institute of Technology, 2017: pp. 1173–1174.

[2] D. Lee, R. Ooka, S. Ikeda, W. Choi, Development of model predictive control method using ANN and metaheuristics (Part 1) Accurate prediction of heat source water temperature of GSHP using ANN (in Japanese), in: Technical papers of annual meeting, the Society of Heating, Air-Conditioning and Sanitary Engineers of Japan at Kochi University of Technology, 2017: pp. 157–160. https://doi.org/10.18948/shasetaikai.2017.9.0_157.

[3] S. Ikeda, R. Ooka, D. Lee, W. Choi, Development of model predictive control method using ANN and metaheuristics (Part 2) Validation of the benefits of ANN in day-ahead optimization for energy systems (in Japanese), in: Technical papers of annual meeting, the Society of Heating, Air-Conditioning and Sanitary Engineers of Japan at Kochi University of Technology, 2017: pp. 161–164. https://doi.org/10.18948/shasetaikai.2017.9.0_161.

[4] D. Lee, R. Ooka, S. Ikeda, W. Choi, Development of model predictive control method using ANN and metaheuristics (Part 3) Application of model predictive control to cooling operation of building energy systems with thermal energy storage (in Japanese), in: Proceedings of AIJ annual conference at Tohoku University, 2018: pp. 1291–1292.

[5] K. Wen, R. Ooka, T. Hino, M. Liu, W. Choi, D. Lee, S. Ikeda, Development of distributed water source heat-pump system for renewable energy (Part 8) System overview and heat collection characteristics of sky-source heat pump in winter (in Japanese), in: Proceedings of AIJ annual conference at Tohoku University, 2018: pp. 1325–1326.

[6] M. Liu, R. Ooka, T. Hino, K. Wen, W. Choi, D. Lee, S. Ikeda, Development of distributed water source heat-pump system for renewable energy (Part 9) Winter field experiment and heating operation performance evaluation (in Japanese), in: Proceedings of AIJ annual conference at Tohoku University, 2018: pp. 1327–1328.

[7] D. Lee, R. Ooka, S. Ikeda, W. Choi, Development of model predictive control method using ANN modeling of thermal energy storage and ground source heat pump system for accurate prediction (in Japanese), in: Proceedings of the 52th joint conference, the Society of Heating, Air-conditioning and Sanitary Engineers of Japan and Japan Society of Refrigerating and Air Conditioning Engineers at Tokyo University of Marine Science and Technology, 2018.

[8] D. Lee, R. Ooka, S. Ikeda, W. Choi, Development of model predictive control method using ANN and metaheuristics (Part 4) Application to an energy system with thermal energy storage considering disturbance of occupant heat load (in Japanese), in: Technical papers of annual meeting, the Society of Heating, Air-Conditioning and Sanitary Engineers of Japan at Daido University, 2018: pp. 57–60. https://doi.org/10.18948/shasetaikai.2018.2.0_57.

[9] M. Liu, R. Ooka, K. Wen, T. Hino, D. Lee, W. Choi, S. Ikeda, D. Palasz, Development of distributed water source heat-pump system for renewable energy (Part 10) Winter field experiment and heating operation performance evaluation (in Japanese), in: Technical papers of annual meeting, the Society of Heating, Air-Conditioning and Sanitary Engineers of Japan at Daido University, 2018: pp. 9–12. https://doi.org/10.18948/shasetaikai.2018.2.0_9.

[10] K. Wen, R. Ooka, T. Hino, M. Liu, D. Lee, W. Choi, S. Ikeda, D. Palasz, Development of distributed water source heat-pump system for renewable energy (Part 10) Winter field experiment and heating operation performance evaluation (in Japanese), in: Technical papers of annual meeting, the Society of Heating, Air-Conditioning and Sanitary Engineers of Japan at Daido University, 2018: pp. 13–16. https://doi.org/10.18948/shasetaikai.2018.2.0_13.

[11] D. Palasz, R. Ooka, T. Hino, W. Choi, M. Liu, K. Wen, D. Lee, S. Ikeda, B. Olesen, O. Kazanci, Performance evaluation for heating operation of a novel multiple-source multiple-use heat pump (MMHP) system in winter, in: Technical papers of annual meeting, the Society of Heating, Air-Conditioning and Sanitary Engineers of Japan at Daido University, 2018: pp. 5–8. https://doi.org/10.18948/shasetaikai.2018.2.0_5.

[12] D. Lee, R. Ooka, S. Ikeda, W. Choi, Development of model predictive control method using ANN and metaheuristics (Part 5) Study on the effect of hyperparameter of artificial neural network on its optimization calculation time for model predictive control (in Japanese), in:

Proceedings of AIJ annual conference at Kanazawa Institute of Technology, 2019: pp. 1399–1400.

[13] M. Liu, R. Ooka, T. Hino, K. Wen, W. Choi, D. Lee, S. Ikeda, Development of distributed water source heat-pump system for renewable energy (Part 14) Summer field experiment and cooling operation performance evaluation (in Japanese), in: Proceedings of AIJ annual conference at Kanazawa Institute of Technology, 2019: pp. 1057–1058.

[14] K. Wen, R. Ooka, T. Hino, M. Liu, W. Choi, S. Ikeda, D. Lee, Development of distributed water source heat-pump system for renewable energy (Part 15) A study on training data size required for predictive performance of regression models of sky-source heat pump (in Japanese), in: Proceedings of AIJ annual conference at Kanazawa Institute of Technology, 2019: pp. 1059–1060.

[15] Q. Guo, R. Ooka, W. Oh, W. Choi, D. Lee, Effects of insulation on indoor thermal comfort in a detached house with a floor heating system (in Japanese), in: Proceedings of AIJ annual conference at Kanazawa Institute of Technology, 2019: pp. 305–306.

[16] D. Lee, R. Ooka, S. Ikeda, W. Choi, Development of model predictive control method using ANN and metaheuristics (Part 6) Estimation of prediction and control horizon on optimal control in model predictive control, in: Technical papers of annual meeting, the Society of Heating, Air-Conditioning and Sanitary Engineers of Japan at Hokkaido University of Science, 2019: pp. 1–4. https://doi.org/10.18948/shasetaikai.2019.9.0_1.

[17] K. Wen, R. Ooka, T. Hino, M. Liu, D. Lee, W. Choi, S. Ikeda, Development of distributed water source heat-pump system for renewable energy (Part 16) Prediction of electricity consumption of RE house in winter using ANN and RNN (in Japanese), in: Technical papers of annual meeting, the Society of Heating, Air-Conditioning and Sanitary Engineers of Japan at Hokkaido University of Science, 2019: pp. 45–48. https://doi.org/10.18948/shasetaikai.2019.2.0_45

[18] M. Liu, R. Ooka, K. Wen, T. Hino, W. Choi, D. Lee, S. Ikeda, Development of distributed water source heat-pump system for renewable energy (Part 17) Analysis of pressure and temperature in piping system of RE house based on CFD (in Japanese), in: Technical papers of annual meeting, the Society of Heating, Air-Conditioning and Sanitary Engineers of Japan at Hokkaido University of Science, 2019: pp. 49–52. https://doi.org/10.18948/shasetaikai.2019.2.0_49.

[19] Q. Guo, R. Ooka, W. Oh, W. Choi, D. Lee, Simulation of indoor thermal environment of a radiant floor heating system in an environmental test room (in Japanese), in: Technical papers of annual meeting, the Society of Heating, Air-Conditioning and Sanitary Engineers of Japan at Hokkaido University of Science, 2019: pp. 353–356. https://doi.org/10.18948/shasetaikai.2019.6.0_353.

[20] Y. Matsuda, R. Ooka, D. Lee, S. Ikeda, W. Choi, Model predictive control with artificial intelligence for building heat source system (Part 1) Overview of experimental equipment and adjustment (in Japanese), in: Proceedings of AIJ annual conference, 2020.

[21] D. Lee, R. Ooka, Y. Matsuda, S. Ikeda, W. Choi, Model predictive control with artificial intelligence for building heat source system (Part 2) Construction of ANN prediction models based on experimental data (in Japanese), in: Proceedings of AIJ annual conference, 2020.

[22] D. Lee, R. Ooka, Y. Matsuda, S. Ikeda, W. Choi, Model predictive control with artificial intelligence for building heat source system (Part 3) Experiment for implementation of model predictive control to building heat source system (in Japanese), in: Technical papers of annual meeting, the Society of Heating, Air-Conditioning and Sanitary Engineers of Japan, 2020.

[23] D. Lee, R. Ooka, Y. Matsuda, S. Ikeda, W. Choi, Model predictive control with artificial intelligence for building heat source system (Part 4) Experimental analysis under different cooling load conditions (in Japanese), in: Proceedings of AIJ annual conference, 2021.

[24] D. Lee, R. Ooka, Y. Matsuda, S. Ikeda, W. Choi, Model predictive control with artificial intelligence for building heat source system (Part 5) Experimental analysis of model predictive control compared to TES priority operation (in Japanese), in: Technical papers of annual meeting, the Society of Heating, Air-Conditioning and Sanitary Engineers of Japan, 2021.

Acknowledgments

The completion of this doctoral dissertation involved the labor and support of many people. I would like to express my gratitude to all who helped and supported me to finish this dissertation.

First and foremost, I would like to express my deepest appreciation to my supervisor Prof. Ryozo Ooka. He gave me an opportunity to find a research theme to apply the field of model predictive control to building energy systems and encouraged me all the time to get interests in research upon entering the master program. He always guided me to fulfill this work with a warm heart.

I would also like to thank Prof. Hideki Kikumoto for his sincere advice on research and living life in the laboratory. His insightful advice in the regular laboratory seminars helped me to improve my doctoral dissertation.

My sincere gratitude also goes to Assoc. Prof. Shintaro Ikeda had given me help and encouragement every semester during the period of school life. Constructive criticism and guidance that he had offered helped me all the time since I was a master’s degree student.

Also, I would like to record my appreciation to Assistant Prof. Wonjun Choi for offering detailed and invaluable comments. Especially, I was pleased to learn technical know-how about planning research, conducting a field experiment, and analyzing a result.

I am also very grateful to Prof. Younghoon Kwak. He did not hesitate to aid me by offering valuable advice and suggestions whenever I have concerns about research.

This doctoral dissertation was made possible by support from Mr. Yuki Matsuda who supported this research through industry-academic cooperation. To him, I owe special thanks for the help and technical assistance I have received to progress the research perfectly as planned.

And a very special thanks to Dr. Wonseok Oh and Ms. Hyoeun Joo for supporting me to strengthen myself without giving up whenever I had a difficulty in my graduate school life.

Also, I am grateful to my seniors, colleagues, and members of the Ooka and Kikumoto laboratory who led me in a good direction and spend most of the time together during my graduate school life. During the last few semesters, I had no choice but to meet them often online because of the Corona

pandemic, they were always kind and supportive.

Finally, my deepest love and appreciation goes to my family who always respects me and gives me unstinting support. My mother, Gilsuk Kim always gave me life wisdom and heartfelt advice so as not to lose my motivation. Especially, the experience of studying abroad in Japan with my younger brother, Jongyeob Lee will be an unforgettable memory for a lifetime.

Doyun Lee

July 2021